UNIVERSITY OF CALIFORNIA, SAN DIEGO

Internal Wave Generation: Turbulent Episodes

A dissertation submitted in partial satisfaction of the
requirements for the degree
Doctor of Philosophy

in

Engineering Sciences (Mechanical Engineering)

by

Masoud JalaliBidgoli

Committee in charge:

Professor Sutanu Sarkar, Chair
Professor Matthew Alford
Professor Juan C. del Alamo
Professor Juan Lasheras
Professor Robert Pinkel

2017

The dissertation of Masoud JalaliBidgoli is approved, and it is acceptable in quality and form for publication on microfilm and electronically:

_____

_____

_____

_____

_____

Chair

University of California, San Diego

2017

DEDICATION

To my parents, Hossein and Zohreh,

and my brother, Mohammad,

whom I could not live without their unconditional love.

EPIGRAPH

I almost wish I hadn't gone down that rabbit-hole - and yet - and yet - its rather curious, you know, this sort of life!

-Alice in Wonderland

TABLE OF CONTENTS

LIST OF FIGURES

LIST OF TABLES

ACKNOWLEDGEMENTS

I would like to express my sincere thanks to my advisor Prof. Sutanu Sarkar for all his support and guidance during the last six years. I have learned much from both our insightful discussions and also his character and manner. His advice and support of my adventures have been invaluable.

I would like to also thank the rest of my thesis committee: Professor Matthew Alford, Professor Juan C. del Alamo, Professor Juan Lasheras, and Professor Robert Pinkel for their helpful comments, encouragement, and the inspiration to be a great scientist like them.

Besides my committee, I am grateful to have had the opportunity to work with Prof. Alberto Scotti and Prof. Edward Santilli. Collaboration with them was both enjoyable and educational.

I thank my fellow labmates here at the CFD Lab at UCSD for the stimulating discussions, the sleepless nights, and the friendly, supportive atmosphere in our group. In particular, special thanks to Dr. Hieu Pham, Dr. Bishakhdatta Gayen, Dr. Eric Arobone and Dr. Vamsi Chalamalla for their valuable training and guidance during the initial phases of my PhD. I am grateful to have had the chance to collaborate with Iman Gohari, Alexandra VanDine, and Dr. Narsimha Reddy Rapaka. I am also thankful for all the company and helps from Dr. Matt de Stadler, Dr. Anikesh Pal, Karu Chongsiripinyo, Vicky Verma, Jose Luis Ortiz Tarin, Pranav Suresh, and Sungwon Lee.

I was lucky to find great friends in San Diego. Supportive and caring friends like them were very important to flourishing during graduate school. These people shaped my

life here: Negin N, Brandon, Negin M, Payam, Alireza, Arman, Elina, Mojgan, Nojan, Negin L, Tina, Shiva, Bahar, Geraldine, Kamran, and Aria.

I would like to appreciate the love I have always received from my family: my parents and my brother. I am grateful for their everyday support throughout this journey. I know that I can always count on my family when times are rough.

Finally, I would like to give a word of thanks to all my co-authors for allowing me to use the following papers as a part of my thesis.

Chapter 3 is a reprint of material published in following journal: M. Jalali, N. Rapaka, S. Sarkar, "Tidal flow over topography: effect of excursion number on wave energetics and turbulence", *J.Fluid Mech.*, 750, 259-283, 2014. The dissertation author is the primary investigator and author of this paper.

Chapter 4 is a reprint of material published in following journal: M. Jalali, A. VanDine, V.K. Chalamalla, S. Sarkar, "Oscillatory stratified flow over supercritical topography: wave energetics and turbulence", *Comput. Fluids*, 0045-7930, 2016. The dissertation author is the primary investigator and author of this paper.

Chapter 5 is a reprint of material published in following journal: M. Jalali, S. Sarkar , "Large eddy simulation of flow and turbulence at the steep topography of Luzon Strait", *Geophys. Res. Lett.*, Accepted. The dissertation author is the primary investigator and author of this paper.

Chapter 6 is a reprint of material published in following journal: M. Jalali, V.K.

Chalamalla, S. Sarkar , "On the accuracy of overturn-based estimates of turbulent dissipation at rough topography", *J. Phys. Oceanogr*, 47.3 (2017): 513-532. The dissertation author is the primary investigator and author of this paper.

Chapter 7 is, in parts, a reprint of material under review for publication in following journal: V.K. Chalamalla, E. Santilli, A. Scotti, M. Jalali, S. Sarkar, "SOMAR-LES: A framework for multi-scale modeling of turbulent stratified oceanic flows" under review for publication in *Ocean Model*. The dissertation author is one of the investigators and co-authors of this paper.

VITA

2017	Ph. D. in Engineering Sciences(Mechanical Engineering), University of California, San Diego
2011	M. S. in Mechanical Engineering, University of Tehran, Iran
2010	B. S. in Industrial Engineering, University of Tehran, Iran
2009	B. S. in Mechanical Engineering *First Rank*, University of Tehran, Iran

PUBLICATIONS

M. Jalali, S. Sarkar , "Large eddy simulation of flow and turbulence at the steep topography of Luzon Strait", *Geophys. Res. Lett.*, Accepted

V.K. Chalamalla, E. Santilli, A. Scotti, **M. Jalali**, S. Sarkar, "SOMAR-LES: A framework for multi-scale modeling of turbulent stratified oceanic flows" under review for publication in *Ocean Model.*

M. Jalali, V.K. Chalamalla, S. Sarkar , "On the accuracy of overturn-based estimates of turbulent dissipation at rough topography", *J. Phys. Oceanogr*, 47.3 (2017): 513-532.

M. Jalali, A. VanDine, V.K. Chalamalla, S. Sarkar, "Oscillatory stratified flow over supercritical topography: wave energetics and turbulence", *Comput. Fluids*, 0045-7930, 2016.

M. Jalali, N. Rapaka, S. Sarkar, "Tidal flow over topography: effect of excursion number on wave energetics and turbulence", *J.Fluid Mech.*, 750, 259-283, 2014

ABSTRACT OF THE DISSERTATION

Internal Wave Generation: Turbulent Episodes

by

Masoud JalaliBidgoli

Doctor of Philosophy in Engineering Sciences (Mechanical Engineering)

University of California, San Diego, 2017

Professor Sutanu Sarkar, Chair

Mixing from turbulence plays a major role in establishing the physical and biological state of the ocean. Climate models which do not appropriately represent this mixing cannot accurately interpret present or predict future climate. Topographic features with steep slope on the ocean bottom are sites of significant energy conversion from the oscillating tide to internal gravity waves that break in the ocean interior. While such sites constitute an important source of deep ocean mixing, they can also host intense turbulence. In this research, we investigate the internal wave dynamics and turbulence at topographies ranging from isolated model obstacles to realistic multiscale ridges using three-dimensional, high-resolution numerical simulations. Direct Numerical Simulations

(DNS) and Large Eddy Simulation (LES) are performed to investigate the effect of topographic and flow properties such as Reynolds number (Re), excursion number (Ex) and slope criticality (ε) on internal wave fields, turbulence mechanisms and baroclinic energy budget terms. These simulations close the baroclinic energy budget, match with observations and illustrate significant local energy loss generated from mechanisms including but not limited to lee waves breaking on the slope during flow reversal, downslope jets, critical slope boundary layer, internal wave beams and off-slope lee-wave breaking. The simulation data are also used to assess the accuracy of estimates of turbulent dissipation inferred from density overturns. This density-overturn based method is commonly used as a simplification by oceanographers to infer dissipation due to the complexity and cost of direct microstructure measurements. Results of this work show positive bias in the magnitude of dissipation at locations where convective instability is the primary source of turbulence. To address the bias, we have introduced an alternative density overturn-based estimate for dissipation for turbulence driven by convective instability.

The physical scales of processes driving mixing during the generation of internal waves in the ocean spans several orders of magnitude from the outgoing low-mode internal tide (vertical scale of order 1 km, horizontal of order several tens of km, time of order hours) to the nonlinear formation of higher wavenumber modes to, finally, turbulence events with spatial scale of order meters and time scale of order minutes that leads to fine-scale turbulence. This immense range of scales poses a severe constraint on realistic simulations, and motivates our application of a recently developed multiscale tool, SOMAR-LES, with a novel hierarchical approach that combines Large Eddy Simulation (LES) at small scales with the Stratified Ocean Model with Adaptive Refinement (SOMAR) for the large scales.

Chapter 1

Introduction

Mixing by turbulence is key to the distribution of oxygen, salt, and heat in the ocean. A considerable portion of mixing observed below the main thermocline is attributed to internal gravity waves that are generated by the oscillation of the barotropic tide over bottom topography in the stratified ocean. Topographic waves, through the associated transport and mixing of momentum and tracers, are involved in setting the local biological and physical state of the ocean (Leichter et al., 2003; Wong et al., 2012; Cacchione et al., 2002) and impact the meridional overturning circulation (Wunsch and Ferrari, 2004). Some of the energy that is converted to internal waves dissipates locally leading to turbulence at the generation site, while the remainder radiates to the ocean interior and toward the continental margins leading to nonlocal turbulence. The local turbulence at the generation site affects the state of the benthic ocean around the generation site and also leads to mixed fluid and suspended particulate matter that are advected away along isopycnals. Accurate quantification of the fraction of energy that is dissipated locally determines the accuracy of both, the wave energy available for remote mixing and the local turbulence, and is thus of crucial importance.

In the barotropic approximation, the density is taken to be a function of solely pressure. The more general oceanic case wherein the density is a function of pressure and other variables such as temperature or salinity has baroclinicity. In the present case of tidal flow, *baroclinic response* refers to the flow physics caused by including buoyancy effects associated with temperature/salinity variation of the region. The barotropic velocity is defined as the depth-average of velocity in a vertical column of fluid over a bottom region with constant slope, and the baroclinic velocity is defined as the deviation from the barotropic velocity. The energy converted from the barotropic tide to baroclinic response locally dissipates by viscosity, transfers to turbulence, or leaves the generation site as the sum of an internal wave flux and an advective flux.

The barotropic tide in the deep ocean can be gentle but, when it flows over a rough ocean bottom with steep features, the response in the water column can be much more energetic and nonlinear. Different turbulence mechanisms are active at various types of topographies. For example, at the Brazil Basin, where the rough bottom is not steep but is extensive, wave-wave interaction is operative. In locations with steeper topography, like the Hawaiian Ridge (Rudnick et al., 2003) and Luzon Strait(Alford et al., 2011, 2015), there is evidence of direct wave breaking and other instabilities. Tall regions of $O(50-100)$ m with overturned isopycnals have been observed (Aucan et al., 2006; Levine and Boyd, 2006; Klymak et al., 2008) at Kaena Ridge, a generation site in the Hawaiian Ridge system, and massive turbulent overturns up to 300 m tall have been reported by Alford et al. (2011) at Luzon Strait. These tall overturns are phase-locked with the barotropic tide and exhibit large velocity fluctuations with fine-scale variability. Multiscale bathymetry which has several bumps with differing slope angles and length scales can host a combination of difference turbulence mechanisms. Observations show that turbulence varies with slope angle and is enhanced at steep slopes (with angle greater

or equal to that of internal wave phase lines with the horizontal), e.g. at Monte Josephine seamounts (Haren et al., 2015).

When categorizing topography, steepness is measured relative to the wave propagation angle. The steepness parameter is defined by $\gamma = (h/l)/\tan(\alpha)$ where h is the characteristic height and l is the half-length of the feature. The wave propagation angle, α, is taken with respect to the horizontal. It is the angle of the group velocity, $\overrightarrow{c_g}$, with the horizontal and also the inclination of the phase lines with the horizontal. Topography is distinguished as subcritical ($\gamma < 1$), near-critical ($\gamma \approx 1$), and supercritical ($\gamma > 1$). Features with $\gamma \geq 1$ are usually referred to as *steep*. The wave propagation angle, α, is shallow for typical ocean stratification, usually between $3 - 8^{\circ}$.

Large generation sites are those where the topographic length scale is large relative to the length of fluid excursion during a tidal cycle. Large sites correspond to low values of excursion number, $Ex = U_0/\Omega l$. Here, U_0 is the amplitude of the tidal velocity, Ω is the tidal frequency and l is the half-length of the roughness. The excursion number, Ex, is the ratio of horizontal fluid displacement during a tidal cycle to the topographic length scale, and can be interpreted as the strength of the advective term relative to the unsteady term in the Navier Stokes equations. Nonlinear flow features including turbulence are possible even for $Ex << 1$ if the slope is locally steep.

Regions with locally critical slope angle, i.e. $\varepsilon = 1$, host nonlinear effects due to the resonant wave generation process. The criticality parameter, ε, varies along the bathymetry and is the ratio of the local topographic slope ($\tan\beta$) to the slope ($\tan\alpha$) of the phase lines of freely propagating waves. Note that steepness parameter, γ, stands for the ratio of bulk steepness of the topography to the wave propagation angle while

local criticality, ε, is the ratio of slope at any particular location to the slope of the wave propagation angle. Critical slopes where $\varepsilon = 1$ cause a near-bottom intensified velocity which, for low Re_s, gives rise to a laminar boundary layer (Gostiaux and Dauxois, 2007; Zhang et al., 2008) and, at high Re_s ($Re_s > 100$), thickens the turbulent boundary layer with cyclical overturns (Gayen and Sarkar, 2010; Lim et al., 2010). Here, Re_s is the Reynolds number based on the Stokes boundary layer thickness. Overturns have been observed on critical regions of the continental slope by Bluteau et al. (2011)

Supercritical obstacles with low Ex can also have a nonlinear flow response if the topographic Froude number ($Fr_h = U_0/Nh$) is small as is true for large, tall features in stratified water. Here, the nonlinear response takes the form of a hydraulically controlled jet (Winters and Armi, 2013) and wave breaking near the ridge top as was found by Legg and Klymak (2008), Buijsman et al. (2012) in two-dimensional simulations of Kaena ridge and Luzon ridge, respectively, and by Alford et al. (2014) in recent observations at Kaena ridge.

Given the possibility of the local small-scale, nonlinearly-evolving flow features in the near-critical and supercritical cases, some of the energy converted from the barotropic tide to the internal wave field is expected to dissipate locally. Rapaka et al. (2013) employed DNS and LES in a laboratory-scale problem to examine internal wave energetics in the low-Ex, turbulent regime for a near-critical obstacle. The radiative flux in their simulations agrees well with linear predictions for low-Re subcritical topography but critical and supercritical cases with higher-amplitude forcing exhibited a significant decrease in radiative flux with respect to linear estimates.

If the horizontal length scale of the obstacle ($2l$) is comparable to the tidal ex-

cursion ($2U_0/\Omega$ with U_0 the amplitude of the tidal velocity and Ω the tidal frequency), the excursion number $Ex = U_0/(\Omega l)$ is no longer small, but is an $O(1)$ quantity. The excursion number, Ex, is generally small for large generation sites but can be large for smaller topographic features under energetic tides. A M2 tide (period of $T = 12.4$ hrs and $\Omega = 1.4 \times 10^{-4}$ s^{-1}) with an amplitude of 0.2 m/s has a fluid excursion length, $2U_0/\Omega = 2.8$ km. Under this tidal forcing, an ocean ridge with characteristic length scale of $2l = 200$ km corresponds to a small $Ex = 0.014$ while a small topographic feature with $2l = 2.8$ km corresponds to Ex = 1. If the barotropic cross-ridge velocity is even larger, e.g. 0.6 m/s as can occur in shallower water, a characteristic length scale of $2l = 8.4$ km corresponds to $Ex = 1$. Note that the topographic Froude number is $Fr_h = Ex(\Omega/N)/(h/l)$. For moderately steep topography with average slope angle comparable to the wave characteristic angle, it follows that $h/l = O(\Omega/N)$ leading to $Fr \simeq Ex$. We will investigate the dynamics of an isolated triangular obstacle over the range of low to O(1) values of Ex and Fr. Steady, unidirectional flow over an obstacle leads to lee waves which, especially in the linear context, have received much attention in the atmospheric sciences. Lee waves can break (Baines, 1995) leading to turbulence. The case of steady, unidirectional flow corresponds to the limit of $Ex \to \infty$ prompting the question of potentially nonlinear phenomena when Ex is not small compared to unity.

Although the LES of a tidal flow past a triangular model ridge can shed light on nonlinear processes operative at generation sites and quantify dissipation and mixing, it is important to note that a realistic multiscale generation site has not been previously studied with turbulence resolving simulations. This motivates the present LES of a steep topography location in Luzon strait where observations from the recent Internal Waves In Straits Experiment (IWISE) are available. Luzon Strait is a highly-energetic generation site for internal tides with extreme isopycnal displacements up to 500 m and

overturns that exceed 300 m (Alford et al., 2015). It is located between Taiwan and the Philippines and connects the Pacific Ocean to the South China Sea. Its complex bathymetry is mainly characterized by two ridges, Heng-Chun to the west and Lan-Yu to the east. The generated waves propagate westward into the South China Sea, steepen into non-linear solitary wave fronts, and dissipate near the Dongsha Plateau and the continental slope of China. These internal waves are important for marine navigation, offshore engineering, marine species, and sediment resuspension (Farmer et al., 2011). Alford et al. (2011) collected data as a part of the IWISE during August and September of 2010 along two lines: one along a southern line observing relatively less dissipation and another along a northern line, at which the depth-integrated energy flux was more dominantly semidiurnal and the dissipation was stronger. Results from a large-scale internal tide model found that the conversion to baroclinic energy did not balance the divergence of baroclinic flux so that the unbalanced term (presumably, dissipative losses) was substantial at the northern line, consistent with the higher dissipation estimates in the observations. The inter-ridge spacing is also close to a semidiurnal wavelength at this transect, allowing a resonance between the internal tidal beams generated at the east and west ridges, as suggested by Echeverri and Peacock (2010). Alford et al. (2011) also point to internal hydraulic phenomena and breaking lee waves as possible factors responsible for near-ridge dissipation, but they suggest that more work is required to determine the specific mechanisms of turbulent dissipation.

Buijsman et al. (2012) performed 2D MITgcm simulations of a zonal transect of Luzon at 20.6°N. They found constructive interference between the wave beams generated at the two ridges, resulting in an increase of baroclinic energy conversion, ridge-top velocities, and inferred dissipation. The spatio-temporal distribution of velocities and inferred dissipation was similar to observations (Alford et al., 2011). As a

follow-up study, Buijsman et al. (2014) performed 3D simulations, which having coarser resolution than their 2D model, accounted for large-scale three-dimensionality rather than improved turbulence resolution. The barotropic velocities were better predicted in the 3D model, and the topographic blocking and steering in 3D led to a stronger resonant interaction with IGW generation at the east ridge. The dissipation at Luzon Strait is high relative to the open ocean. Alford et al. (2011) estimated that nearly 40% of baroclinic energy is dissipated near the submarine ridges in their domain of study, much more than at the Hawaiian Ridge where estimates are between 8-25% (Klymak et al., 2006) and 19%(Carter et al., 2008). Alford et al. (2015) use *in situ* measurement along with numerical models to estimate again nearly 40% local dissipation at Luzon. However, they note uncertainty in this estimate and state that improved resolution of turbulent processes is necessary to better constrain the model result.

Chapter 2 describes the problem formulation and the numerical methods used to simulate the internal wave generation problem. It also discuss details of the calculation for terms in the barotropic to baroclinic energy conversion equation. Chapter 3 is an examination of internal tides with values of Ex up to unity using direct numerical simulation (DNS) of a laboratory-scale ridge shown in the schematic of figure 1.1. The model with a region having critical slope is used to study the properties of internal waves with a focus on how these properties change with respect to the low Ex regime. The objective of chapter 4 is to quantify the effect of increasing Ex on the wave field and turbulence in the case of an obstacle with *supercritical* slope. LES of the three-dimensional Navier-Stokes equations are employed for this purpose. We will compare the results with a critical-slope obstacle at the same values of Ex that was considered in chapter 3. We also compute a closed baroclinic energy budget and quantify the local baroclinic energy loss, q. Changes in q are linked to changes in the features responsible for turbulence.

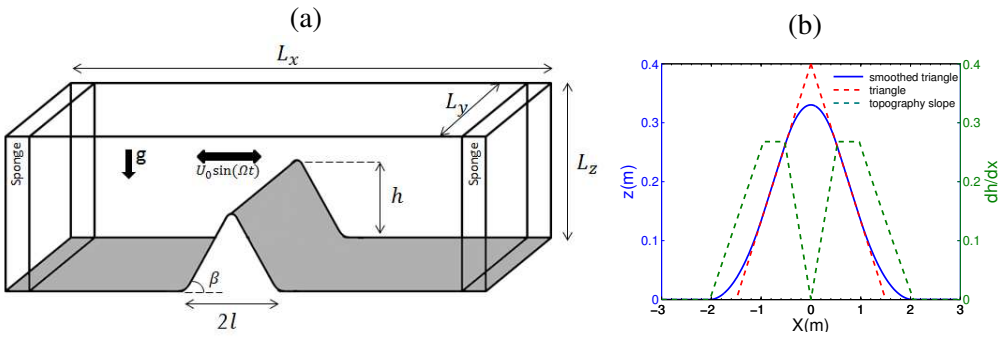

Figure 1.1: (a) Schematic of oscillating flow over a two-dimensional obstacle, (b) Profiles of the smoothed triangular topography (solid line) used in the present work and the triangular topography (dashed line) used by Pétrélis et al. (2006). Note that the constant slope region is critical with an angle of 15° and occupies 20% of the streamwise length.

In chapter 5, we perform turbulence-resolving LES to both understand the dynamics responsible for turbulence at steep topography such as Luzon and to quantify the local dissipation of the wave energy. Since LES of the entire Luzon strait with sufficiently high resolution to capture turbulence is impractical, a smaller 40 km portion is modeled. The realism of the present model in capturing the baroclinic response of the system over the local topography is demonstrated by using results of our simulation with barotropic forcing modelled after measurements reported as dataset N2a by Alford et al. (2011).

Chapter 6 describes two alternate methods for obtaining overturn-based dissipation estimates from the simulation data. Large eddy simulations to capture flow near such a complex bathymetry are the first of their kind, with various turbulence mechanisms contributing to the energy cascade to smaller scales. Therefore, before venturing into the complex problem of Luzon strait, the DNS simulation data of Chalamalla and Sarkar (2015) is re-examined and the dissipation rates calculated from the simulation data is compared against dissipation rates inferred from both conventional Thorpe and the new inversion sorting method. The comparison of overturn-based estimates with the turbulent

dissipation rate is performed at several spatial stations and with two different values of the forcing amplitude. The accuracy of overturn-based dissipation rates has been found to depend on the mechanism of transition to turbulence at different locations.

Chapter 7 is a brief foray into the application of a new multiscale numerical method, SOMAR-LES (Chalamalla et al., 2017) , to the Luzon strait problem of Chapter 5. A multiscale approach is necessary to span the disparity between length scales which can span 8 orders of magnitude. Current Ocean Global Circulation Models (OGCMs) are limited by horizontal resolution and hydrostatic approximation. For these reasons, OGCMs do not resolve scales smaller than $O(10\,\mathrm{Km})$. Physical processes occurring on smaller scales in an OGCM are parameterized with a variety of models. At the opposite end of the scale spectrum, turbulent process, are usually studied numerically with Direct Numerical Simulation (DNS) or Large Eddy Simulation (LES), at the cost of highly idealizing the geometry and driving mechanism. There is no unifying modeling framework which can simultaneously resolve large scale features and model small scale turbulence. The numerical technique discussed in chapter 7, is an attempt to bridge this gap to some extent. The Stratified Ocean Model with Adaptive Refinement (SOMAR) developed recently (Santilli and Scotti., 2011, 2015) is a non-hydrostatic model that can dynamically increase the resolution in localized regions where nonlinearity transfers energy to finer scales, allowing the model to capture both large-scale and small scale features of the flow at a reduced computational cost. This allows SOMAR to access scales normally inaccessible to the current generation OGCMs. These scales are amenable to be solved with a LES. Thus, a new technique, called SOMAR-LES, has been developed by Chalamalla et al. (2017), whereby a large eddy simulation is performed on the finest grids of the adaptive mesh to model the effects of the unresolved small scale turbulence on the resolved scales of the flow. The focus of chapter 7 is to demonstrate the SOMAR-LES

modeling technique by applying it to study internal tide generation at Luzon topography.

Chapter 2

Formulation and Numerical Method

The generation of internal waves by horizontally oscillating flow over an obstacle in a stratified fluid involves several key physical parameters as noted by Garrett and Kunze (2007), namely the depth of the ocean, H, height, h, and length, l, of the topography, and amplitude of the barotropic tidal velocity, U_0. A number of frequency parameters are also relevant for this formulation, specifically the barotropic forcing frequency, Ω, buoyancy frequency, N_∞, and Coriolis frequency, f. Significant non-dimensional parameters are as follows. The slope criticality, $\varepsilon = \tan\beta/\tan\alpha$, measures the local steepness of the topography with slope $\tan\beta$ relative to the internal wave characteristic with slope $\tan\alpha = \sqrt{(\Omega^2 - f^2)/(N_\infty^2 - \Omega^2)}$. As mentioned, the steepness, $\gamma = (h/l)/\tan\alpha$, is an overall measure of topographic steepness. The ratio of the background fluid excursion during one tidal cycle to the streamwise length scale of the topography is characterized by the excursion number, $Ex = U_0/\Omega l$. Local amplification of the barotropic tide relative to that in open water is determined by the topographic height change compared to the depth of the ocean, $h_r = h/H$. The topographic Froude number, $Fr_h = U_0/Nh$, which compares the vertical length scale, U_0/N, of the stratified flow to the topographic height, h, is an important parameter for both oscillating flow and steady currents. In viscous

flows, the Reynolds number also becomes important. The parameter, $Re_h = U_0 h/\nu$, is key for topography-scale features in the flow while the parameter $Re_s = U_0\sqrt{2\nu/\Omega}/\nu$ found from Stokes boundary layer analysis is relevant to the oscillating boundary layer.

2.1 Governing equations

The Navier-Stokes equations, solved numerically under the Boussinesq approximation in a non-rotating environment, are as follows:

$$\nabla \cdot \boldsymbol{u} = 0 \tag{2.1a}$$

$$\frac{D\boldsymbol{u}}{Dt} = -\boldsymbol{\nabla} p^* + F_b(t)\,\boldsymbol{i} + \frac{1}{Re}\nabla^2 u - B\rho^*\,\boldsymbol{k} - \nabla\cdot\boldsymbol{\tau} \tag{2.1b}$$

$$\frac{D\rho^*}{Dt} = \frac{1}{Re\,Pr}\nabla^2\rho^* + w\frac{d\rho^b}{dz} - \nabla\cdot\boldsymbol{\lambda}\,. \tag{2.1c}$$

In the above equations, $\mathbf{u} = (u, v, w)$ denotes velocity in streamwise (x), spanwise (y), and vertical (z) directions, respectively while ν is the molecular viscosity, κ is the thermal diffusivity, and ρ is the density. F_b is a barotropic forcing term. Bold letters indicate vector/tensor variables. The non-dimensional variables in the governing equations are related to dimensional values, denoted by subscript d, as follows:

$$t = t_d\Omega,\ \boldsymbol{x} = \frac{\boldsymbol{x_d}}{\frac{U_0}{\Omega}},\ p^* = \frac{p_d^*}{\rho_o U_o^2},\ \boldsymbol{u} = \frac{\boldsymbol{u_d}}{U_0},\ \rho^* = \frac{\rho_d^*}{\frac{U_0}{\Omega}\frac{d\rho_d^b}{dz_d}|_\infty}. \tag{2.2}$$

Here, p^* indicates the deviation from the background hydrostatic pressure while ρ^* denotes deviation from the background density state, $\rho^b(z)$.

The non-dimensional parameters, namely, Reynolds number, Re, Buoyancy parameter, B, and Prandtl number, Pr are defined as

$$Re \equiv \frac{l_{ex}U_0}{\nu} = \frac{U_0^2}{\Omega\nu} \quad , \quad B \equiv -g\frac{d\rho_d^b}{dz_d}|_\infty\frac{1}{\rho_0\Omega^2} = \frac{N^2}{\Omega^2} \quad , \quad Pr \equiv \frac{\nu}{\kappa}\,. \tag{2.3}$$

N is a characteristic value of the background buoyancy frequency taken here to be the value at the ridge crest. It is common in tidal flows to use the Reynolds number based on the characteristic length of the Stokes boundary layer thickness, $\delta_s = \sqrt{2\nu/\Omega}$,

$$Re_s = \frac{U_o \delta_s}{\nu} = \sqrt{2Re}\,. \tag{2.4}$$

Both Re and Re_s compare inertial to viscous forces. The Navier-Stokes equations are written using the coordinates

$$\xi = \xi(x,z) \quad , \quad \eta = \eta(x,z) \quad , \quad \zeta = \zeta(y), \tag{2.5}$$

where, at the slope, ξ points parallel to and across the slope while η is normal to the slope. Equation (2.1) is transformed as described by Fletcher (1991) to the form of a strong-conservation law as

$$\begin{aligned}
\frac{\partial U_j^c}{\partial \xi_j} &= 0 && \text{(2.6a)}\\
\frac{\partial (J^{-1}u_i)}{\partial t} + \frac{\partial F_{ij}}{\partial \xi_j} &= J^{-1}\cos(t)\delta_{1i} - J^{-1}B\rho^*\delta_{3i} && \text{(2.6b)}\\
\frac{\partial (J^{-1}\rho^*)}{\partial t} + \frac{\partial H_j}{\partial \xi_j} &= J^{-1}w && \text{(2.6c)}
\end{aligned}$$

where the fluxes are

$$\begin{aligned}
F_{ij} &= U_j^c u_i + J^{-1}\frac{\partial \xi_j}{\partial x_i}p' - \frac{1}{Re}uG^{jm}\frac{\partial u_i}{\partial \xi_m} + J^{-1}\frac{\partial \xi_j}{\partial x_m}\tau_{im}, && \text{(2.7a)}\\
H_j &= U_j^c \rho^* - \frac{1}{Re\,Pr}G^{jm}\frac{\partial \rho *}{\partial \xi_m} + J^{-1}\frac{\partial \xi_j}{\partial x_m}\lambda_m. && \text{(2.7b)}
\end{aligned}$$

Here the inverse of the the determinant of the Jacobian, J^{-1}, is the volume of the cell in physical space while U_j^c is the volume flux (contravariant velocity multiplied by J^{-1})

normal to the surface of constant ξ_j. G^{jm} indicates the mesh skewness tensor. These quanties are

$$U_j^c = J^{-1}\frac{\partial \xi_j}{\partial x_i}u_i, \tag{2.8a}$$

$$J = det\left(\frac{\partial \xi_j}{\partial x_i}\right), \tag{2.8b}$$

$$G^{jm} = J^{-1}\frac{\partial \xi_j}{\partial x_n}\frac{\partial \xi_m}{\partial x_n}. \tag{2.8c}$$

In Equation (2.1), τ_{im} is the subgrid-scale (SGS) stress tensor and λ_m is the SGS heat flux. The SGS stress tensor is calculated using the Smagorinsky model (Smagorinsky, 1963; Germano et al., 1991; Zang et al., 1993), which has been applied successfully in previous investigations. The accuracy of terms in the turbulent kinetic energy equation has been validated in such studies as Martin et al. (2000) who show close agreement between dynamic Smagorinsky and DNS in isotropic turbulence and Foysi and Sarkar (2010) who achieve similar results in a compressible mixing layer. More recently, Pham and Sarkar (2014) found good agreement in buoyancy-induced reduction in the shear layer growth rate and the TKE balance when comparing DNS and LES using the model. From the results of these prior studies, with a proper resolution for the large-eddy length scale and Ozmidov length scale, LES with the chosen subgrid model is an accurate and effective numerical scheme to be used for our problems. Using the popular dynamic Smagorinsky model (Smagorinsky, 1963; Germano et al., 1991; Zang et al., 1993), the SGS stress tensor, τ_{im}, is calculated as

$$\tau_{im} = -2\nu_t \tilde{S}_{im} \quad , \quad \nu_t = (C_s\Delta)^2|\tilde{\mathbf{S}}|. \tag{2.9}$$

Here, the Smagorinsky coefficient, C_s, is dynamically evaluated using a test filter, Δ_t, as well as a grid filter, Δ. Following Lund (1997), the LES models use a positive-definite

filter which is best described in terms of its standard deviation, $\Delta_t = \sqrt{12\int_{-\infty}^{\infty} x^2 G(x)dx}$. After discretization, the filter width ratio is calculated using trapezoidal integration to be $\Delta_t/\Delta = \sqrt{6}$. The model coefficient, C_s, is given by

$$C_s^2 = \frac{<L_{im}M_{im}>}{<M_{im}M_{im}>} \tag{2.10}$$

where

$$L_{im} = \overline{\tilde{u}_i\tilde{u}_m} - \overline{\tilde{u}}_i\overline{\tilde{u}}_m \quad , \quad M_{im} = 2\Delta^2\left(\overline{|\tilde{S}|\tilde{S}_{im}} - \alpha^2\overline{|\tilde{S}|}\,\overline{\tilde{S}_{im}}\right). \tag{2.11}$$

The test and grid filters are denoted by $\tilde{(\bullet)}$ and $\overline{(\bullet)}$ respectively, where $<\bullet>$ denotes the spanwise average. The magnitude of the resolved strain rate tensor is given by $|\tilde{S}| = \sqrt{(2\tilde{S}_{im}\tilde{S}_{im})}$.

Using a dynamic eddy viscosity model (Armenio and Sarkar (2002)), the SGS heat flux, λ_m, is similarly found to be

$$\lambda_m = -\kappa_t\frac{\partial\rho}{\partial x_m} \quad , \quad \kappa_t = (C_\rho\Delta)^2|\tilde{\mathbf{S}}|. \tag{2.12}$$

Here, $\rho = \rho^* + \rho^b$ is the density and the model coefficient, C_ρ, is given by

$$C_\rho^2 = \frac{<L_i^\rho M_i^\rho>}{<M_m^\rho M_m^\rho>} \tag{2.13}$$

where

$$L_i^\rho = \overline{\tilde{\rho}\tilde{u}_i} - \bar{\tilde{\rho}}\bar{\tilde{u}}_i \quad , \quad M_m^\rho = 2\Delta^2\left(\overline{|\tilde{S}|\frac{\partial\rho}{\partial x_m}} - \alpha^2\overline{|\tilde{S}|}\,\overline{\frac{\partial\rho}{\partial x_m}}\right). \tag{2.14}$$

The dynamic Smagorinsky model is a well established subgrid mode for LES which has been applied successfully in many similar cases, for examples, rotating channel flow (Piomelli, 1995), mixing layers (Vreman et al., 1997a), and flow over bluff bodies (Rodi et al., 1997). The accuracy of turbulent dissipation rate and the other terms in

the TKE equation has been validated in several studies, for example, by Martin et al. (2000) who show close agreement between dynamic Smagorinsky and DNS in isotropic turbulence, and by Foysi and Sarkar (2010) in a compressible mixing layer. Recently, Pham and Sarkar (2014) compared DNS and LES results in a stratified shear layer and found good agreement between them with regards to the buoyancy-induced reduction in shear layer growth rate and the TKE balance. Based on the results of these prior studies, with a proper resolution for the large-eddy length scale and the Ozmidov length scale, LES with the chosen subgrid mode is an accurate and effective numerical scheme to be used for our problems.

2.2 Numerical methods

The DNS/LES model is designed to handle environmental flows over boundaries. Its capabilities include: (1) computational boundaries that conform to topography, (2) a semi-coarsening multigrid Poisson solver for the pressure that efficiently handles anisotropic grids, (3) adaptive subgrid models for turbulent fluxes of momentum and scalars that allows for backscatter, (4) an adaptive near wall model for the smallest energy containing scales of motion that occur at the boundary but are not resolved by the near-boundary grid, (5) streamwise inhomogeneity if the mean flow evolution in the streamwise direction is important.

The three-dimensional, unsteady Navier Stokes equations, written in curvilinear coordinates that conform to topography, are numerically solved. The grid generation is based on transfinite interpolation. In this method, domain boundary points are specified

through four sets of parametric equations,

$$\mathbf{x}_b(\xi) \quad , \quad \mathbf{x}_t(\xi), \;\; 0 \leq \xi \leq 1 \tag{2.15a}$$

$$\mathbf{x}_l(\eta) \quad , \quad \mathbf{x}_r(\eta), \;\; 0 \leq \eta \leq 1. \tag{2.15b}$$

Here subscripts b, t, l and r of $\mathbf{x} = [x,z]$ denote bottom, top, left and right boundaries, respectively. Boundary points are used to create the interior grid as follows.

$$\begin{aligned} \mathbf{x}(\xi,\eta) = {} & (1-\eta)\,\mathbf{x}_b(\xi) + \eta\,\mathbf{x}_t(\xi) + (1-\xi)\,\mathbf{x}_l(\eta) + \xi\,\mathbf{x}_r(\eta) \\ & - \xi\,\eta\,\mathbf{x}_t(1) - \xi\,(1-\eta)\,\mathbf{x}_b(1) - \eta\,(1-\xi)\,\mathbf{x}_t(0) \\ & - (1-\xi)\,(1-\eta)\,x_b(0) \end{aligned} \tag{2.16}$$

This method yields a non-orthogonal grid. However, an orthogonal grid is more appropriate and therefore implemented near the boundary to accurately impose the zero normal heat flux condition at the bottom boundary conforming to the topography.

A mixed spectral/finite difference method is employed for spatial discretization. Periodic directions in the problem are treated using Fourier collocation and non-periodic directions with second-order finite difference. A low-storage, third-order accurate Runge-Kutta (RK3) method is employed for temporal integration with the exception of the diffusive terms which are calculated using second-order derivatives and treated implicitly with the alternating direction implicit (ADI) method. In each RK3 substep, the data is decomposed into $y-z$ planes during the ADI splitting process, Thomas algorithm, and multigrid pressure correction. However, upon transformation from physical to Fourier space and vice versa, it is necessary to alter the domain decompositiion to the $x-y$ plane to create data local in the x-direction for FFT. MPI is used to parallelize the code.

Rayleigh damping in the form of a sponge layer (Gayen and Sarkar, 2011b) is implemented at the right and left boundaries of the computational domain to minimize spurious reflections at artificial boundaries. The velocity and scalar fields are relaxed towards the background state in the sponge region by adding damping functions -$\sigma(z)\left[\boldsymbol{u}(\boldsymbol{x},t) - <u_{\boldsymbol{x}}>\right]$ and $-\sigma(z)\left[\rho(\boldsymbol{x},t) - \rho^b(z)\right]$ to the right hand side of the momentum and scalar equations, respectively. Here, $\sigma(z)$ is the sponge strength parameter that increases exponentially from the beginning to the end of the sponge region.

Zero velocity divergence is imposed with a fractional step method and the resulting Poisson pressure equation is solved using a multigrid method. The Poisson equation for the pressure correction is generated using the fractional step method Bewley (2007) as shown.

$$\frac{\partial}{\partial \xi_i}\left(G^{ij}\frac{\partial \phi^{n+1}}{\partial \xi_j}\right) = \frac{\partial U_j^{c*}}{\partial \xi_j} \tag{2.17}$$

Here, $U_j^{c*} = J^{-1}\frac{\partial \xi_j}{\partial x_i}u_i^*$ is an intermediate volume flux and superscripts n and $n+1$ denote current and advanced time level. Subsequently, velocity and pressure are corrected as

$$\mathrm{U}_j^{c(n+1)} = U_j^{c(n)} - G^{jm}\frac{\partial \phi^{n+1}}{\partial \xi_m} \quad , \quad \mathrm{p}^{*(n+1)} = p^{*(n)} + C_1\phi^{n+1}\,. \tag{2.18}$$

Here, C_1 is a factor that depends on the RK3 substep time interval. Equation (2.17) is solved using a two-dimensional multigrid method developed by Adams (1989).

With regards to boundary conditions, periodicity is imposed on velocity, density, ρ^*, and pressure, p^*, in the spanwise ($\zeta = \zeta(y)$) direction. At the bottom boundary, $\eta = 0$, zero velocity and zero normal density gradient are imposed. Additionally, orthogonality

is enforced near the boundary such that

$$\frac{\partial \rho}{\partial \eta} = 0 \Rightarrow \frac{\partial \rho^*}{\partial \eta} = \cos(\beta) \quad \text{at} \quad \eta = 0\,, \tag{2.19}$$

where $\beta = \tan^{-1}(h_x)$. At the top of the domain, $\partial u/\partial\eta = 0$, $v, w = 0$, and $\rho^* = 0$ while at the right and left boundaries, $\partial u/\partial\xi = 0$, $v, w = 0$, and $\rho^* = 0$. The pressure boundary condition at the top and bottom of the domain is $\partial p^*/\partial\eta = 0$ while $p^* = 0$ at the right and left edges of the computational domain.

In moderate *Re* cases with enough resolution, near wall flow is treated with no-slip boundary conditions. However, in flows with higher Reynolds number, specifically over large scale topographies, it is desirable to reduce near wall resolution requirements. This can be accomplished by employing a nonlinear drag model (Rapaka and Sarkar, 2016) as follows:

$$\left\{\frac{\partial \overrightarrow{u_t}}{\partial n}\right\}_1 = \frac{\{C_D \rho_0 |\overrightarrow{u_t}|\ \overrightarrow{u_t}\ \}_1}{\mu_{e1}} = \alpha \overrightarrow{u_t}_1 \tag{2.20}$$

where $\alpha = \{C_D \rho_0 |\overrightarrow{u_t}|\ \}_1 / \mu_{e1}$ and μ_e is the effective viscosity, $\mu_e \equiv \mu + \mu_{SGS}$, with μ_{SGS} being the sub-grid scale stress used in LES. The drag coefficient, C_D, is chosen here to be 0.0025, a common choice for bottom boundary layers Taylor and Sarkar (2008). The boundary condition for the velocity components is obtained using,

$$\overrightarrow{\tau_w} = \left\{\mu_e \frac{\partial \overrightarrow{u_t}}{\partial n}\right\}_w = \left\{\mu_e \frac{\partial \overrightarrow{u_t}}{\partial n}\right\}_1 \tag{2.21}$$

At a no-slip wall, μ_{SGS} is zero which results in huge velocity gradients near the wall, $\left\{\frac{\partial \overrightarrow{u_t}}{\partial n}\right\}_w$. To resolve this problem in the wall model, it is assumed that $\mu_e|_w = \mu_e|_1$ or $\left\{\frac{\partial \mu_e}{\partial n}\right\}_w = 0$ near the wall so that a linear discretization of the diffusion fluxes in the momentum equation yields a consistent shear stress and numerical stability. Therefore,

Equation (2.21) can be written as

$$\left\{ \frac{\partial \overrightarrow{u_t}}{\partial n} \right\}_w = \left\{ \frac{\partial \overrightarrow{u_t}}{\partial n} \right\}_1 = \alpha \overrightarrow{u_t}_1. \tag{2.22}$$

As $\overrightarrow{u_t}_w$ is parallel to $\overrightarrow{u_t}_1$, $\overrightarrow{u_t}_1$ can be expressed in terms of $\overrightarrow{u_t}_w$ using a Taylor series expansion as

$$\begin{aligned} \overrightarrow{u_t}_1 &= \overrightarrow{u_t}_w + \left\{ \frac{\partial \overrightarrow{u_t}}{\partial n} \right\}_w (\Delta n) \\ &= \overrightarrow{u_t}_w + (\alpha \overrightarrow{u_t}_1)\,(\Delta n) \end{aligned} \tag{2.23}$$

where Δn is the distance from the first cell center to the wall. Note that the impermeability boundary condition gives $\overrightarrow{u_n}_w = 0$ and hence, $\overrightarrow{u}_w = \overrightarrow{u_t}_w$, reducing the slip velocity at the wall to

$$\overrightarrow{u_w} = (1 - \alpha \Delta n)\ \overrightarrow{u_t}_1. \tag{2.24}$$

All the cases presented in this manuscript have no-slip boundary conditions unless it has specified otherwise.

2.3 Baroclinic to Barotropic energy conversion equation

The baroclinic energy equation is employed as the framework for investigating the energetics of the internal waves. In the case of linear inviscid theory, all the energy converted from the barotropic to the baroclinic wave field is assumed to reside in the internal wave field, i.e., Bt-Bc conversion and radiation terms are assumed equal. However, the present fully nonlinear, DNS enables relaxation of this simplifying assumption and separate quantification of the other key terms in the balance including the local dissipation

and the flux that is advected rather than being radiated as the pressure work. Rapaka et al. (2013) adapted the baroclinic energy equation of Carter et al. (2008) and Kang and Fringer (2011) to turbulent flow. The velocity, in split, into a mean field, including barotropic and baroclinic components, and a three dimensional fluctuation field

$$\begin{aligned} u(x,y,z,t) &= < u > (x,z,t) + u'(x,y,z,t) \quad &= U + u_{bc} + u' \\ w(x,y,z,t) &= < w > (x,z,t) + w'(x,y,z,t) \quad &= W + w_{bc} + w' . \end{aligned}$$

Similarly, pressure is decomposed as $< p^* >= P^* + p_{bc} + p'$ where p^* stands for the deviation from hydrostatic pressure. Symbol $<>$ indicates spanwise averaging. U, P^*, W are the barotropic components; the first two are the depth averages of $< u >$ and $< p^* >$, respectively, and $W(z) = -\frac{\partial}{\partial x}[z - h(x)]U$. The terms u_{bc}, w_{bc} and p_{bc} are baroclinic components. For $Re_s \gg 1$, the diffusive fluxes of wave energy can be neglected and the equation for the baroclinic energy without diffusive fluxes is simplified to

$$\frac{\partial}{\partial t}(\overline{E_k} + \overline{E_p}) + \nabla \cdot \overline{\mathbf{F}} = \overline{C} - \bar{\varepsilon}_{bc} - \bar{P} \tag{2.25}$$

The terms can be written in more detail as :

$$\begin{aligned}
\text{Unsteadiness} \qquad & \frac{\partial}{\partial t}(\overline{E_k}+\overline{E_p}) \\
\text{Pressure Flux (M)} \qquad & \nabla_H.(\overline{\boldsymbol{u}_{bcH}\, p^*}) \\
\text{Advection Flux } (M_{adv}) \qquad & \nabla_H.(\,\overline{\boldsymbol{u_H}(E_p+E_k)}+\overline{\boldsymbol{u}_{bcH}E_{hk}}\,) \\
\text{Dissipation } (\varepsilon_{bc}) \qquad & \overline{\rho_0 \nu \frac{\partial(\boldsymbol{u}_{bc})_i}{\partial x_j}\frac{\partial(\boldsymbol{u}_{bc})_i}{\partial x_j}} \\
\text{Turbulence production (P)} \qquad & -\overline{\langle u_i' u_j' \rangle_y \left\langle S_{ij} \right\rangle_y} \\
\text{Conversion (C)} \qquad & -\overline{\frac{\partial p^*}{\partial z} W} \\
\text{Nonlinear Conversion } (C_{nl}) \qquad & \rho_0 H(\,U\overline{\nabla_H.(\boldsymbol{u}_{bcH}u_{bc})}+V\overline{\nabla_H.(\boldsymbol{u}_{bcH}v_{bc})}\,)
\end{aligned}$$

where overbar lines represent depth integration, subscript H denotes horizontal, and

$$E_k = \frac{1}{2}\rho_0\left({u_{bc}}^2+{v_{bc}}^2+{w_{bc}}^2\right), \quad E_p = \frac{1}{2}N_\infty^{-2}b^2, \quad E_{hk} = \rho_0(U u_{bc}+V v_{bc}).$$

The buoyancy term, b, is defined as $b \equiv -g\rho^*/\rho_0$ and rate of strain tensor, S_{ij}, is defined as $S_{ij} \equiv \frac{1}{2}(\frac{\partial U_i}{\partial x_j}+\frac{\partial U_j}{\partial x_i})$. The energy flux, $\nabla \cdot \overline{\mathbf{F}}$, in equation (2.25) is expressed as the sum of the wave flux, M, and the advective flux, M_{adv}, in order to keep our notation consistent with literature. Boundary conditions corresponding to a two-dimensional topography are used to simplify the equation. C represents conversion from the barotropic to baroclinic wave field, ε_{bc} represents viscous dissipation of the baroclinic energy. The nonlinear part of conversion, C_{nl}, and the advection flux, M_{adv}, were not considered by Rapaka et al. (2013), but are required in this study because of high Ex. The term, $-P$, is

also considered as described in Rapaka et al. (2013) to account for turbulence production which represents local conversion from the internal tide to turbulence. Equation (2.25) can be reorganized,

$$C + C_{nl} = \frac{\partial}{\partial t}(E_p + E_k) + M + M_{adv} + \varepsilon_{bc} + P\,, \tag{2.26}$$

to give the following physical interpretation. It is important to distinguish between $-P$ which measures energy transfer from the internal tide to turbulence and ε_{bc} which is the viscous dissipation of the baroclinic wave field. In simulations that resolve high-*Re* turbulence, it is $-P$ that is linked to turbulent dissipation rate, not ε_{bc}. Local energy loss, q, is defined as $q = 1 - M/C$ in Chapter 3 and 4 and as $q = \varepsilon_{bc} + P$ in chapter 5.

Unlike Rapaka et al. (2013) and Jalali et al. (2014), the background buoyancy frequency is not constant in cases with realistic stratification. Therefore, it is more accurate to use the following equations for baroclinic potential energy and dissipation:

$$E_P = \int_{z-\zeta}^{z} g[\rho(z) - \rho_r(z^*)]dz^*$$
$$\varepsilon_p = g\kappa\nabla\rho^* \cdot \nabla\zeta$$

where ρ_r is the reference density $\rho = \rho_r + \rho^* = \rho_0 + \rho_b + \rho^*$ and ζ is the vertical displacement of a fluid particle. In the present problem, $\rho_b(z)$ is nonlinear, leading to a vertical variation in the buoyancy frequency $N(z)$ which is computed using $N^2 = -(g/\rho_0)d\rho_b/dz$. Using the two leading terms in the Taylor series expansion of ρ^*, the

values of E_P and ε_p can be estimated as

$$E_P = \frac{g^2 \rho^{*2}}{2\rho_0 N^2} + \frac{g^2 (N^2)_z \rho^{*3}}{6\rho_0^2 N^6},$$
$$\varepsilon_p = \frac{\kappa g^2}{\rho_0 N^2} (\nabla \rho^*)^2 + \frac{g^2 (N^2)_z \rho^*}{\rho_0^2 N^4} \frac{\partial \rho^*}{\partial z}.$$

Chapter 3

Tidal flow over model topography: Critical ridges

Three-dimensional direct numerical simulation is employed to investigate the effect of excursion number, Ex, on the internal wave field and turbulence at a laboratory-scale obstacle with smoothed triangular topography. Ex is increased from 0.066 to 1.0 while Re_s, the Reynolds number based on the Stokes boundary layer thickness, is kept constant. Here, we focus on the independent effect of Ex when Re_s is held constant and, furthermore, explore the $Ex = O(1)$ regime. The topography chosen is triangular with a constant slope portion, that is 20% of the streamwise length, inclined at the critical angle. The present simulations provide new results summarized below from which we infer that changing Ex from small to O(1) values leads to qualitative changes in the wave field as well as in the near-field turbulence.

3.1 Problem setup

An oscillating tide over a two dimensional obstacle, figure 1.1(a), is studied using fully nonlinear, three-dimensional simulations. Background thermal stratification with a constant buoyancy frequency, N_∞, is considered while the bottom surface is assumed adiabatic. The background barotropic current, $U(x)sin(\phi)$ where ϕ is the tidal phase, is forced by an imposed horizontal pressure gradient that oscillates in time (t_d),

$$F_0(t_d) = \rho_0 U_0 \Omega cos(\Omega t_d) \; . \tag{3.1}$$

Quantities u, v and w denote velocity in streamwise (x), spanwise (y) and vertical (z) directions, respectively. The obstacle shown in figure 1.1(b) is obtained by taking a triangular profile, equation (4.2) with $h_0 = 0.4m$ and $l_0 = 1.5m$, and then smoothing it. The height is 0.328 m and half-length, l_0, is 1.9 m, similar to the profile used by Rapaka et al. (2013).

$$z(x) = \begin{cases} h_0 \left(1 - \frac{|x|}{l_0}\right) & \text{if } |x| \leq l_0, \\ 0 & \text{otherwise.} \end{cases} \tag{3.2}$$

Table 3.1 shows the principal parameters of the simulations. Five cases are studied in a series where Ex is changed, keeping other nondimensional parameters constant. The value of Ex is changed from 0.064 to unity, a relatively high Ex. The large value of $Ex = 1$ is appropriate for energetic tides over small-scale obstacles in the ocean. For example, a M2 tide (period of $T = 12.4$ hrs and $\Omega = 1.4 \times 10^{-4}$ s^{-1}) with an amplitude of 0.2 m/s flowing over an obstacle with half-length of 1.42 km would lead to Ex of unity. The obstacle chosen here has a smoothed triangular shape that is moderately steep with 20 % slope length that is critical and blends smoothly into a subcritical region. The value of $Re_s = 177$ is larger than has been investigated in the laboratory experiments, is much smaller than oceanic values, but has the advantage of allowing DNS while being

Table 3.1: Parameters of the simulated cases. In cases CEX1-CEX5, Ex number changes while Re_s is kept constant. For all cases: $L_x = 40\,m$, $L_y = 0.5\,m$, $L_z = H = 3.28\,m$, $l = 1.9\,m$, $h = 0.328\,m$, $\beta = 15^o$, $\theta = 15^o$, $\Omega = 1$ s^{-1}, $\varepsilon = 1$, $N_\infty^2 = 14.93$ s^{-2} and $Pr = 1$.

Case	Re_s	Ex	Fr	N_x	N_y	N_z
CEX1	177	0.066	0.098	897	128	321
CEX2	177	0.200	0.300	897	128	321
CEX3	177	0.400	0.600	897	128	321
CEX4	177	0.700	1.026	897	128	321
CEX5	177	1.000	1.500	897	128	321

sufficiently large for turbulence. The wave angle of 15° with respect to the horizontal is smaller than in most laboratory experiments but still about 2-3 times larger than typical values in the ocean.

The turbulent fluctuations are inferred via departures of instantaneous velocity, pressure and density from the spanwise average. Statistics of turbulent quantities are a function of x and z, and are computed by spanwise averaging. The computational domain lengths in the horizontal directions, L_x and L_y, and the vertical domain length, L_z, are specified in table 3.1. The spanwise domain length, L_y, is chosen so as to accommodate the largest spanwise vortical structures that appear during convective instability. A grid with approximately 36 million grid points is used and designed to have adequate resolution of boundary layer turbulence and good resolution of turbulence arising from convective overturns and wave breaking. Case $CEX1$ has the first grid point from the wall at $z_1^+ = 2$ (distance normalized by the viscous wall unit ν/u_τ). Minimum grid resolution in the streamwise direction(Δx_{min}^+) is 21 and the spanwise direction has a uniform grid spacing of $\Delta y^+ = 16$ with spatial derivatives computed with spectral accuracy. The long integration time (about 10 cycles) is computationally expensive, e.g., approximately 9000 time steps are used per cycle for the $Ex = 1$ case.

3.2 Characteristics of the internal wave field

The spatial structure of internal wave field changes with Ex. At $Ex = 0.06$ (figure 3.1a), the internal wave response exhibits a coherent internal wave beam with fluid velocity that is substantially larger than the barotropic background velocity and an angle corresponding to the barotropic forcing, Ω. Rays with angles corresponding to harmonics and interharmonics can also be seen. However, with increasing Ex, the internal wave beam becomes less coherent and exhibits smaller velocity intensification. The wave response also becomes progressively more asymmetric with the beam pattern shifting towards the lee of the obstacle. When the slope angle is critical and equal to the characteristic angle of wave propagation in the stratified background, the local baroclinic response is resonant leading to intensification of near-bottom velocity. The model topography chosen here has a slope length, $l_c/l = 0.2$ at each flank. At low Ex, a fluid particle on the critical slope is exposed to a slope angle that is critical throughout its oscillation leading to the strong velocity intensification seen in figure 3.1(a) . At larger Ex, the fluid particles that are nominally on the critical slope are advected on to regions with subcritical slope angle, thus weakening the resonant response. The attenuation of normalized fluid velocity in the beam with increasing Ex is quantified in figure 3.2. We expect qualitative similarities between the behavior of the intensification and the normalized wave flux, M, because the latter depends on the amplitude of the oscillating fluid velocity.

Steady flow over an obstacle, in the appropriate Froude number regime, can lead to lee waves that are standing wave patterns in the lee of the obstacle. When the oscillatory tide has $Ex = O(1)$, analogous wave patterns are formed in the lee of the obstacle with phase lines that are different from the beams present at low Ex. The case

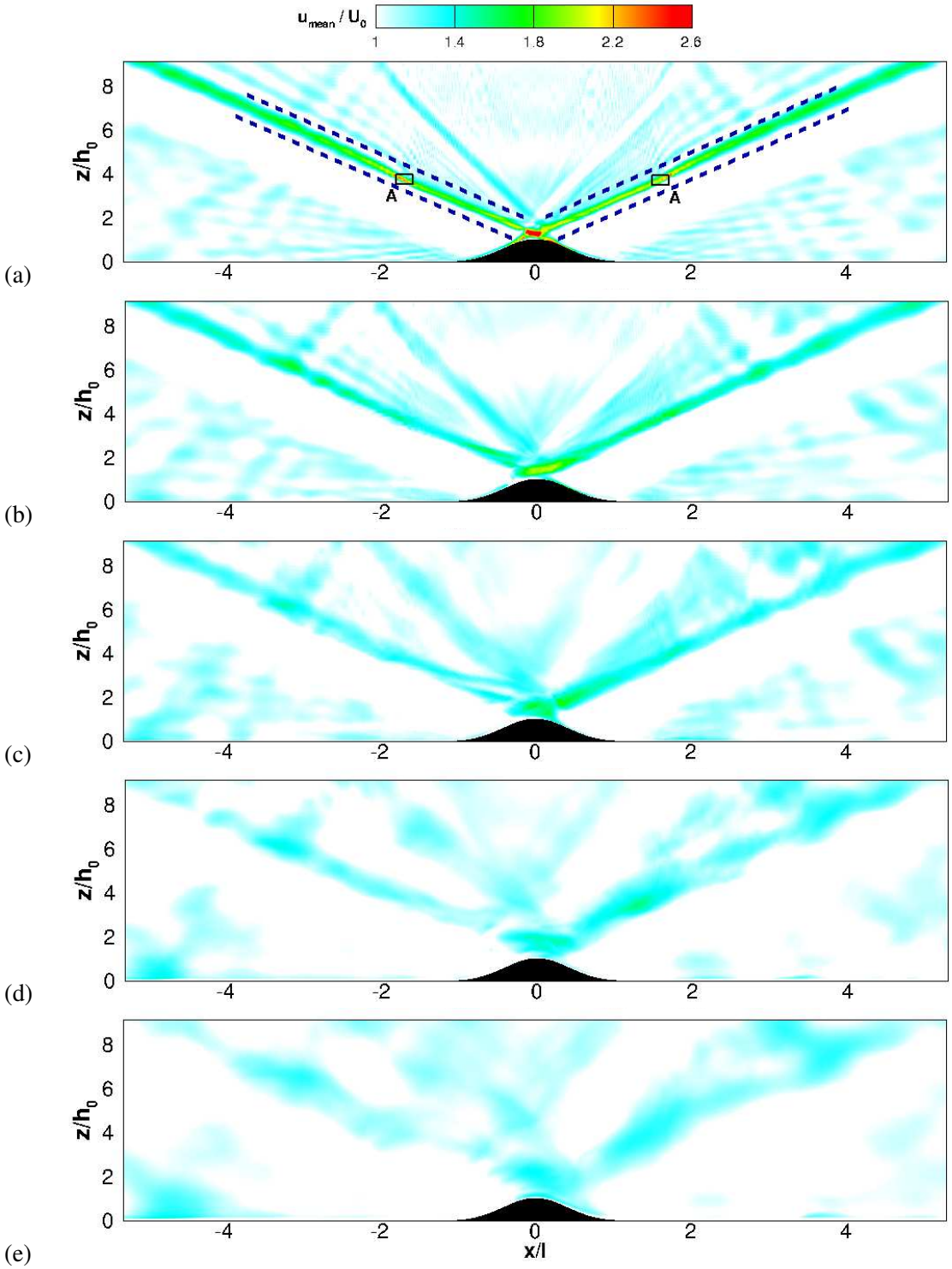

Figure 3.1: Instantaneous streamwise velocity at $t/T = 6.25$ and phase, $\phi = \pi/2$, corresponding to positive peak in barotropic velocity: (a)$Ex = 0.06$, (b)$Ex = 0.2$, (c)$Ex = 0.4$, (d)$Ex = 0.7$, and (e) $Ex = 1.0$. Topography is shown in black and beam regions are shown between blue dashed line at each side in (a.)

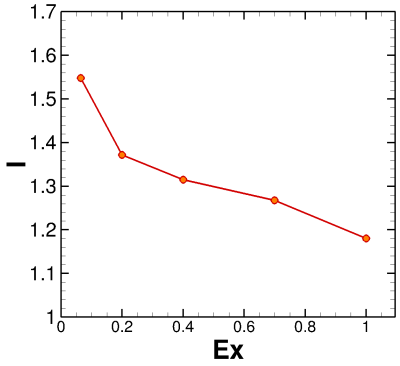

Figure 3.2: The dependence of velocity intensification, I, in the internal wave beam on excursion number. Here, $I = (1/A)\int u_b/U_0\, dA$ where u_b is the velocity amplitude in the beam region at $x/l \sim 2$ (shown in figure 3.1 (a) with symbol A) and A is the area of the beam region.

with $Ex = 1$ simulated here shows isopycnals with large displacements that extent to significant vertical and horizontal distances from the obstacle. The lee waves generated near the topography in each half cycle are responsible for these displacements. To obtain a clear picture of the life cycle of lee waves generated by oscillatory flow, it is beneficial to follow a wave phase line. The waves are released every half cycle at the lee side of the obstacle when the leeward flow reverses and the velocity passes through zero. Consider line A (figure 3.3 (a) on the right flank) that forms at phase 180°, the end of the half cycle with positive velocity, during which the right flank is in the lee of the oscillating tide. The inclination, θ_A, of phase line A with the horizontal can be estimated from linear theory as follows. A current of velocity U_0 flowing over a periodic bump of wavelength $\lambda = 2l$ gives rise to a wave with frequency $\omega = U_0\pi/l$ so that

$$\sin(\theta_A) = \omega/N = U_0\pi/lN = \pi Ex\, sin\theta, \tag{3.3}$$

where θ is the angle of the internal wave beam with the horizontal. Equation (3.3) with the parameters of case CEX5 leads to $\theta_A = 54.4°$ which, as shown in figure 3.3, agrees well with the inclination of the phase line A in the simulation. It is interesting to note

that, at $Ex = 1/\pi$, the inclination of the lee wave phase line is equal to that of a freely propagating internal wave ray and therefore conducive to an intensified wave response.

Line A is born and can be taken to be an initial phase line for the subsequent flow during the very next half cycle when the right flank becomes windward. Line A is advected from the windward side to the leeward side while another lee-wave phase line is being generated, e.g., line B in figure 3.3 (b). As shown in figure 3.3 (b), the displacement that was initially present in the lower part of line A fades; this is because the lee wave breaks at the topography leading to turbulence as will be discussed in the following section. Figure 3.3 (c) corresponds to phase 0° at which time the angle of line A changes because it advects into the region corresponding to a wave beam. The 0° phase corresponds to the end of leeward flow on the left flank and, accordingly, the lee wave on the left flank is fully formed as shown by phase line line B. Figure 3.3 (d) shows a phase of 90°. Line B has advected across and beyond the obstacle, and a new wave is being formed on the right side of the topography as shown by phase line C. However, line A at phase 180° with which we initiated the discussion is no longer identifiable. Thus, a lee wave phase line is very clear during half a cycle, from flow reversal at one flank to flow reversal at the other flank.

3.3 Turbulence

Figure 3.4(a)-(f) are snapshots of the near-field flow, each showing turbulent kinetic energy (TKE), isopycnals, and velocity profiles. Note that TKE = $0.5(u_{rms}^2 + v_{rms}^2 + w_{rms}^2)$ with subscript *rms* denoting root mean square. Three cases with $Ex = 0.06$, $Ex = 0.4$ and $Ex = 1.0$, respectively, are arranged as three rows with each row showing

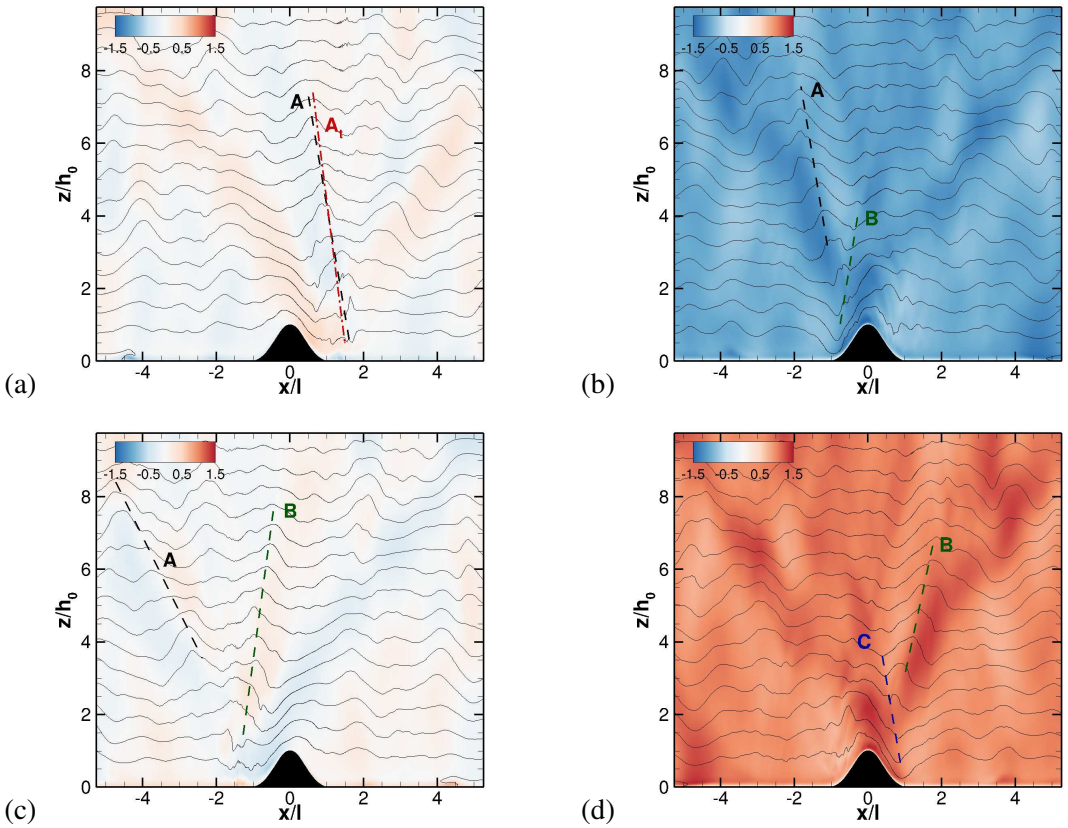

Figure 3.3: Normalized stream-wise velocity and isopycnals in case CEX5 ($Ex = 1.0$) for (a) $t/T = 5.5$, phase 180; (b) $t/T = 5.75$, phase=270; (c) $t/T = 6$, phase=0, and (d) $t/T = 6.25$, phase=90. The life cycle of a lee wave is illustrated through phase lines A, B and C. The line A_t shows a phase line obtained from linear theory using the barotropic velocity amplitude and obstacle length.

two phases of the flow. The left column corresponds to a phase when the flow turns from leftward to rightward or slightly past that point, and the right column corresponds to peak rightward velocity (phase 90) with the expectation of quasi-symmetric behavior at phase 180 and phase 270. At low Ex (figure 3.4a-b), TKE is present on the slopes, above the top of the obstacle as well as in the internal wave beam radiated away. At $\phi = 0^\circ$, there is a turbulence layer over and parallel to the left slope with a characteristic thickness equal to that of the overturned isopycnals in that region.

Intensification of the boundary flow at the critical slope (Gayen and Sarkar, 2011b) that leads to convective instability during flow reversal from down to upslope (Gayen and Sarkar, 2011a) is the underlying mechanism for transition to turbulence. These fluctuations then interact with the shear of the accelerating upslope flow to drive TKE. A quarter cycle later when the barotropic velocity peaks at $\phi = 90^\circ$ (figure 3.4 b), the turbulence patch is near the crest and again has a thickness equal to that of the overturned isopycnal. The TKE above the topography is bounded by the two internal wave beams that radiate upward from the flanks.

In moving from $Ex = 0.06$ to larger Ex numbers, there is a qualitative change in the turbulence. At $Ex = 0.4$, the patch of intense TKE (figure 3.4 c) becomes much taller, extending from the bottom to approximately twice the topographic height and, instead of being oriented parallel to the slope, is almost vertical. The isopycnals are indicative of a tall convective overturn of height approximately $2h_0$. The wave response (figure 3.1) was shown to be increasingly asymmetric with respect to the center with increasing Ex and so is the TKE pattern; owing to the leftward flow preceding $\phi = 0^\circ$, turbulence is displaced increasingly to the left (leeward) side. A rightward moving wave is released when the leeward flow slows down, isopycnals exhibit large amplitude deformation, and the generated lee waves break leading to turbulence, e.g. the tall and intense TKE patch

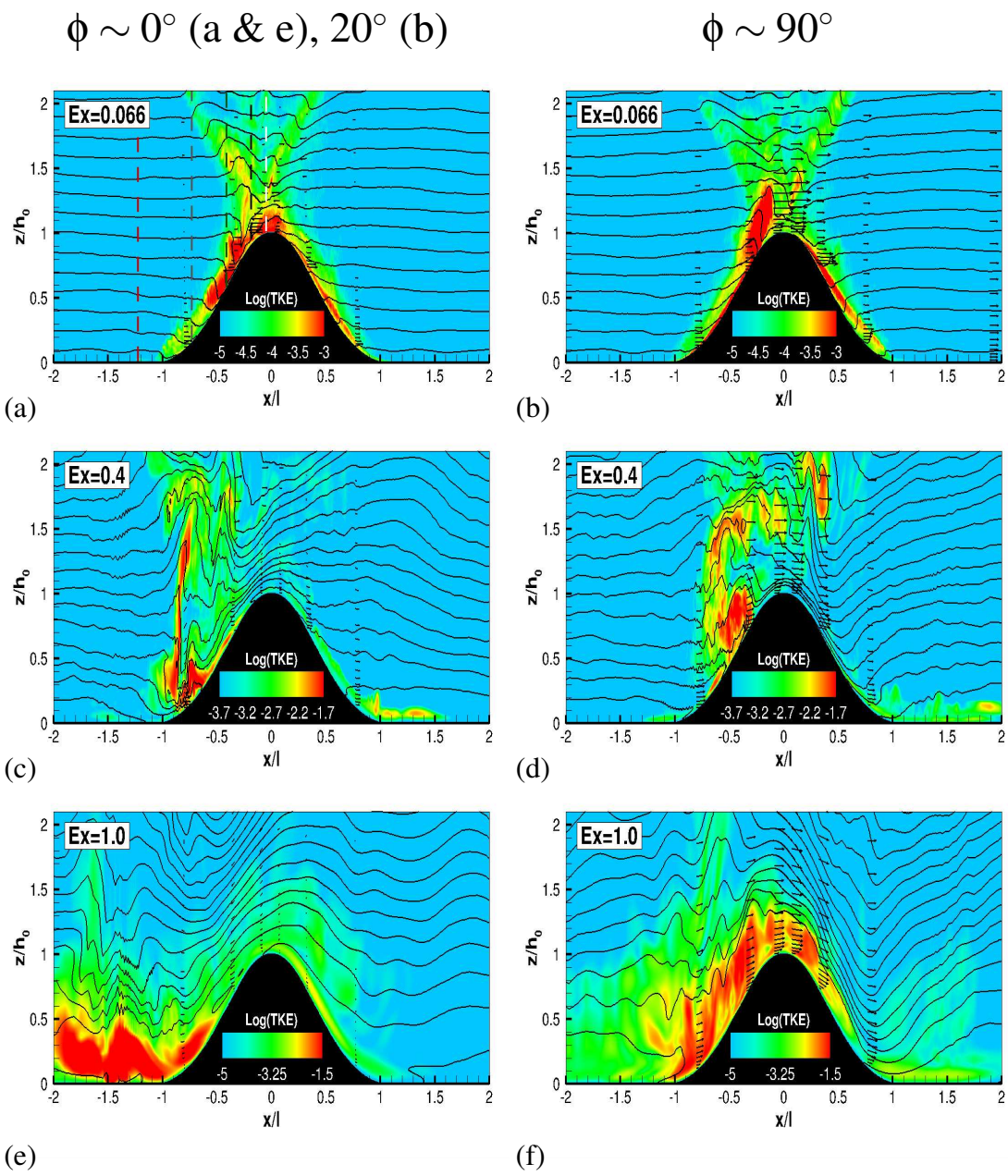

Figure 3.4: Snapshots of TKE (not normalized) and isopycnals. The left column corresponds to a phase of zero or small positive value of barotropic velocity while the right column corresponds to a positive peak of barotropic velocity: (a) $Ex = 0.06$ at $t/T = 6$, (b) $Ex = 0.06$ at $t/T = 6.25$, (c) $Ex = 0.4$ at $t/T = 6.05$, (d) $Ex = 0.4$ at $t/T = 6.25$, (e) $Ex = 1.0$ at $t/T = 6$, and (f) $Ex = 1.0$ at $t/T = 6.25$. Velocity vectors are also shown at selected cross sections.

at $x/l \sim -0.8$ in figure 3.4(c). Note that the phase of 20° that is shown in figure 3.4(c) allows sufficient time for TKE to develop from the convective instability that occurs slightly earlier at a phase of 0°. Turbulence present at $\phi = 20°$ advects upslope and there are additional smaller patches of TKE above the obstacle at the later time shown in figure 3.4(d). Since the beams are no longer thin and strong, the smaller patches of turbulence are not clearly clustered along characteristic ray paths.

There is a further change in the spatial pattern of turbulence at $Ex = 1$. Although the vertical displacement of isopycnals is as large as at $Ex = 0.4$, the height of the TKE patches in figures 3.4 (e)-(f) is not as large. Since a fluid particle sweeps back and forth across the entire topographic feature when Ex is unity, the critical angle present at only 20% of the length is unable to significantly intensify the baroclinic velocity unlike at low Ex. Therefore, in spite of the large fluid velocity, the internal wave shear is not large away from the boundary. Turbulence is dominant in a bottom boundary layer (figure 3.4e) with weakly stratified fluid and large shear in the lee wave response. Later in time, the weakly stratified layer of turbulence advects upslope. When the barotropic velocity is positive and at maximum (figure 3.4f), TKE is present over the entire windward slope.

Overturned lee waves and turbulence high above an obstacle can occur in the case of steady currents as discussed by Baines (1995) and by the numerical investigations of Afanasyev and Peltier (1998); Yakovenko et al. (2011). Here, the lee wave displacements in the $Ex = O(1)$ cases extend high above the obstacle but do not overturn. A likely reason is that the duration, $T/2$, of unidirectional flow is not sufficiently long. The nondimensional time corresponding to a half-period is

$$\frac{U_0 T}{2h} = \frac{U_0 \pi}{\Omega h} = \frac{\pi Ex}{A}, \tag{3.4}$$

where $A = h/l$ is the aspect ratio of the obstacle. The simulations of Yakovenko et al. (2011) conducted at $Fr = 0.6$ required $U_0 t/h \sim 22.5$ for overturning and $U_0 t/h \sim 40$ for a fully developed patch of turbulence. Since $A \simeq 0.2$ and $Ex \leq 1$ in the present simulations, the lee waves do not have sufficient time to overturn and break down into turbulence. Nevertheless, overturning aloft the obstacle may be possible at smaller values of A and also when Fr is smaller leading to stronger nonlinearity associated with the bottom boundary.

The gradient Richardson number, $Ri_g(x,z) = N^2(x,z)/S^2(x,z)$, where S is the mean (span-averaged) shear and N is mean (span-averaged) buoyancy frequency is an indicator of possible instability. Convective instability ($Ri_g(x,z) < 0$) and shear instability ($0 < Ri_g(x,z) < 0.25$) at the phases corresponding to the snapshots shown in Figure 3.4 are shown in Figure 3.5. When $Ex = 0.066$, the convective instability associated with flow reversal ($\phi = 0^\circ$) is clearly present at $x/l \sim -0.5$, the region where the slope is critical, and advects to a somewhat higher location at $\phi = 90^\circ$. There are also convective and shear unstable regions in the narrow region adjacent to the sides of the topography, particularly in the downward beam at the leeward side, associated with shear in the high-mode baroclinic response.

In addition, the crossing of the two beams radiated from the opposite sides, leads to unstable regions at the crest. Small regions of shear instability in the upward beams are also noticeable, even as high as $z/h \sim 1.4$, in figure 3.5 (b), and they lead to turbulence in the beams as discussed later.

At a larger value of $Ex = 0.4$ (figure 3.5c), there is a tall convectively unstable region with $Ri_g < 0$ located at $x/l \sim -0.9$, bounded from below by the bottom, and

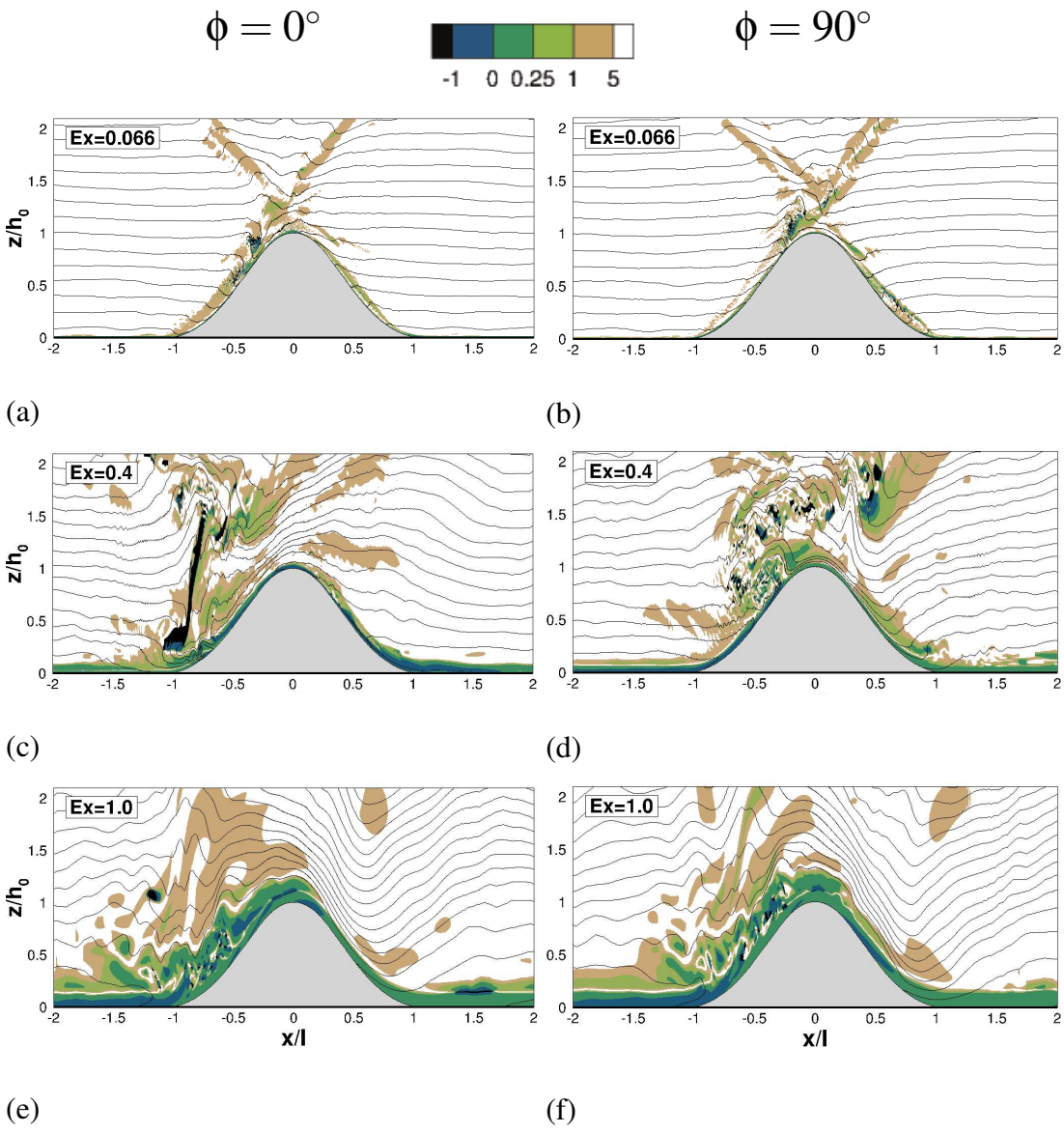

Figure 3.5: Ri_g and isopycnals near the topography for $Ex = 0.06$,$Ex = 0.4$ and $Ex = 1$ are shown at $t/T = 6.0$ (phase 0) and $t/T = 6.25$ (phase 90).

from above by the the beam launched from the opposite flank of the topography. This convective instability at $\phi = 0^\circ$ is responsible for transition to turbulence that evolves into the tall patch of TKE at $\phi = 20^\circ$ that was seen at $x/l \sim -0.8$ in figure 3.4(c). Because of the subsequent rightward propagation of the wave field, patches of convective and shear instability can be seen to span a large area between the topography and the beams in figure 3.5 (d). In addition, convective and shear instabilities occur in the boundary layer at both phases shown for $Ex = 0.4$. When the tidal forcing is further increased so that $Ex = 1.0$, shear instability in the boundary layer dominates as shown in figure 3.5 (e)-(f) although there are interspersed convectively unstable spots indicative of overturns. The regions with $0.25 < Ri_g < 5.0$ above the near-bottom turbulent layer have weaker TKE with patterns that are similar between $Ex = 0.4$ and $Ex = 1.0$ as can be seen by comparing parts (e) and (f) of figure 3.5 with parts (c) and (d), respectively.

The spatial organization of cycle-averaged TKE in figure 3.6 changes dramatically with increasing Ex. Turbulence is concentrated on the upper slope (the critical region and above it) and along the internal wave beams at lower $Ex = 0.066$, is concentrated at and above the lower slope in the $Ex = 0.4$ case, and is concentrated at the flat bottom adjacent to the obstacle and in an envelope around the obstacle at $Ex = 1.0$. When normalized by the kinetic energy of the barotropic forcing and the characteristic area of the obstacle cross-section, the integrated TKE is largest at the lowest $Ex = 0.066$ and is reduced by almost an order of magnitude at $Ex = 1$. At the lower excursion numbers, there is significant turbulence above the topography, i.e., TKE extends to almost two topographic heights above the flat bottom, $z = 0$. The spatial organization of different terms in the cycle-averaged TKE balance is shown in figure 3.7. In all cases, shear production, P, is the primary overall source in the TKE balance. Integrated buoyancy flux is positive and a significant source of turbulence in the regions of convective instability: on and above

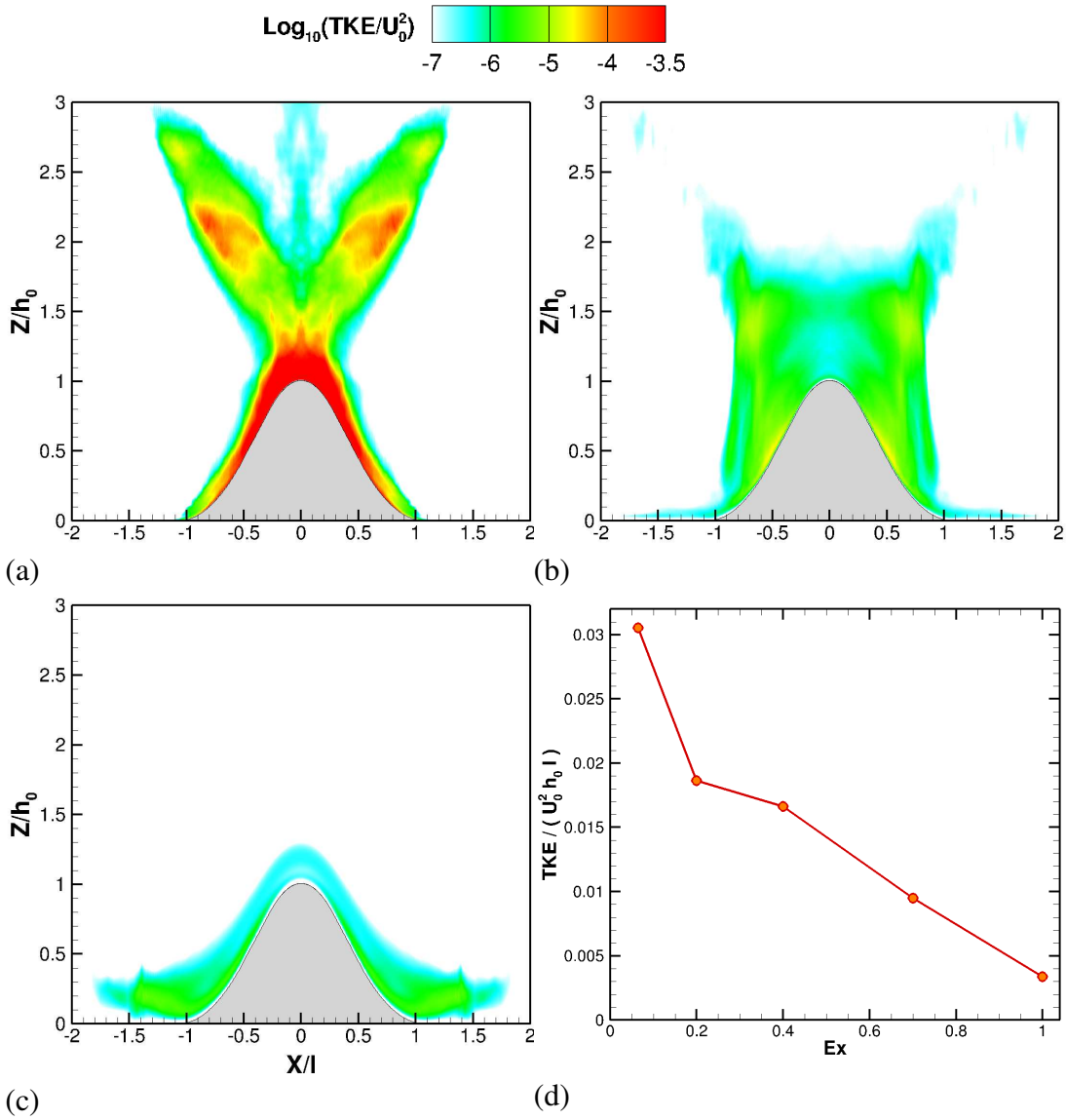

Figure 3.6: The spatial organization of cycle-averaged TKE normalized by U_0^2: (a) $Ex = 0.066$, (b) $Ex = 0.4$ and (c)$Ex = 1.0$. Part (d) shows the cycle-averaged TKE integrated between $-2 < x/l < 2$ and normalized with the barotropic TKE and characteristic obstacle area ($U_0^2 h_0 l$) as a function of Ex.

the critical slope at $Ex = 0.066$, and in the transient breaking lee waves at $Ex = 0.04$ and $Ex = 1.0$. Advection is an important component of the TKE balance since it spatially redistributes TKE from areas with significant shear or buoyancy production. For instance, at $Ex = 0.04$, advection acts to redistribute energy from the region with wave breaking (a sink term in figure figure 3.7 e) to the region near the crest (a source term in figure figure 3.7 e). The spatial organization of the turbulent dissipation is similar to that of the turbulent production.

We now discuss temporal patterns of turbulence. A remarkable finding at $Ex = 0.066$ is the temporal growth of turbulence (figure 3.8) in the radiated internal wave beam. Figure 3.8 shows the evolution of u_{rms}/U_0 at different points that belong to the internal wave beam (dashed line in figure 3.1 a) and located by their normalized height above bottom z_b/h_0. Higher locations in the beam exhibit turbulence at later time, e.g., even a location as high as $z_b/h_0 = 3$ exhibits TKE after 6 cycles. In addition to the advection of turbulence from the crest into the beam, the large shear within the beams leads to instability.

Field study of turbulence often involves interpretation of the time evolution of the flow at a few vertical moorings. The time evolution of the vertical profiles of normalized TKE at the summit, $x/l = 0$, and at approximately midslope, $x/l = -0.4$, is shown in Figure 3.9 (a)-(f) over two tidal cycles. It is noteworthy that, when normalized by the barotropic forcing, the case with largest $Ex = 1.0$ has the weakest turbulence, both in terms of time duration and height from the bottom. Also, as shown previously by Rapaka et al. (2013), TKE at the summit of the ridge shows *two* maxima in a cycle corresponding to the passage of turbulence from each of the two internal wave beams generated at the ridge flanks, but shows only *one* maximum at midslope. At $Ex = 0.066$,

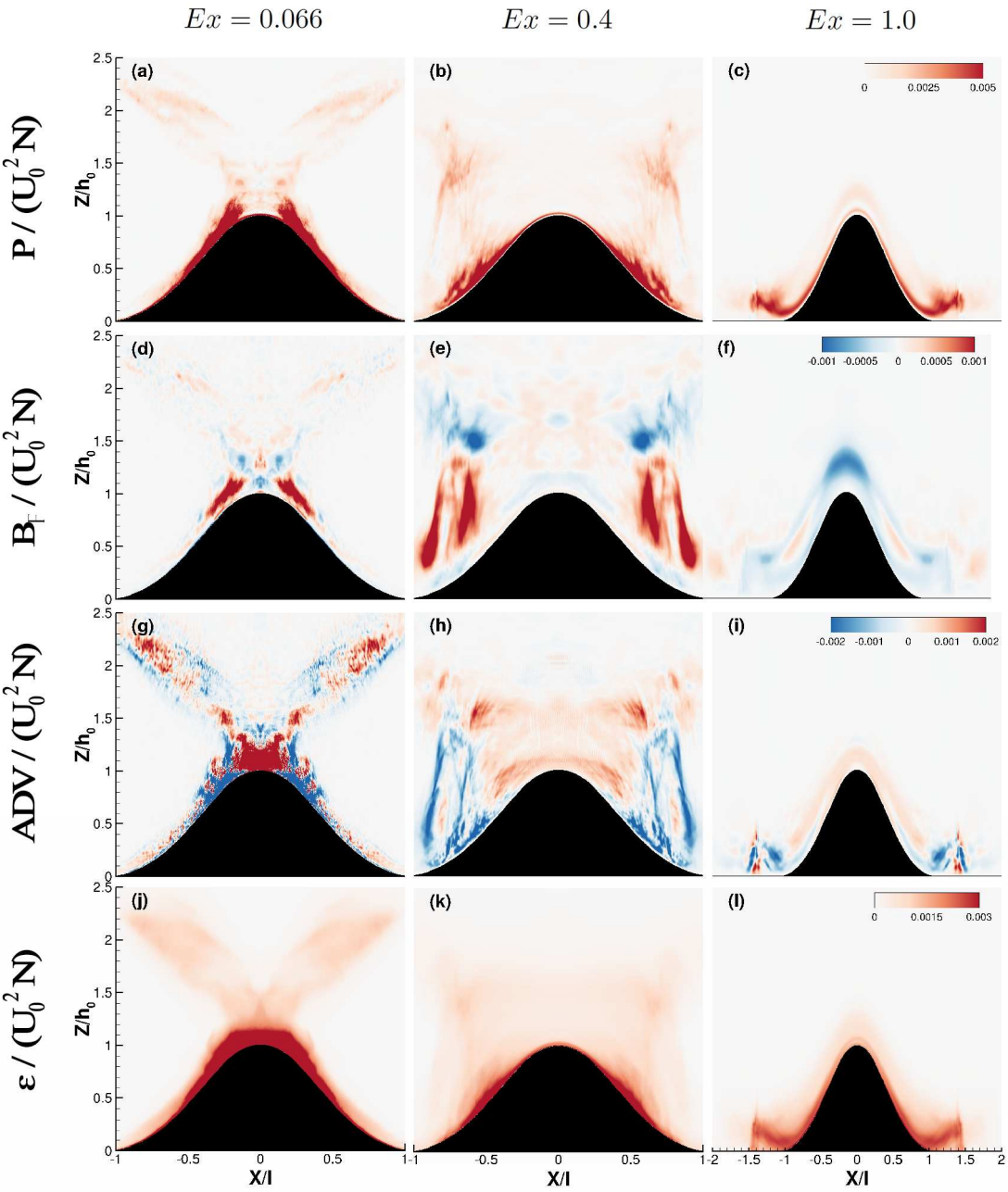

Figure 3.7: The spatial organization of cycle-averaged terms, normalized by $U_0^2 N$, in the TKE equation: (a-c) Production, (d-f) Buoyancy, (g-i) Advection, and (j-l) Dissipation. Left, middle and right columns correspond to Ex = 0.066, 0.4 and 1.0, respectively.

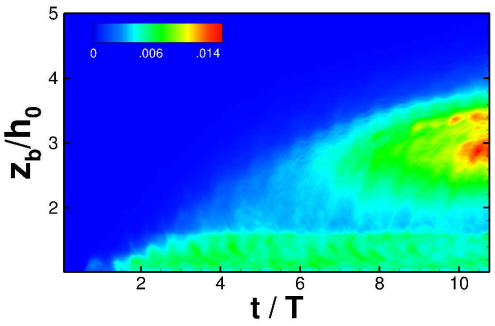

Figure 3.8: Temporal evolution of turbulence in the beam for case CEX1 ($Ex = 0.066$) with the normalized r.m.s. streamwise velocity, u_{rms}, used as the turbulence indicator. There are two beams as shown in figure 3.1 and u_{rms} at a particular z_b/h_0 is obtained by averaging over u_{rms} at points on the horizontal line $z = z_b$ that belong to either beam.

turbulence is present over the ridge throughout the cycle. Figure 3.9 (b) shows that there is a near-bottom region of turbulence that becomes thicker during flow reversal from down to up at $t/T = n$ (n integer) as well as a region of weaker turbulence that originates in the internal wave beam above the slope at $z/h_0 \sim 2$. At the summit (figure 3.9 a), beams from both flanks cross and the TKE is more extensive vertically and in time. The case with $Ex = 0.4$ has substantial near-bottom turbulence at midslope (figure 3.9d). The off-bottom peak at $z/h_0 \sim 2$ corresponds to a TKE patch from the opposite ridge flank being swept downslope while during the upslope phase there is an increase in TKE because of the upslope advection of the TKE patch that was initiated by the breaking lee wave. The case with $Ex = 1.0$ has strong turbulence when the barotropic velocity is large, either downslope or upslope.

3.4 Energetics of baroclinic response

The baroclinic energy budget is quantified to assess the change in wave energetics among cases CEX1 to CEX5. The contribution of each term in equation (2.25) is shown

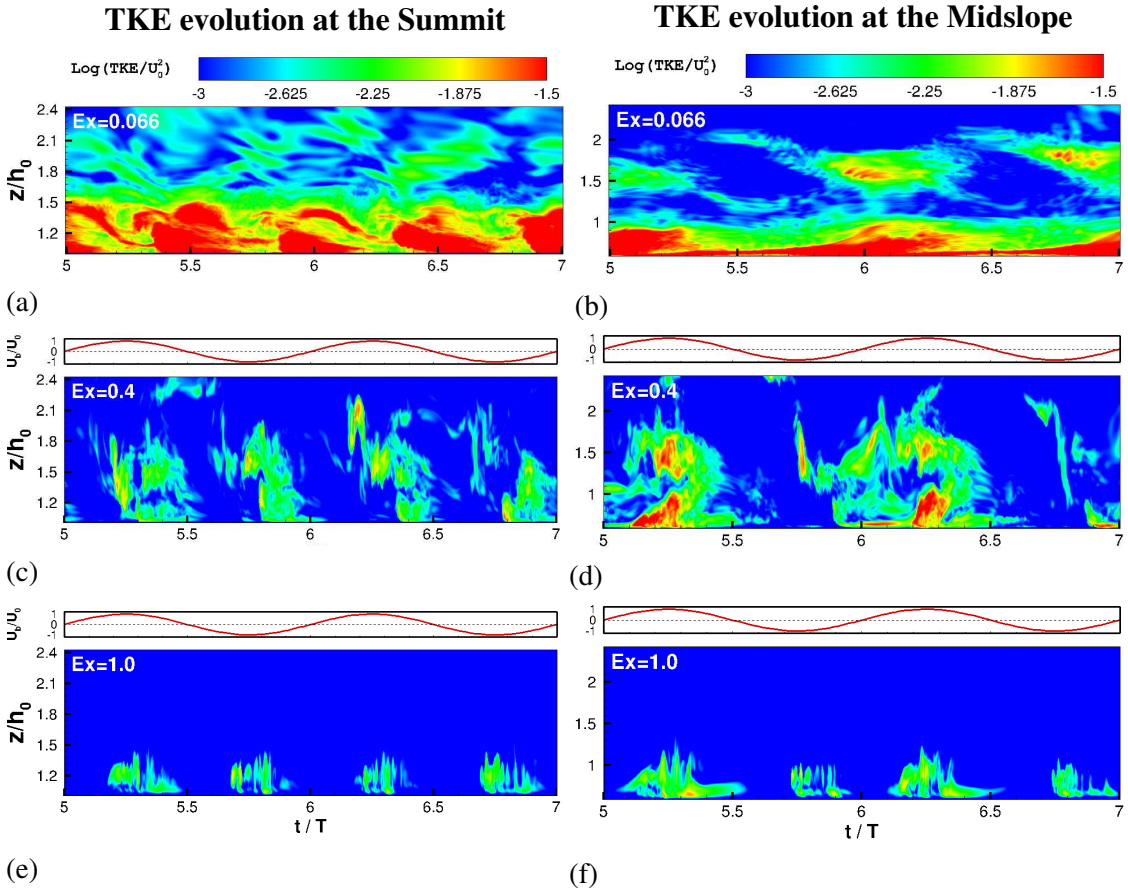

Figure 3.9: Temporal evolution of vertical profiles of $log_{10}(TKE/U_0^2)$ at the ridge summit (left column) and at midslope of the left flank (right column). Upper row corresponds to $Ex = 0.066$, middle row to $Ex = 0.4$ and bottom row to $Ex = 1.0$.

Table 3.2: Baroclinic energy budget. Each term in equation (2.25) is integrated over a box spanning $-1.57 < x/l < 1.57$ in the horizontal direction, averaged over the forcing time period at statistical steady state, and normalized by the factor $(\pi/4)\rho_0 U_0^2 h_0^2 \sqrt{N^2 - \omega_0^2}$ that appears in simplified analysis.

Case	Tendency	Conversion to waves (C)	Wave flux (M)	Baroclinic dissipation (ε_{bc})	Turbulent production (P)	Advection Flux (M_{ad})	Nonlinear Conversion (C_{nl})	Residual
CEX1	0.00291	0.622	0.555	0.0141	0.0350	0.00221	0.00102	0.0187
CEX2	0.00838	0.598	0.511	0.0350	0.0276	0.01493	0.00374	0.0050
CEX3	0.00109	0.574	0.463	0.0540	0.0215	0.04961	0.01540	-0.001
CEX4	-0.0029	0.604	0.474	0.0861	0.0184	0.07339	0.02249	-0.022
CEX5	0.00259	0.574	0.416	0.1185	0.0141	0.11418	0.03337	-0.058

in Table 3.2. The terms of the normalized budget shown in Table 3.2 are also plotted in Figure 3.10 (a) as a function of Ex. The primary inference to be drawn from this figure is the considerable drop in radiated wave flux, M. The increase in the advection term, M_{adv}, and the increase in baroclinic dissipation term, ε_{bc}, lead to both terms drawing more energy from the conversion C, leaving less available for radiation. Furthermore, C also decreases somewhat with increasing Ex. The larger barotropic forcing velocity U_0 leads to an increase in the advection term, M_{adv}, which is not surprising since M_{adv} is proportional to velocity cubed while the normalization factor is proportional to the velocity squared. The increasing importance of M_{adv} can be also explained as follows. In the linear case, there is a strong correlation between pressure and velocity. It can be recognized in the governing equation (2.1) because, in the absence of non-linear terms and molecular dissipation, the imposed pressure gradient term,$\boldsymbol{\nabla} p^*$, is fully used to accelerate a fluid particle, $d\boldsymbol{u}/dt$. Increasing the horizontal excursion of the barotropic background flow implies that a part of the pressure gradient term can no longer be used to locally accelerate the fluid particle but instead accounts for fluid inertia, $u_0.\nabla u$.

Assuming that the length scale of the velocity gradient remains constant among cases leads to the normalized baroclinic dissipation being proportional to $1/Re_s$. In the present simulations, Re_s is held constant but the normalized dissipation increases with increasing Ex. The reason is the enhancement in small scales associated with nonlinear wave steepening and wave breaking, as well as a larger horizontal extent of the dissipative region when the excursion number increases.

The conversion, C, from barotropic to baroclinic energy decreases somewhat (almost 8% at $Ex = 1$), although not as much as the decrease in M (almost 25% at $Ex = 1$), with increasing excursion number. It is also worth examining the widely used linear estimate of Bt-Bc energy conversion which simplifies the conversion term to the time average of following equation using the pressure and velocity from numerical simulation.

$$C^* = \int_x p^*(x,0,t)U(x,0,t)\frac{dh}{dx}\,dx \tag{3.5}$$

Figure 3.10 (b) shows the estimate of simplified conversion as well as the contributions from hydrostatic and non-hydrostatic pressure to this estimate. The simplified conversion shows little change with increasing Ex while the hydrostatic component increases with Ex. Reduction in the non-hydrostatic part compensates for the increase in the hydrostatic component and makes C^* approximately invariant to Ex. The hydrostatic pressure is computed using the density fluctuation from the background and subsequently the hydrostatic component is calculated as the time average of $\int_x (\int_z \rho^*(x,z,t)g\,dz)U_0\frac{dh}{dx}\,dx$.

Internal tides are though to be an important contributor to mixing in the ocean interior. Therefore, the fractional amount of barotropic energy converted to baroclinic

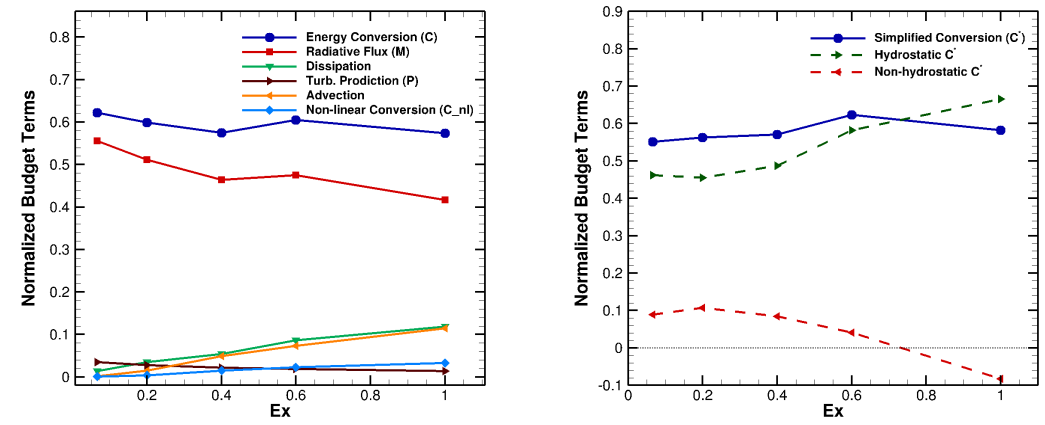

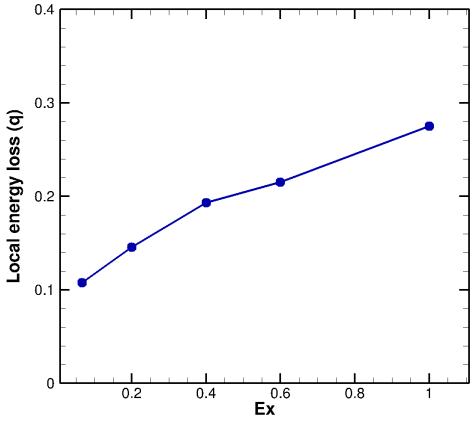

Figure 3.10: Effect of Ex on (a) baroclinic energy budget terms, (b) Simplified conversion term along with its hydrostatic and non-hydrostatic components. All terms are integrated between $x/l = \pm 1.57$ and normalized by $(\pi/4)\rho_0 U^2 h^2 \sqrt{(N^2 - \Omega^2)}$, and (c) Local loss of internal wave energy, $q = 1 - \frac{M}{C}$.

energy at topography that escapes as radiated internal waves is of interest. The quantity, $q = 1 - M/C$, is plotted in figure 3.10 (c). The local loss, q, increases to almost 0.3 at $Ex = 1$, a value that is thrice the value at low Ex.

We now discuss the spatial organization of the cycle-averaged terms involved in the baroclinic energy balance plotted in figures 3.11 (a)-(l). Each term in figure 3.11 shows a substantial decrease in the coherence of the beam pattern when Ex increases so that, in the cycle-averaged view, the beam is virtually absent at $Ex = 1$. The spatial organization of conversion is significantly affected by the excursion number. When Ex increases, a larger area is involved in the Bt-Bc conversion whereas, at low Ex, the conversion is dominant at the beams. It is remarkable that, although the spatial organization of the conversion term (figure 3.11 a-c) changes dramatically with increasing Ex, the change in its spatially integrated value in figure 3.10(a) is small and consistent with the trend in the linear estimate obtained from the boundary forcing. The dissipation plots are also noteworthy. As shown in Figure 3.11(g), baroclinic dissipation at low Ex occurs mainly in the boundary layer at critical slope and in the beams, both near the obstacle top and in the radiated tails. On the other hand, in the larger $Ex = 1$ case, baroclinic dissipation dwindles in the beam area and strengthens near the bottom, both at the sloping topography and the neighboring flat bottom region owing to breaking lee waves as will be discussed later. For better understanding of the decrease in M and C, the vertical profile of the amplitude of u_{bc} and P^*, and the amplitude of the correlation, $(P^* u)_{bc}$, computed at $x/l = -1$ are plotted. Figure 3.12 (a) confirms the previous discussion about diminished beam structure in the baroclinic velocity. Although the baroclinic pressure decreases in the beam region with increasing Ex, the magnitude at the boundary increases.

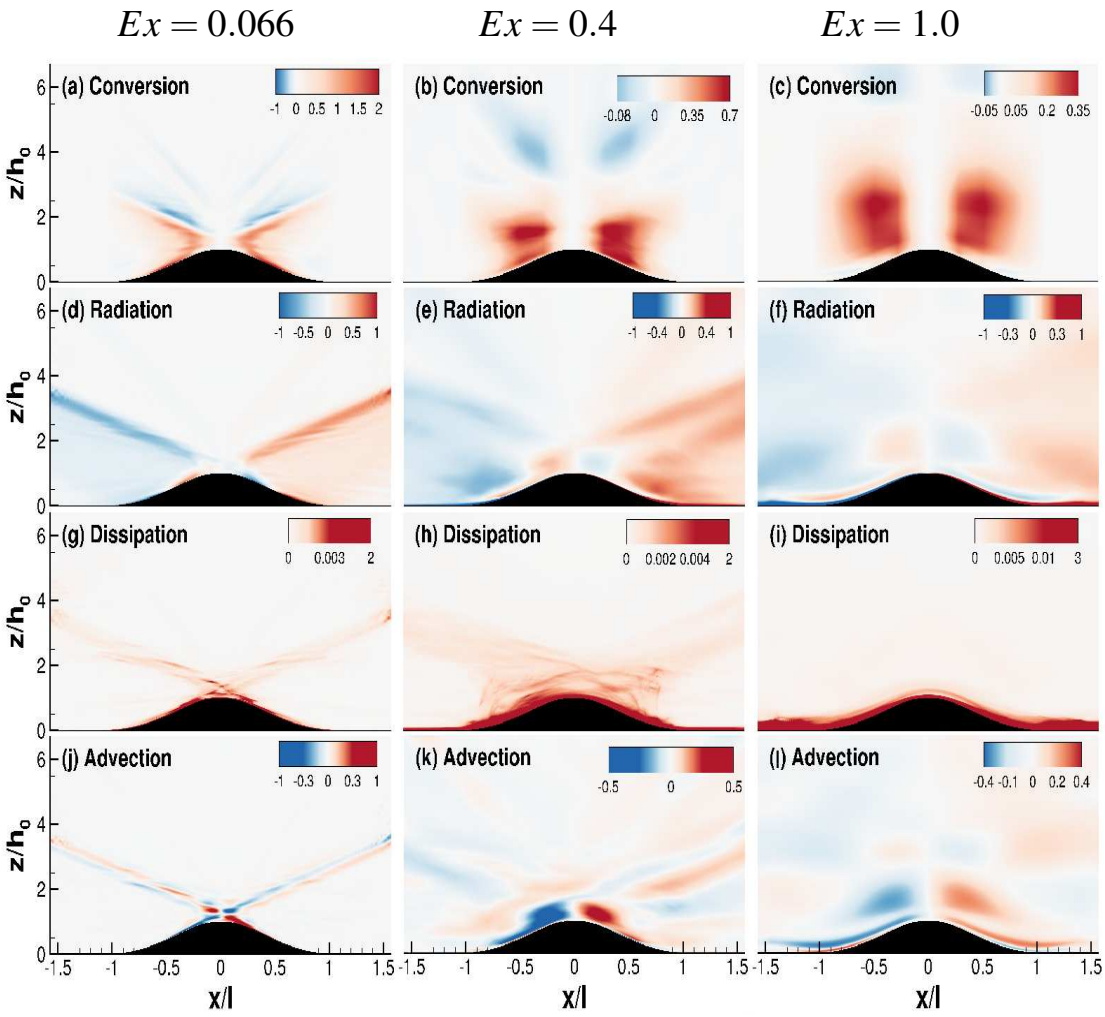

Figure 3.11: The spatial organization of cycle-averaged terms in the baroclinic energy balance normalized by $(\pi/4)\rho_0 U_0^2 h_0^2 \sqrt{N^2 - \omega_0^2}$.

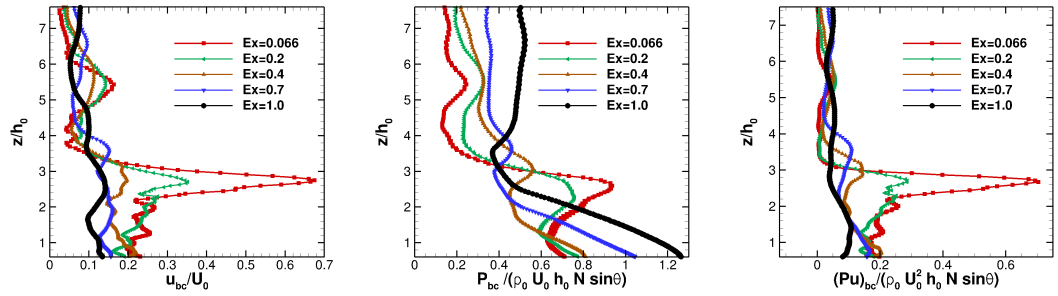

(a) (b) (c)

Figure 3.12: Vertical profiles of the normalized values of: (a) baroclinic velocity amplitude, (b) baroclinic pressure amplitude, and (c) the amplitude of the pressure-velocity correlation. Profiles shown at $x/l = -1$ for different Ex.

3.5 Conclusions

Three-dimensional direct numerical simulation is employed to investigate the effect of excursion number, Ex (the ratio of streamwise fluid advection length during a tidal cycle to streamwise topographic length scale), on the internal wave field and turbulence at a laboratory-scale obstacle with smoothed triangular topography. Ex is increased from 0.066 to 1.0 while Re_s, the Reynolds number based on the Stokes boundary layer thickness, is kept constant. In the previous work of Rapaka et al. (2013), the tidal forcing was systematically increased so that both Ex and Re_s increased and, moreover, the simulations were performed in the low Ex regime. Here, we focus on the independent effect of Ex when Re_s is held constant and, furthermore, explore the $Ex = O(1)$ regime. The topography chosen is that with a constant slope portion (20% of slope length) inclined at the critical angle. The present simulations provide new results summarized below from which we infer that changing Ex from small to O(1) values leads to qualitative changes in the wave field as well as in the near-field turbulence.

With increasing Ex, the beam structure of the radiated wave field becomes less evident, and the baroclinic intensification of velocity in both the boundary layer and the beams is reduced. The reason is that, when tidal excursion length increases, the fluid particle nominally on the critical slope is advected on to subcritical regions, attenuating the resonant wave response. In the present simulations with $Ex = 0.4$ and larger, visualizations show the presence of transient lee waves. At $Ex = 1$, lee wave phase lines can be clearly identified at birth and have inclination in close agreement with linear theory of steady lee waves. Evaluation of the cyclic-averaged barotropic energy budget shows a reduction of approximately 25% in the radiated wave flux at $Ex = 1$, which is attributed to increased baroclinic dissipation and the advective flux as well as reduction of

conversion. The numerically computed value of the linear approximation of conversion using boundary values remains almost invariant with respect to Ex. Interestingly, the hydrostatic component of the linear conversion increases when Ex exceeds 0.4 (when transient lee waves are identified), but this increase is compensated by a reduction in the non-hydrostatic component. The spatial distribution of cycle-averaged terms in the baroclinic energy budget is examined. The radiative flux, that is concentrated along the beams at low Ex, becomes less localized at high Ex. The baroclinic dissipation occurs in the beams at low Ex, unlike the situation at high Ex, where the baroclinic dissipation is much larger in the boundary layer.

Turbulence changes qualitatively among the cases with $Ex = 0.06$, 0.4 and 1.0. The $Ex = 0.066$ case has turbulence in the radiated beams. Advection of turbulent patches from the slope and intensified velocity shear lead to beam instability, which eventually becomes strong enough to generate turbulence in the radiated beam. TKE production (mainly by shear and to a lesser extent by buoyancy) is strongest at and above the critical slope, and advection distributes TKE from the slope to the crest. It is worth noting that, although cycle-averaged TKE production by buoyancy is small, it is the convective instability during flow reversal from down to upslope flow (Gayen and Sarkar, 2011a) that causes transition to turbulence over the entire height of the local boundary layer. The case with $Ex = 0.4$ has the tallest turbulent overturns, up to 2 obstacle heights from the flat bottom. The source in the TKE balance is TKE production, concentrated near the lower flanks, as well as the buoyancy, concentrated in the tall overturning regions adjacent to the topography that have vertical strain and gravitational instability. The overturns are initiated during flow reversal from downslope to upslope in the transient lee waves akin to the finding of Legg and Klymak (2008), although the nonlinearity in flow response has different origins: Ex based on the streamwise length of

the small obstacle considered here is $O(1)$, while Legg and Klymak (2008) consider large obstacles with low value of Ex but strongly supercritical slope leading to $O(1)$ values of Ex_{in}, based on a dynamically determined inner streamwise length scale (Winters and Armi, 2013) that is applicable near the crest. In the present simulation with $Ex = 1.0$, internal wave beams are nearly absent, the shear and strain in the upper water column is weak and, therefore, turbulence is limited to a near-bottom layer over the obstacle and adjoining flat bottom. The spatial organization of gradient Richardson number, Ri_g, shows close relationship to the TKE patches, indicating convective and shear instabilities in the corresponding regions. The temporal evolution and phase dependence of vertical profiles of density, velocity, and turbulence are also investigated and show differences between the slope and the crest as can be anticipated from the preceding discussion.

We conclude that small-scale topographies with energetic tides, corresponding to the regime of $Ex = O(1)$, are not as efficient radiators of internal wave energy as topographies with small Ex. The dependence of the local loss, q, of baroclinic energy is obtained without recourse to parameterization or artificially large numerical diffusivity in the present DNS study but the robustness of this result to larger, more realistic length scales needs to be established. Furthermore, the the influence of Ex in situations with supercritical topography needs examination through turbulence resolving simulations.

Acknowledgements

This chapter, in full, is a reprint of the material as it appears in "'Tidal flow over topography: effect of excursion number on wave energetics and turbulence", M. Jalali, N. Rapaka, S.Sarkar, *J.Fluid Mech.*, 750, 259-283, 2014. The dissertation author is the primary investigator and author of this paper. I am gratefully acknowledge the support of ONR grant N00014-09-1028.

Chapter 4

Tidal flow over model topography: Super-Critical ridges

The internal wave dynamics and turbulence at an isolated supercritical obstacle are investigated using three-dimensional, high resolution large-eddy simulations (LES) conducted with a body conforming grid. An obstacle with a smoothed triangular shape having supercritical slope is considered as a laboratory-scale model for a two-dimensional ocean ridge. Three simulations are performed with constant Reynolds number and an excursion number (Ex) that varies from 0.066 to unity, corresponding to a large obstacle and a small obstacle, respectively. The nonlinear flow features and turbulence mechanisms are studied and compared with critical slope simulations in the previous chapter

4.1 Problem setup

Fully nonlinear three-dimensional simulations are used to study an oscillating tide over a two-dimensional, triangular obstacle shown in figure 4.1. Background thermal

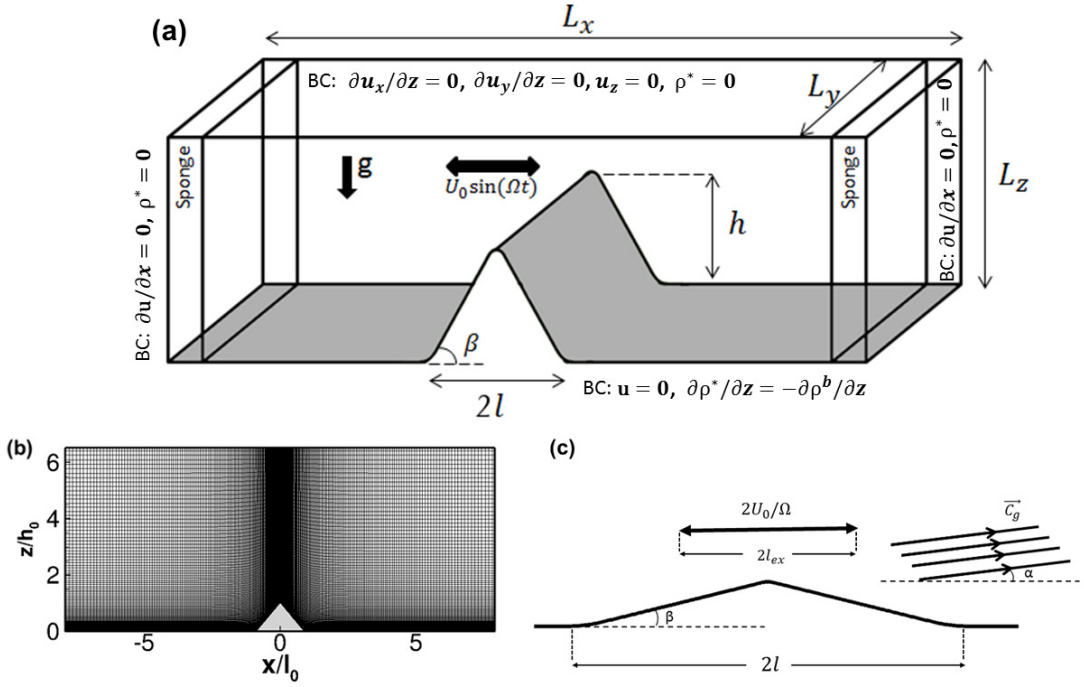

Figure 4.1: (a) Schematic (not to scale) of the problem of stratified, oscillating flow over a supercritical two-dimensional obstacle. Boundary conditions are also shown. (b) The body fitted computational domain, the grid has been shown partially with one of every three horizontal and vertical grid points. (c) Schematic of wave generation showing the wave propagation angle, α, topographic slope angle, β, excursion length, $2l_{ex}$, and topographic length, $2l$. In this panel $\vec{c_g}$ stands for group velocity.

stratification with a constant buoyancy frequency, N, is introduced while the bottom surface is assumed adiabatic. The background barotropic current, $U(x)\sin(\phi)$ with tidal phase, ϕ, is forced by an imposed horizontal pressure gradient that oscillates in time (t_d),

$$F_0(t_d) = \rho_0 U_0 \Omega \cos(\Omega t_d)\ . \tag{4.1}$$

The ridge is obtained by smoothing a triangular profile given by Equation (4.2) with $h = 0.4$ and $l = 1.5$. Its height is 0.328 m while the half-length, l, of 1.9 m is similar

Table 4.1: Key dimensional and nondimensional parameters of LES cases. The domain has streamwise length, $L_x = 30\ m$, height, $L_z = H = 2.62\ m$, and spanwise length, $L_y = 0.25\ m$. Topography length, $L_0 = 2l$, is 3.8 m and height, h, is 0.402 m. The critical angle is $\theta = 7^\circ$ while the slope angle is $\beta = 13.79^\circ$ and the tidal frequency is $\Omega = 1\ s^{-1}$. Steepness is $\gamma = 1.7$, and 77.5% of the slope is linear with $\varepsilon = \varepsilon_{max} = 2$. Prandtl number, Pr, is equal to 1.

Case	Ex	ε_{max}	$U_0[ms^{-1}]$	$\nu[m^2s^{-1}]$	$N^2[s^{-2}]$	Re_s	Fr_h	Ny	Nz	Nx
A	0.066	2	0.125	1.00e-6	67.33	177	0.038	64	321	897
B	0.4	2	0.76	3.68e-5	67.33	177	0.230	64	257	705
C	1.0	2	1.9	2.30e-4	67.33	177	0.576	64	257	705

to the profile used by Jalali et al. (2014); Rapaka et al. (2013).

$$z(x) = \begin{cases} h\left(1 - \frac{|x|}{l}\right) & \text{if } |x| \leq l, \\ 0 & \text{otherwise.} \end{cases} \tag{4.2}$$

The ridge has an overall steepness of $\gamma = 1.73$, about 77.5 % of the slope is linear with $\varepsilon_{max} = 2$, and the linear region blends smoothly into a subcritical region. The characteristic wave angle for all simulations is 7° with respect to the horizontal and the linearly sloping region has an angle of $\beta = 13.79^\circ$ leading to $\varepsilon = 2$.

Table 4.1 gives key parameters of the simulations. These cases are studied with Ex varying from 0.066 to unity, a relatively high Ex. The large value of $Ex = 1$ is appropriate for energetic tides over small-scale obstacles in the ocean. As mentioned previously, Ex is the ratio of excursion half-length, $l_{ex} = U_0/\Omega$ (half the horizontal tidal displacement of a fluid particle) to the characteristic half-width of the topography, l, as shown in Figure 4.1 (c). For example, in the case of an M2 tide with period 12.4 hours and velocity amplitude of 0.1 m/s, values of $Ex = U_0/\Omega l$ between 0.01 and 1 correspond to topographies with width between 142 km and 1.4 km. Topographic Froude number, Fr_h, on the other hand indicates the ratio of vertical displacement, U_0/N, based on energy considerations in a stratified fluid to the height of the topography, h.

Cases A, B, and C have $Re_s = 177$; the value of Ex (and therefore, Fr_h) is systematically changed among cases holding all other non-dimensional parameters constant. The value of $Re_s = 177$ is larger than in laboratory experiments of wave generation, but much smaller than oceanic values. The low Re_s has the advantage of allowing wall-resolved LES with sufficiently resolution of turbulence.

The LES model is used with case-specific grids. For instance, in Case B, a three-dimensional computational domain that enables the simulation of three-dimensional turbulent motions is discretized with 1,281 grid points in the streamwise (x) direction, 193 grid points in the vertical (z) direction, and 64 equispaced points in the spanwise (y) direction. The stretched grid has higher resolution near the bottom of the domain and ridge top as illustrated in Figure 4.1.

The simulations have adequate resolution of near-wall boundary layer turbulence and turbulence arising from convective overturns and wave breaking. The first grid point from the wall in Case A is located at $z_1^+ = 2$ (distance normalized by the viscous wall unit $\nu/\overline{u_\tau}$ based on average u_τ). Minimum grid resolution in the streamwise direction (Δx^+_{min}) is 22.3 and the spanwise direction has a uniform grid spacing of $\Delta y^+ = 17.6$ with spatial derivatives computed with spectral accuracy. The Ozmidov length scale, $L_O = \sqrt{\varepsilon/N^3}$, averaged over its values between the obstacle boundary and the height of active region, h_i, is calculated. At the phase, $\phi = \pi$, with largest overturns, the streamwise location with large convective overturns has average $L_O = 7\Delta z$, verifying that the Ozmidov scale is well resolved. The time step governed by the constraint, $CFL = 1$, is small with $\Omega\Delta t$ as small as 0.0007. Turbulent fluctuations are inferred from departures of instantaneous velocity, pressure, and density from the spanwise average. Statistics of turbulent quantities are a

function of x, z and t, and are computed via spanwise averaging.

4.2 Characteristics of the internal wavefield

Steep topography can have near-critical ($\varepsilon \approx 1$) regions with finite length while being overall subcritical ($\gamma < 1$), or be supercritical with critical points. Both types of steep topography have nonlinear flow response but due to different reasons as it will be explained in this chapter. We will contrast the effect of Ex in the present supercritical series with that found in our previous critical-slope series. Cases from Jalali et al. (2014) with the same Ex and Re_s as cases A, B and C are labelled as Cases A_{crit}, B_{crit} and C_{crit}, respectively. The model topography of Jalali et al. (2014) is an isolated, smoothed triangular obstacle, similar to the present simulations, with the same length $2l = 3.8$ m, overall subcritical ($\gamma = 0.64$), but with 20% of the streamwise length inclined at the critical angle.

Figures 4.2 compares the critical ($\varepsilon_{max} = 1$) and supercritical ($\varepsilon_{max} = 2$) simulations at the phase $\phi = \pi/2$ with maximum positive (rightward) velocity. At small $Ex = 0.066$, the critical case (figure 4.2a) exhibits intensified boundary layer flow over the entire obstacle while the supercritical case (figure 4.2d) shows flow blocking with zero velocity in a wedge between the obstacle flank and downward wave beams emanating from the critical points. Both cases show the fundamental wave beam as well as harmonics and interharmonics, that are especially sharp in the supercritical case. While beams are present in all simulations, two beams traveling downwards are unique to the supercritical cases. The maximum velocity (dark red patch in figure 4.2a) in the critical case occurs where the beams from the opposite flanks intersect. In the supercritical case, the maximum velocity (dark red patch in figure 4.2b) is at the obstacle peak and extends a short distance down the right (lee) flank. This is a signature of the downslope jet in the

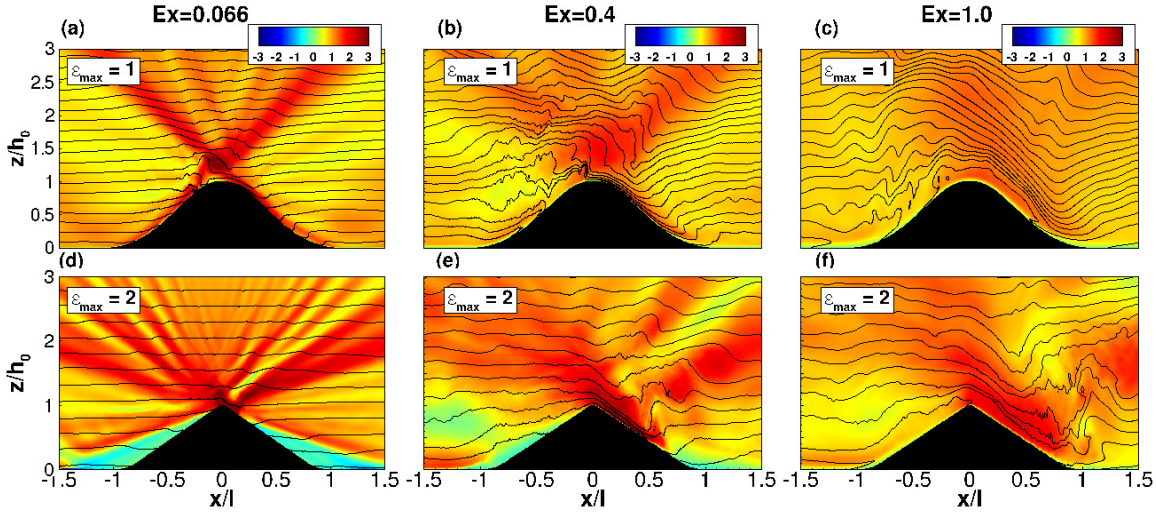

Figure 4.2: Streamwise velocity, U/U_0, and density isopycnals shown using contours and black lines, respectively. The phase corresponds to maximum positive (rightward) velocity with $\phi = \pi/2$. Subfigures (a), (b), and (c) correspond to critical cases while (d), (e), and (f) correspond to the supercritical cases A, B, and C respectively.

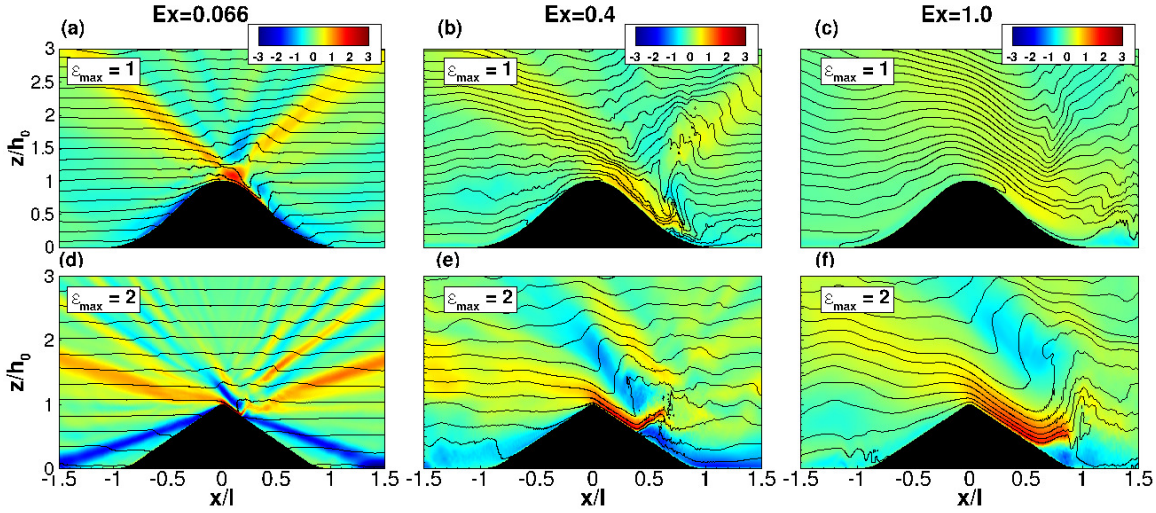

Figure 4.3: Streamwise mean velocity, U/U_0, and mean density isopycnals are shown using contours and black lines, respectively. The phase corresponds to zero velocity with $\phi = \pi$. Subfigures (a), (b), and (c) correspond to critical cases while (d), (e), and (f) correspond to the supercritical cases A, B, and C respectively.

lee of the obstacle that forms in all the simulated supercritical cases. The jet becomes thicker and travels further downslope with increasing Ex as can be seen in figures 4.2 (e) and (f). With increasing Ex, the asymmetry of the velocity increases in both critical and supercritical cases, and the wave beams become more diffuse.

Figure 4.3 is a comparison between critical and supercritical cases at zero velocity ($\phi = \pi$) at the point when flow reverses from positive to negative, i.e. downslope to upslope on the right, leeward flank. Consider the supercritical obstacle. At this phase of zero barotropic velocity, it is clear that fluid from the left of the obstacle crest is swept downslope on the right flank as a jet. The jet thickens and lengthens with increasing Ex while maintaining its integrity. The jet with downward momentum transporting lighter than background fluid is met by a baroclinic flow traveling upslope, at which time they interact to create a *rebounding jet* with large velocity perpendicular to the slope of the topography. As the jet rebounds, isopycnals steepen yielding overturns that become taller with increasing Ex. Lee waves with steep isopycnals are present. The amplitude of the lee waves increase with Ex so that by $Ex = 1$ there is significant isopycnal distortion well above the obstacle (Figure 4.3 f).

In a uniformly stratified fluid, flow with velocity U_0 has sufficient kinetic energy to overturn fluid spanning vertical displacements of U_0/N. At this point, all the kinetic energy has been converted to potential energy. As such, this ratio can be used to define a topographic Froude number, $Fr_h = U_0/Nh$. When $h > U_0/N$, i.e. $Fr_h < O(1)$, nonlinear effects become important in the flow over the obstacle. In particular, a steady current with $Fr_h < O(1)$ is host to a number of nonlinear hydraulic effects (Baines, 1995) including a fast moving layer with $Fr_h = O(1)$ due to acceleration of flow at the crest, blocking of the flow in the bottom layer deeper than $O(U_0/N)$ from the crest, and a hydraulic jump

where transition to subcritical flow is achieved in the lee. The transient downslope jet found in the present simulations with oscillating flow can be understood by analogy with the steady case.

Now consider the critical-slope obstacle shown in the top panel of figure 4.3. The boundary layer on the right flank has intensified velocity owing to the critical slope but the flow and the associated isopycnal pattern is different from the rebounding downslope jet seen in the supercritical cases. Critical-slope cases with $Ex = 0.066$ and $Ex = 0.4$ exhibit steep isopycnals and overturning motions over the obstacle. The overturning motions at $Ex = 0.066$ are associated with the boundary flow that is intensified owing to the critical-slope region while those at $Ex = 0.4$ are due to breaking lee waves.

Large steep supercritical ($\varepsilon > 1$) topography, e.g. the Kaena ridge or Luzon strait have attracted much interest because they are hot spots of internal wave generation. In such cases, the excursion number is small. Nevertheless, a strong nonlinear response is noted near the ridge peak as seen in observations as well as numerical models of oscillatory flow over supercritical obstacles. To clarify such behavior, Winters and Armi (Winters and Armi, 2013) introduced a characteristic topographic length scale denoted as the inner horizontal length scale, l_i, of the ridge corresponding to the vertical distance U_p/N from the ridge top where U_p is the ridge top velocity. Although Ex is small, the inner excursion number, $Ex_i = U_0/\Omega l_i$ can be O(1) leading to nonlinear flow features in the case of supercritical flow. The prediction of Ex_i from geometric and flow parameters is important. Let $I = U_p/U_0$ be the flow intensification at the ridge top. For a triangular ridge, Ex_i can be related to criticality and intensification of the flow as follows. The dynamically active depth from the ridge top, h_i, and corresponding inner length scale, l_i,

are

$$h_i = U_p/N = IU_0/N, \tag{4.3a}$$

$$l_i = \frac{h_i}{\tan(\beta)} = \frac{U_p}{N\tan(\beta)} = \frac{IU_0}{N\tan(\beta)} \tag{4.3b}$$

Therefore,

$$Ex_i = \frac{U_0}{\Omega l_i} = \frac{U_0}{\Omega I U_0/(N\tan(\beta))},$$

and finally,

$$Ex_i = \frac{\varepsilon}{I}. \tag{4.4}$$

Note that α (the angle of the phase line with the horizontal) satisifies $\tan\alpha \simeq \Omega/N$, a relationship that is used to obtain Eq. (4.4) from the preceding equation. A practical use of the relationship, $Ex_i = \varepsilon/I$, is to estimate the inner excursion number in the case of supercritical obstacles using the slope, background N, and a measurement of ridge-top velocity, without the direct measurement of active and inner length scales. Estimation of Ex_i facilitates prediction of nonlinear features and turbulence regimes in supercritical cases.

Table 4.2 shows good agreement between the theory presented in Equation 4.4 and simulation results. Intensification, $I = U_p/U_0$, is calculated using the maximum ridge-top velocity at phase $\phi = \pi/2$ for U_p. Further, h_i and l_i are defined as given by Equation (4.3). The inner length scale in the simulation, $l_{i,sim}$, can be directly computed as the width of the topography at the point where the flow velocity changes direction from downward to upward at the front of the jet. It is interesting to note that $l_{i,sim}$ agrees well with $l_i = h_i/\tan\beta$.

Table 4.2: Comparison between inner excursion (Ex_i in row 4) computed using Eq. (4.4) and the simulation value ($Ex_{in,sim}$ in bottom row). Note that I is computed from simulation. Case C has $Ex = 1$ and Ex_i is not dynamically relevant.

Parameters	A	B
$\varepsilon = \tan(\beta)/\tan(\alpha)$	2	2
$Ex = U_0/(l_o\ \Omega)$	**0.066**	**0.4**
$I = U/U_0$	6.0	3.5
$Ex_i = \varepsilon/I$	**0.330**	**0.571**
$h_i = I\ U_0/N[m]$	0.091	0.324
$l_i[m]$	0.374	1.339
$l_{i,sim}[m]$	0.395	1.377
$U_0[ms^{-1}]$	0.125	0.760
$Ex_{i,sim} = U_0/(l_{i,sim}\ \Omega)$	**0.314**	**0.552**

Case A in Table 4.2 is an example of supercritical topography with low Ex but larger Ex_i. As discussed, there is strong nonlinear behavior, e.g. downslope jet and wave breaking in Case A, despite the small value of outer excursion number, Ex. It will be shown in the next section that these nonlinear features lead to significant turbulence at the top of the ridge. The flow physics in case A is similar to that at oceanic sites like Luzon strait and Hawaiian ridge which have low Ex but a very active turbulent region close to their crest.

4.3 Turbulence

In simulations of a critical-slope obstacle in Chapter 3, changing Ex leads to a qualitative change in turbulence. The case with $Ex = 0.066$ hosts turbulence in radiated beams and the critical boundary layer. Intensified velocity in advected turbulence patches

leads to shear instability within the beam which eventually becomes strong enough to generate TKE within the beams. The source of turbulence for the case with $Ex = 0.4$ is the convective instability in the tall overturning regions associated with the upslope bore which has vertical strain as well as shear instability near the lower flanks. At $Ex = 1$, the response becomes increasingly asymmetric with shear in the boundary layer over the lee side. Here, wave breaking in the lee of the ridge occurs on the flat bottom, and these turbulent patches are advected back over the ridge.

An examination of the present supercritical regime also reveals qualitative changes with increasing Ex. In Case A, turbulence arises from several sources. In particular, there is a turbulence patch at the top of the ridge from the shear caused by the fast-moving, narrow flow at the ridge top. During the phase between maximum velocity and flow reversal, the intensified flow propagates as a downslope jet on the ridge flank, generating boundary layer turbulence due to shear. There is a secondary upward flow above the jet which itself acts as a source of shear instability at the jet boundary. This secondary flow intensifies turbulence in the jet region, resulting in a patch of turbulence larger than the downward jet. In the flow reversal phase, isopycnals are steepened by the rebounding jet, and the subsequent wave breaking creates a turbulence patch sized on the order of h_i which later advects to the top of the ridge. Additionally, turbulence due to shear is generated from the downward beams adjacent to the topography. Upward beams transfer turbulence patches within their ray paths.

In Case B, turbulence develops at the leading edge of the downslope jet. The jet is responsible for steep vertical overturns approximately h_i in size which result in a patch of turbulence extending from the boundary up to the height of the topography. Above the ridge crest, there is offslope lee wave breaking from steepened isopycnals which are

advected to the other side of the topography. As such, convective instability also plays a role in this case. Further, turbulence due to shear is generated as in Case A from the downward beam. However, velocity is less intensified than in Case A, so normalized turbulence within the beam is not as prevalent. Similarly, a weaker turbulence patch develops when the downward beam hits the bottom boundary.

In Case C, turbulence due to the downward propagating beam is almost negligible. However, wave breaking above the topography exists with a huge patch of turbulence attributed to convective instability. *S*-isopycals indicating Rayleigh-Taylor instabilities are seen right before flow reversal. These generate a patch of turbulence sized as large as h which advects upslope. The downslope jet exists, however, it is much thicker compared to the smaller Ex cases, leading to weaker shear and thus weaker boundary layer turbulence. Nonetheless, the jet plays an important role in instigating turbulence for this case too as isopycyncals are distorted by the relative shear created with respect to the secondary upward flow and when the jet rebounds as it collides with the upslope boundary flow. All turbulence patches are advected and connect to create a single sizable region of turbulence extending up to h above the ridge crest. Thus, in the $Ex = 1$ case, there is more turbulence attributed to wave breaking as opposed to internal wave beam or boundary layer shear.

Figure 4.4 depicts the time-averaged turbulent kinetic energy normalized by U_0^2 for the critical and supercritical cases. Subfigures (a), (b), and (c) show that the spatial pattern of turbulence changes remarkably with increasing Ex. The pattern at $Ex = 0.066$ shows boundary layer turbulence associated with critical-slope dynamics as well as turbulence aloft in the wave beams. In contrast, the $Ex = 1$ case exhibits turbulence only in a relatively thin boundary region including the flat bottom adjacent to the obstacle.

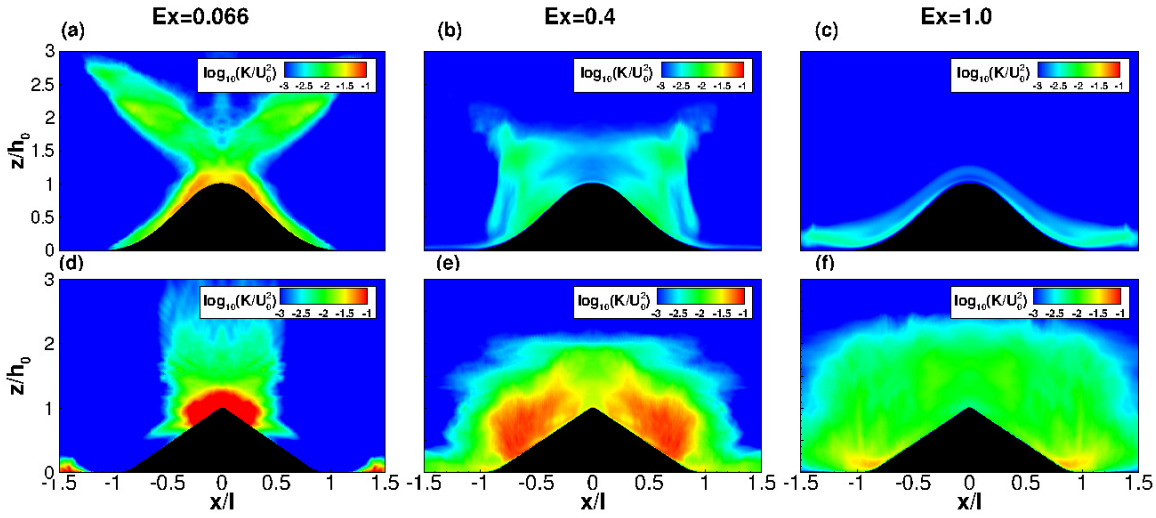

Figure 4.4: Time-averaged turbulent kinetic energy normalized by U_0^2. Subfigures (a), (b), and (c) correspond to critical cases while (d), (e), and (f) correspond to the supercritical cases A, B, and C respectively.

The intermediate case with $Ex = 0.4$ has a broad and tall (about $2l$ by $2h$) turbulent region that is fueled by breaking lee waves as well as shear associated with the upslope bore.

The spatial distribution of time-averaged TKE for the supercritical cases, shown in the lower panel of 4.4, is quite different from that for the critical cases shown in the top panel. The downslope jet and breaking lee waves are the significant contributors to turbulence in the supercritical cases. At low $Ex = 0.066$, there is no clear signature of internal wave beams as was present in the critical case at low Ex. However, instantaneous visualizations do show TKE at specific times along the ray paths of the beams at the fundamental frequency, especially the downward propagating family, as well as within the superharmonics and interharmonics that were evident in the velocity field (figures 4.2 d and 4.3 d). The shear in the jet, convective overturns during the jet rebound, and breaking lee waves create a zone of intensified TKE over the ridge top with $K/U_0^2 = O(0.1)$ that extends down to $h_i = U_p/N$. There is also a surrounding layer of weaker TKE, associated with shear in the wave beams and advection of TKE, that extends to almost h above

the ride top. Unlike the critical case, there is little TKE on the ridge flank below the active region of $h_i = U_p/N$. The downward wave beam interacts with the flat bottom to create some turbulence. The active height h_i increases with increasing Ex and so does the span of the turbulent region below the ridge top as can be seen from subfigures (e) and (f). Case B has a broader jet and smaller normalized value of K/U_0^2 relative to case A, however, since the area occupied by the turbulence is larger in case B, so is the area-integrated, normalized TKE. The case with the largest excursion number, Case C, has a sizable turbulence region although the jet is not as strong, resulting in less intense shear and wave breaking. In case C, both the local magnitude and the overall area-integrated value of the normalized turbulence region are smaller than in case B.

4.4 Energetics of baroclinic response

Table 4.3 shows the normalized, cycle-averaged terms from the energy budget in equation (2.25), integrated over the computational domain. The last column in Table 4.3 reports the value of local loss, given by $q = 1 - M/C - (\partial E/\partial t)/C$. It is the fractional amount of barotropic energy converted to baroclinic energy that does not escape as radiated waves. While the temporal change in the cycle-averaged variable is only about 1% of the conversion term, it is still relevant to the calculation of the local loss energy. In contrast to linear inviscid theory, which assumes all converted energy resides in the internal wave field, a significant local loss is expected in the supercritical cases.

The first trend to note in Table 4.3 is the considerable drop in linear energy conversion, C_l, in the higher Ex supercritical cases while the critical cases possess no such drop. Though smaller values of conversion naturally lead to reduced values of

radiated wave flux, M, the drop in this flux term is not proportional to the drop in C_l. Some of the drop in M can be attributed to increases in the advection term, M_{adv}, baroclinic dissipation, ε_{bc}, and turbulent production, P. These terms draw energy from conversion, C, thereby leaving less energy available for radiation. The combination of these factors leads to a significant increase in the local loss, q, especially in cases B and C.

In Cases A, B, and C with low, moderate, and high tidal velocities respectively, the local loss q increases from 10% to 46%, a trend reflecting the increase in turbulent production and baroclinic dissipation. From the present simulations, it is clear that small (high Ex) obstacles have considerably more local loss than large (low Ex) obstacles, both having the same supercritical slope. In addition, large obstacles with small Ex have larger normalized conversion, leading to larger normalized radiated wave flux.

Production by the Reynolds stresses transfer wave energy to TKE. Similar to normalized integrated TKE, the production term is the largest in case B followed by Case C. However in critical cases, normalized TKE exhibits a monotone decrease with increasing Ex, consistent with the drop in turbulent production for these cases.

In both critical and supercritical cases, normalized baroclinic dissipation increases with excursion number. Denoting the length scale of the velocity gradient as l_{bc} and estimating the baroclinic velocity as IU_0 where I is the intensification leads to $\varepsilon_{bc} \sim \nu(IU_0/l_{bc})^2$. Introducing the definition of Re_s allows elimination of ν so that $\varepsilon_{bc} \sim I^2U_0^4/(\Omega Re_s^2 l_{bc}^2)$. Note that Re_s and Ω are constant among cases and that the normalization factor contains U_0^2. Therefore the normalized baroclinic dissipation varies among cases as $(IU_0)^2/l_{bc}^2$. The normalized baroclinic dissipation is found to increase with tidal forcing in the simulations but at a rate which is somewhat lower than $(IU_0)^2$

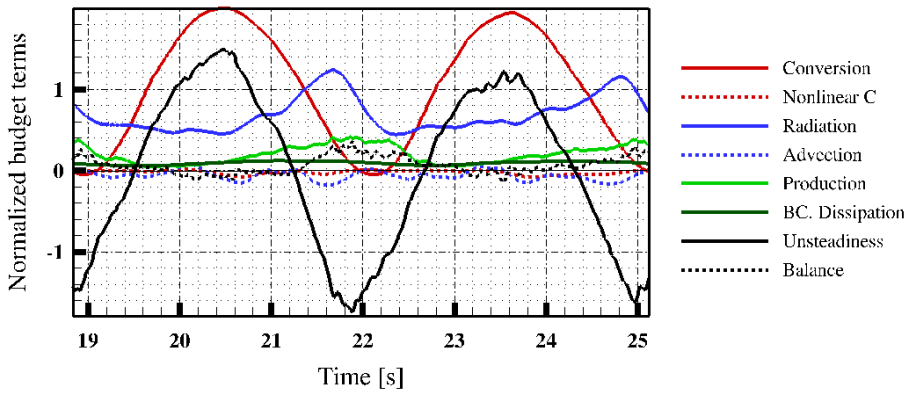

Figure 4.5: Evolution of normalized, area-integrated terms of barotropic to baroclinic energy conversion equation over the computational domain for Case B.

because of the increase of l_{bc} among cases.

The nonlinear part of the conversion term becomes larger from Case A to Case C because stronger forcing makes the flow field more nonlinear. At the same time, M_{adv} is proportional to U_0^3 while the normalization factor is proportional to U_0^2. Thus, one would expect a larger barotropic forcing to correspond to an increase in the normalized advection term as is seen here.

4.5 Conclusions

Steep topography that is supercritical (slope larger than that of the internal wave phase line) has higher conversion from barotropic tidal energy to internal wave energy relative to subcritical obstacles. At the same time, steep topography also facilitates nonlinear waves and turbulence that potentially increases local losses. Wave generation has yet to be studied systematically with turbulence-resolving simulations for supercritical topography motivating the present study. We perform three-dimensional, high

Table 4.3: Baroclinic energy budget. Each term in baroclinic energy equation is cycle-averaged and integrated over the computational domain. The critical cases noted as A_{crit}, B_{crit}, and C_{crit} are referenced from Jalali et al. (2014). All terms are normalized by the factor $H_N = (\pi/4)\rho_0 U_0^2 h^2 \sqrt{N^2 - \Omega^2}$ used in linear theory.

case	C_l	C_{nl}	M	M_{adv}	P	ε_{bc}	$\partial E/\partial t$	residual	q
A_{crit}	0.622	0.001	0.555	0.002	0.035	0.014	0.003	0.019	0.103
A	1.291	0.005	1.172	0.038	0.092	0.014	-0.011	0.067	0.100
B_{crit}	0.574	0.015	0.463	0.050	0.022	0.054	0.001	-0.001	0.192
B	1.020	-0.023	0.694	-0.061	0.197	0.090	0.015	0.064	0.308
C_{crit}	0.574	0.033	0.416	0.114	0.014	0.119	0.003	-0.059	0.271
C	0.777	0.046	0.402	0.170	0.147	0.141	0.012	-0.050	0.467

resolution LES in a body fitted coordinate system. A smoothed triangular obstacle with slope criticality of $\varepsilon = 2$ is taken as a laboratory scale model of a ridge and three cases with increasing tidal velocity (cases A, B and C with excursion number of $Ex = 0.066$, 0.4 and 1, respectively) are simulated for a constant Reynolds number based on the nominal Stokes boundary layer thickness. The results are contrasted with cases from a previous study (Jalali et al., 2014) of an obstacle with similar triangular geometry, overall subcritical ($\gamma = 0.64$), but with 20% slope at critical angle that was conducted at the same Reynolds number and a similar range of Ex.

In the supercritical problem, the dominant nonlinear feature is a jet that forms as an accelerated layer at the ridge top and flows downslope over a vertical height, h_i. The height, h_i, can be estimated on energetic grounds and is approximately IU_0/N (Winters and Armi, 2013) where U_0 is the amplitude of the oscillating tide, I is the baroclinic velocity intensification at the ridge top, and N is the background stratification. Furthermore, during the flow reversal phase for all cases, the downward jet encounters an upward flow, resulting in a *rebounding jet* which pushes isopycnals upward and creates

convective instability. In Case A, there is a short jet at the top of the ridge, internal wave beams including two downward beams, and pronounced superharmonics. As Ex is increased, the superharmonics and downward beam structures become less coherent. The length and thickness of the jet increase with increasing Ex even though the intensification of the velocity decreases from its value of $I = 6$ at the low $Ex = 0.066$. Therefore, as Ex increases, the nonlinear behavior is characterized more by transient convective overturns than jet features. The inner excursion number, Ex_i, is an important determinant of nonlinear wave behavior and turbulence in the case of supercritical obstacles. An analytical estimate of $Ex_i = \varepsilon/I$ is derived and simulation data support this result.

There are two primary mechanisms responsible for turbulence at a supercritical wave generation site, notably shear in the downslope jet and convective instabilities. Convective instabilities arise from steepened isopycnals and wave breaking as the flow reverses from down to upslope. Other mechanisms such as shear in the superharmonics and downward beams are also present though not as prevalent. Turbulence patches generated via these mechanisms are advected over the topography. For Case A, there is an intense, active region at the top of the ridge. As Ex increases, this region becomes larger but the local normalized TKE is smaller. Case B yields the largest area-integrated normalized TKE of all cases.

The small-scale waves and abundant turbulence in the supercritical problem have considerable impact on the wave energetics. With increasing Ex, there is a substantial decrease in the normalized energy conversion (C) from the barotropic tide to the baroclinic wave field as well as an increase in the local energy loss (q) that measures the fraction of converted energy that is not transported away by internal waves. This finding is supported by the loss of beam structure with increasing Ex as well as the increasing

fraction of turbulence production and viscous dissipation of the wave field.

The normalized wave radiation (M) in the supercritical wave generation problem is almost twice that for the near-critical problem when the excursion number has a low value of $Ex = 0.066$. At this low Ex, the loss is $q \approx 0.1$ in both problems. Although the obstacle is overall subcritical ($\gamma = 0.64$) and the flow has low Ex, the presence of a critical slope with 20% of the streamwise length is sufficient to increase the loss to that for the supercritical problem. With increasing Ex, the value of M decreases for both problems but with a faster rate for the supercritical problem so that by $Ex = 1$ the supercritical problem has slightly smaller M relative to the critical-slope case. As shown by Table 4.3, the large decrease of M with increasing Ex in the supercritical problem is both due to reduced conversion C and increased loss q. Insofar as near-field turbulence, it has larger normalized TKE (both magnitude and area-integrated) in the supercritical problem. An important distinction is that, as a function of increasing Ex, the normalized TKE increases in the supercritical problem as opposed to the decrease exhibited by normalized TKE in the critical-slope problem.

Based on the preceding summary, we conclude that large (horizontal length scale is large with respect to tidal excursion length), supercritical isolated obstacles with small Ex effectively radiate wave energy while small, supercritical obstacles with $Ex = O(1)$ are effective in hosting local turbulence. We note that the present simulations are of an isolated feature at low Reynolds number and the robustness of our conclusion to higher Reynolds number and more realistic, multiscale topography needs further investigation by turbulence resolving simulations. Three cases corresponding to $Ex << O(1)$, $Ex = O(1)$ but less than unity, and $Ex = 1$ were simulated. The inclusion of additional cases in future studies will help refine the quantitative estimates of energy loss, q, and conversion,

P, to turbulence obtained here.

Acknowledgements

This chapter, in full, is a reprint of the material as it appears in Oscillatory stratified flow over supercritical topography: wave energetics and turbulence", M. Jalali, A. VanDine, V.K. Chalamalla, S.Sarkar, *Comput. Fluids*, 0045-7930, 2016. The dissertation author is the primary investigator and author of this paper. I am gratefully acknowledge the support of NSF Grant OCE-1459774.

Chapter 5

Tidal flow over realistic topography: Luzon strait

Luzon Strait is a strong internal tide generation site with broad rough topography, as illustrated by the transect at $20.6°N$ (Figure 5.1(a)). It is a double-ridge system with each primary ridge having smaller subridges and topographic bumps. A semidiurnal oscillating tide over a section of the Luzon Strait is studied using fully nonlinear, three-dimensional LES. The model is a nondimensional setup of a realistic geometry located over an approximately 40 km long region of the west ridge (shown with a box in figure 5.2(a)) at $20.6°N$ that contains station N2, a site of the observational study in 2010 whose data will be compared with the present simulations. The topography shown in Figure 5.2(c) corresponds to high-resolution bathymetry used by Buijsman et al. (2012), and was extracted from a global topography bathymetry grid (SRTM30 PLUS) with a resolution of 30 arc seconds, as well as the Smith and Sandwell database. Our focus in this study (Jalali and Sarkar., 2017) is on the west ridge and in particular the two subridges boxed in figure 5.1. The eastern subridge with mooring N2 is referred to as the main subridge.The stratification has a realistic shape based on Buijsman et al. (2012).

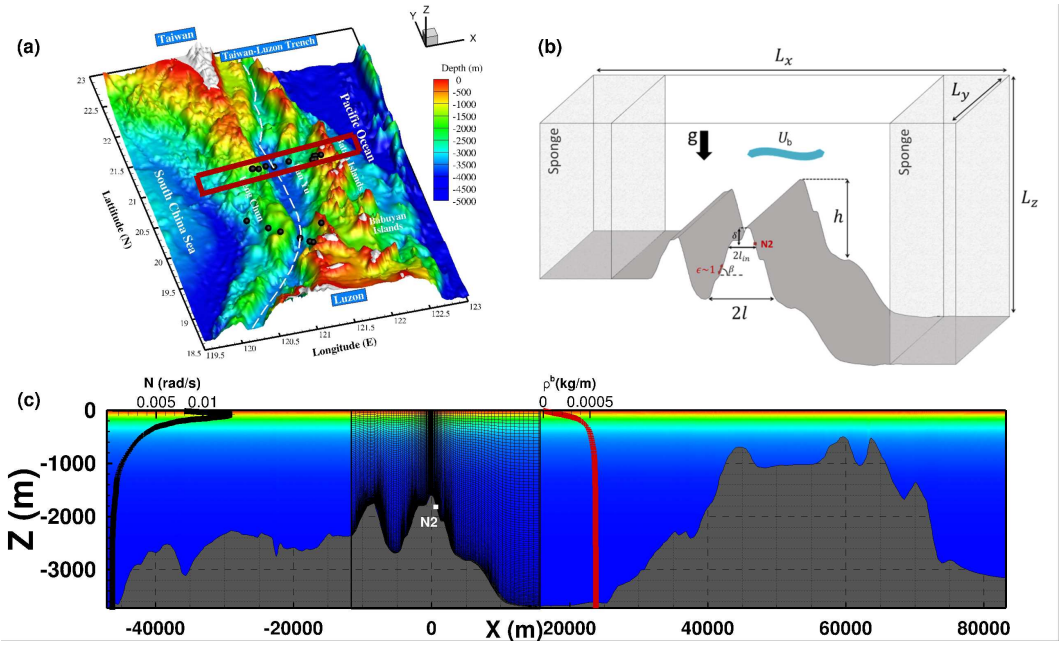

Figure 5.1: (a) The double-ridge Luzon Strait. (b) Schematic of the model problem. (c) East-west cross section of the double-ridge Luzon Strait at 20.6°N. Vertical profiles of the density and buoyancy frequency at measurement station N2 are given. The model domain with the body-fitted grid (shown partially with one of every ten horizontal and one of every two vertical grid points) is also shown.

5.1 Problem setup

The LES model is applied to simulate flow at topography that is two-dimensional. A three-dimensional computational domain that enables the simulation of three-dimensional turbulent motions is discretized with 1,281 grid points in the streamwise (x) direction, 193 grid points in the vertical (z) direction, and 64 equispaced points in the spanwise (y) direction.The stretched grid has higher resolution near the bottom and also near the ridge top as illustrated in figure 5.2 (b).

The details of the LES model implementation were discussed in Chapter 2. Rotation is not considered for simplicity as it is not considered crucial to near-obstacle turbulence processes at low latitudes where the internal tide propagates away freely. The combination of strong tidal forcing and steep slopes leads to strong turbulent motions at and above the topography. Nonlinear wave-wave interactions present in the case of rotation are expected to lead to weaker turbulence but their influence on the flow is worth future examination.

The model is designed to keep the following *non-dimensional* parameters excluding *Re* the same in the model and the ocean: Excursion number $Ex = U_0/(\Omega l)$, slope criticality $\varepsilon = \tan(\beta)/\tan(\alpha)$, topographic Froude number $Fr_h = U_0/(N_\infty h)$, depth ratio h/H, and frequency ratio Ω/N_∞. In the definition of criticality, α is the angle of internal wave phase line with the horizontal given in a non-rotating environment by $\alpha = \sin^{-1}(\Omega/N_\infty)$ with β being the local slope angle. *Normalized coordinates*, $\bar{x} = x/H$, $\bar{y} = y/H$ and $\bar{z} = z/H$ where H is the maximum depth of the modeled section, are used to present results.

The values of non-dimensional variables for the Luzon transect considered here are computed using the following characteristic values: $U_0 = 0.132$ m/s which is the average of the maximum and minimum tidal velocity measured at N2, the M2 tidal frequency of $\Omega = 1.405 \times 10^{-4}$ s^{-1}, the buoyancy frequency of $N_\infty = 0.0011$ s^{-1} at the N2 mooring bottom, the maximum ocean depth of $H = 3694$ m, the height of the main sub-ridge crest $h = 2100$ m and length of the transect $l = 40,000$ m. The model matches the following non-dimensional parameters of the Luzon transect: $Ex = 0.047$, $Fr_h = 0.057$, $h/l = 0.052$, and $h/H = 0.56$. Although the model $Re = 6.28 \times 10^4$ is smaller than the oceanic value of $Re = 1.24 \times 10^8$, *Re* is still sufficiently large to realize nonlinear waves

and turbulence. It is worth noting that Winters (2015) used a nondimensional setup to simulate turbulence during reflection of a mode-1 tide and converted their results to compare with the Bay of Biscay measurements of temperature at a bottom mooring by van Haren (2006) that had shown upslope bores with thermal fronts with approximately the tidal frequency. A sponge layer is added at the western and eastern boundaries to minimize spurious reflections. The model case is simulated with 2D topography in a 3D domain, discretized with 1,281 streamwise (x) points and 193 points in the vertical (z) direction. The stretched grid has higher resolution near the bottom and also near the main subridge top. The spanwise (y) domain of nondimensional length 0.65 (oceanic length of 2400 m) is discretized with 64 equispaced points. The turbulence is mostly associated with overturns detached from the boundary and 5 or more points spanning the Ozmidov length (as large as 20 m) provide good resolution of these overturns. The resolution of the present non-dimensional LES setup corresponds to length-scales of about 2.4 m vertically and 4.8 m in the x direction near the top of the main subridge.

We do not model both ridges of Luzon since the available computational resources are insufficient to do so while still resolving turbulent processes. Instead, we force the tidal flow at the west ridge with an oscillatory body force to match the observed barotropic velocity at $N2$ and study *local* generation of internal waves. The background forcing is obtained by using two periodic modes (the dominant semi-diurnal frequency Ω_{M2} and the diurnal frequency Ω_{O1}) and a westward current: $U_b(t_d) = A_{M2}sin(\Omega_{M2}t_d + \Phi_{M2}) + A_{O1}sin(\Omega_{O1}t_d + \Phi_{O1}) + A_0$ where the amplitudes and phase differences extracted from curve fitting the measured barotropic velocity at $N2$ (Figure 5.2 d) are $A_{M2} = 0.0889$, $A_{O1} = -0.0091$, $\Phi_{M2} = 2.7275$, and $\Phi_{O1} = 1.7593$. In order to facilitate comparison with observations, simulation time is converted to phase as $t = (t_d - t_0)\Omega_{M2}$, setting $t_0 = 292.2$ [year-day].

5.2 Velocity and Turbulence fields

The temporal and spatial structure of the flow (Figures 5.2-5.5) at the west ridge shows small-scale nonlinear waves and tall turbulent overturns that are generally consistent with observations (Alford et al., 2011). The time evolution of the velocity profile at station N2 is compared between observations (Figure 5.2a) and simulation (Figure 5.2b). Spatial snapshots of simulated velocity are shown in Figure 5.3 (a)-(b) to help understand the flow. Three important tidally-modulated features are identified: First, Figure 5.3 (a) shows that a beam that originates from the the left (west) of the main subridge centered at $\bar{x} = 0$ crosses the N2 mooring at $\bar{z} \approx -0.3$ (A2* in Figure 5.3a). The beam velocity magnitude exceeds thrice the barotropic velocity amplitude, U_0. The inclined beam advects westward over the ridge and, correspondingly, the high velocity region in the N2-mooring time series (feature A2 in Figure 5.2b) at station N2 moves downward with increasing time. Second, an additional beam originates from the other sub-ridge centered at $\bar{x} = -4.1$ and crosses the N2 mooring at $\bar{z} \approx -0.2$ (A1 in Figure 5.2b). The A1 feature moves downward with increasing time (phase) in Figure 5.2 (b) owing to advection. Note that similar beam features, indicated by B1 and B2, also form during the eastward ($U > 0$) phase of the tide. Third, there is intensified velocity (marked by B3 in Figures 5.2b and 5.3b) close to the bottom of the topography owing to the tail of a jet (shown in Figure 5.3 d, inset) that forms at the main subridge crest and sweeps downhill toward N2 increasing the recorded velocity.

Comparison with the measurements in Figure 5.2 (a) reveals generally good agreement of the spatial structure and phasing of the velocity and isopycnal displacements. For example, A2 and B2 in the simulated velocity correspond to A$'$2 and B$'$2 in the observations, respectively. Despite this agreement, the absence of the east ridge in the

model has a consequence, namely the constructive resonance between the wave generated at the east ridge and the locally generated wave at N2 (Buijsman et al., 2012) is lacking. This absence and the simplifications in the forcing lead to near-bottom velocity (B3) that is less powerful than in observations. Also, there are more small-scale fluctuations in the observed isopycnals and velocity relative to the lower-*Re* model.

The turbulent dissipation rate, ε, reported by Alford et al. (2011) is a Thorpe-scale estimate. In the simulation, ε was computed directly as the sum of resolved and subgrid dissipation from the model and also as a Thorpe-scale estimate using the same method as Alford et al. (2011). Figure 5.2 (c) shows vertically-integrated ε. The Thorpe-scale ε has similar values in the simulation (black curve) and observation (blue curve with symbols), although the spike at $t = 2.5\pi$ in the observation from B3 is absent in the simulations. The vertically-integrated ε calculated directly from the LES model (red curve) is also plotted. The Thorpe estimate is larger than the LES model dissipation. There is an ongoing discussion about the applicability of the Thorpe-sorting estimate in regions which have turbulence predominantly from convective instabilities as discussed by Mater et al. (2015); Scotti (2015); Jalali et al. (2017).

Figures 5.3 (a)-(b) show the spatial structure of the velocity, U, in the x-direction. Coherent internal wave beams with velocity much larger than U_0 radiate from the topography and interact with the upper-ocean pycnocline. There are distinct wave beams corresponding to the primary tidal forcing as well as rays corresponding to harmonics and interharmonics. Figure 5.3 (c) shows TKE at the same phase as in Figure 5.3 (a). There is turbulence associated with the wave beams corresponding to features A1 and A2 as they emanate from the obstacle and also farther up as they interact with the higher stratification of the upper ocean. At the beams and in the vicinity of generation, the

dominant mechanism is shear instability evidenced by regions with $Ri_g < 0.25$, although visualizations show that TKE patches from different regions can also get advected by the strong baroclinic velocity. In addition, other instabilities such as parametric subharmonic instability (PSI) (Gayen and Sarkar, 2014) can also lead to turbulence, specifically during beam refraction through the pycnocline. TKE is intensified where the IW beam hits the pycnocline.

Figure 5.3 (d) depicts TKE at the same phase as in Figure 5.3 (b). The inset, a magnified view of the region near station N2, shows velocity vectors corresponding to a jet that flows across and down the eastern side of the ridge crest towards N2. The TKE is intensified in the jet. The enhanced TKE is associated with high shear production in a region with $0 < Ri_g < 0.25$ as shown by supporting figure 5.4.

Figure 5.3 (e) shows a patch of TKE in the wave breaking region at the left side of the crest ($-0.5 < \bar{x} < 0$) during flow reversal from down to upslope. The TKE and the isopycnal pattern are similar to those of case CEX04 shown in figure 8(c) of Jalali et al. (2014) who simulated tidal flow over a triangular obstacle. The dynamically relevant excursion number (Winters and Armi, 2013) for topography that has low Fr_h (such as the Luzon topography) is $Ex_i = U_0/(\omega l_i)$ where l_i is the inner length scale of the unblocked flow at the top of the main subridge. For the $Fr_h = O(1)$ obstacle of case CEX04, the relevant parameter is the regular excursion number, Ex. The value of $Ex_i = 0.55$ in the present simulation and $Ex = 0.42$ in case CEX04 of Jalali et al. (2014) are close, explaining the similarity in TKE pattern. The height of the turbulent patch is $3L_v$, where $L_v = U_0/N$ is the maximum vertical displacement of a fluid particle before all its kinetic energy is converted into potential energy. The implication is a turbulent patch with height of $3L_v \approx 360$ m at Luzon. This panel also shows strong turbulence in regions that are

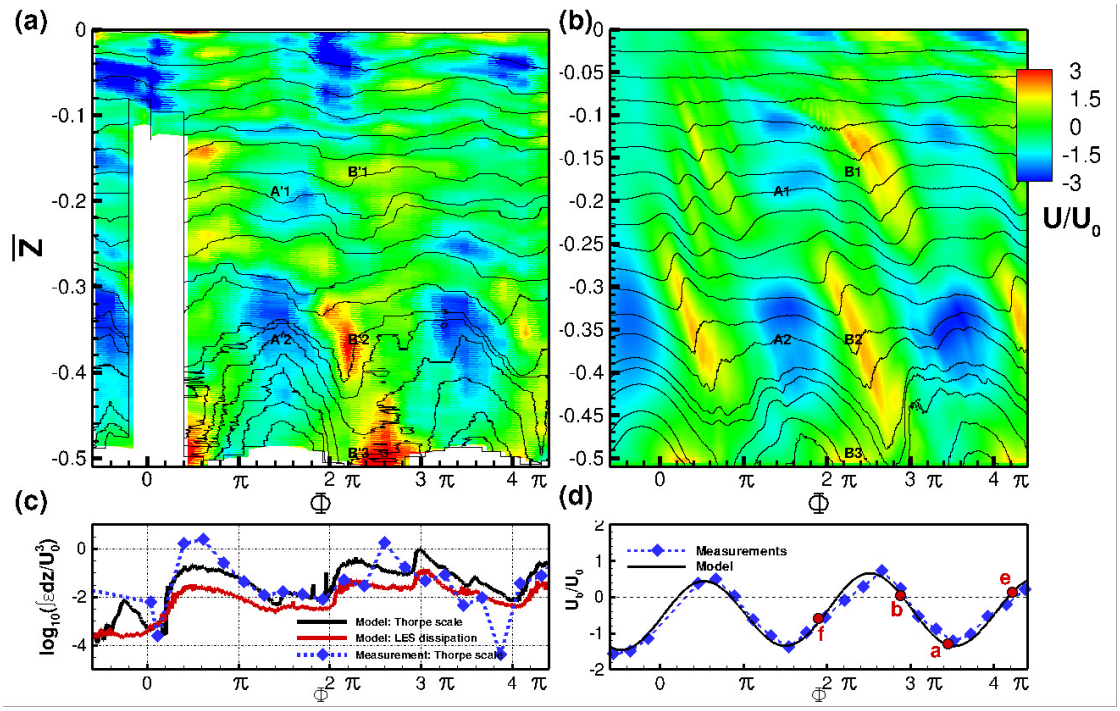

Figure 5.2: Time series of velocity and isopycnals at N2 station over a period of dominant semi-diurnal tide: (a) Observation of Alford et al. (2011), (b) Present simulation. (c) Temporal evolution of normalized depth-integrated dissipation compared among the directly computed LES model value (black), conventional Thorpe-scale method applied to model results and the Thorpe-inferred measurement (symbols), (d) Observed and model barotropic velocity at N2 station. Reference velocity, U_0, is chosen to be 0.132 m/s.

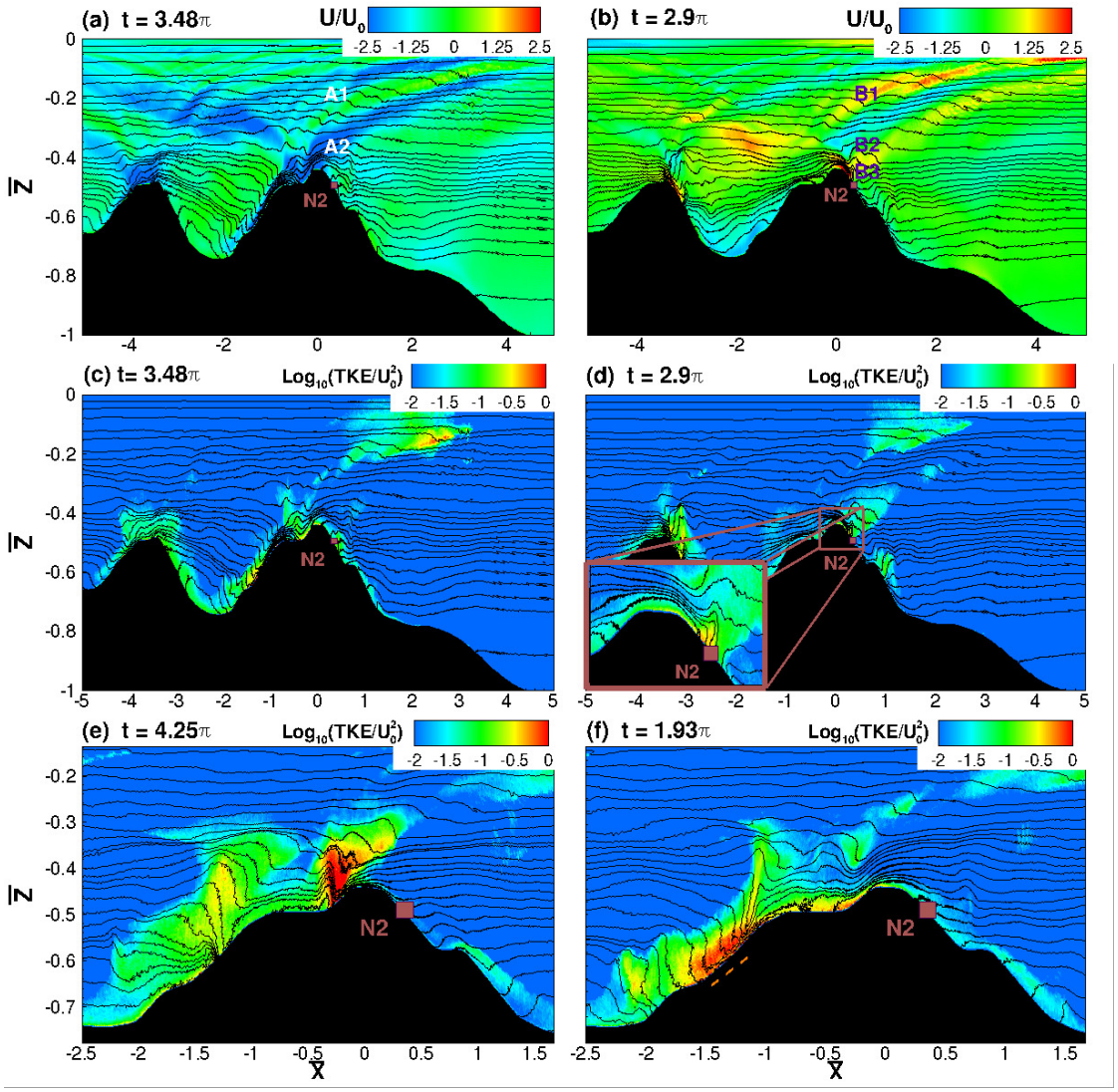

Figure 5.3: Snapshots of normalized zonal velocity and TKE with density isopycnals at different times (phases) of the tidal cycle. Labels in this figure and Figure 5.2 correspond to nonlinear features discussed in the text. The phases corresponding to (a)-(d) are marked.

elevated above the seafloor in the valley ($-1.5 < \bar{x} < -1.0$). In this particular region and phase, strong vertical velocities are generated that distort the isopycnals leading to regions of convective and shear instability with enhanced turbulence.

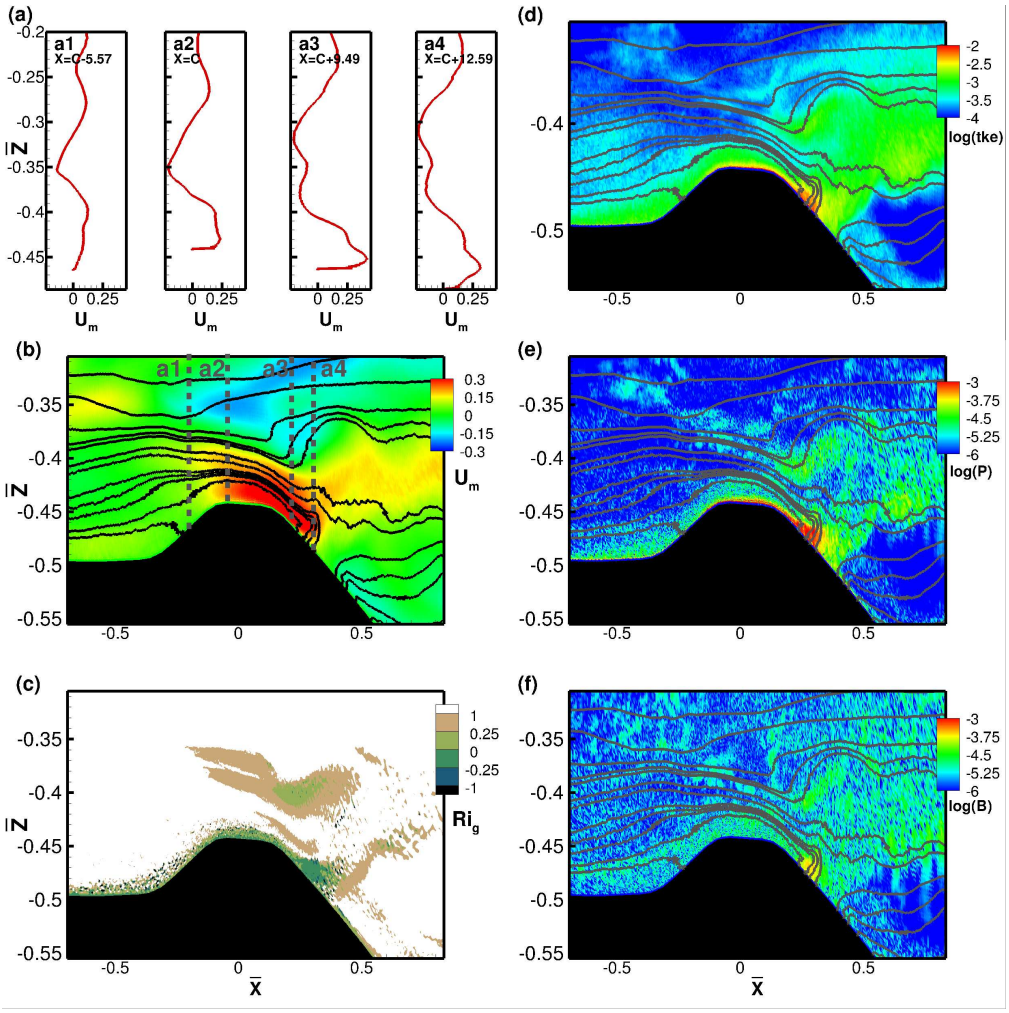

Figure 5.4: Top of the main subridge at tidal phase $\phi = 2.85\pi$: (a) Velocity profiles at four locations indicated in panel (b) by dashed lines. (b) Velocity contours and isopycnals. (c) Gradient Richardson number, Ri_g. (d) TKE. (e) Turbulent production. (f) Buoyancy flux.

Figure 5.3 (f) shows enhanced near-bottom turbulence at the critical and super-critical flank of the topography at $-1.25 < \bar{x} < -1.5$ during a phase when the local velocity is downslope and the tidal phase corresponds to westward (negative) velocity.

Here, the intensified velocity of about $3U_0$ leads to a turbulent patch of thickness $1.5L_v$ over the entire steep region. Lee-wave steepening with associated turbulence is also observed with the characteristic S-shape of isopycnals, associated with wave-breaking events, well above the topography in the circled region. The westward mean current in the forcing, although not dominant, contributes to the asymmetry of the baroclinic velocity and intensification of the baroclinic wave response at the steep section west (leeward with respect to the current) of each of the two subridges.

The spatial distribution of cycle-averaged flow and turbulence is shown in Figure 5.5 using mean kinetic energy (MKE), turbulent kinetic energy (TKE) and turbulent dissipation (ε). MKE is indicative of the asymmetric, complex and non-linear baroclinic response of multiscale steep bathymetry to a realistic asymmetric forcing including a current and oscillating tides. Midwater and above the valley ($-3.5 < \bar{x} < -1.5$ and $-0.5 < \bar{z} < -0.2$) there is an extensive patch of MKE due to interaction of beams from the subridges. However there is little TKE and ε in this region because the gradient Richardson number, $Ri_g = N^2/S^2$ with S the local shear, exceeds the critical value of 0.25. TKE and ε are enhanced at the top of the subridges and at their near-critical and super-critical flanks. The layer of turbulence has a vertical thickness of approximately $5L_v$ and ε that varies between $10^{-2} - 10^0 \times U_0^2 N$. Turbulence is also enhanced within the high-mode wave beams which have regions of $Ri_g < 0.25$ and extend eastward from their origin into the pycnocline. Panel (d) depicts criticality of the topography. Extended regions of subcritical topography have little turbulence as observed by (Haren et al., 2015).

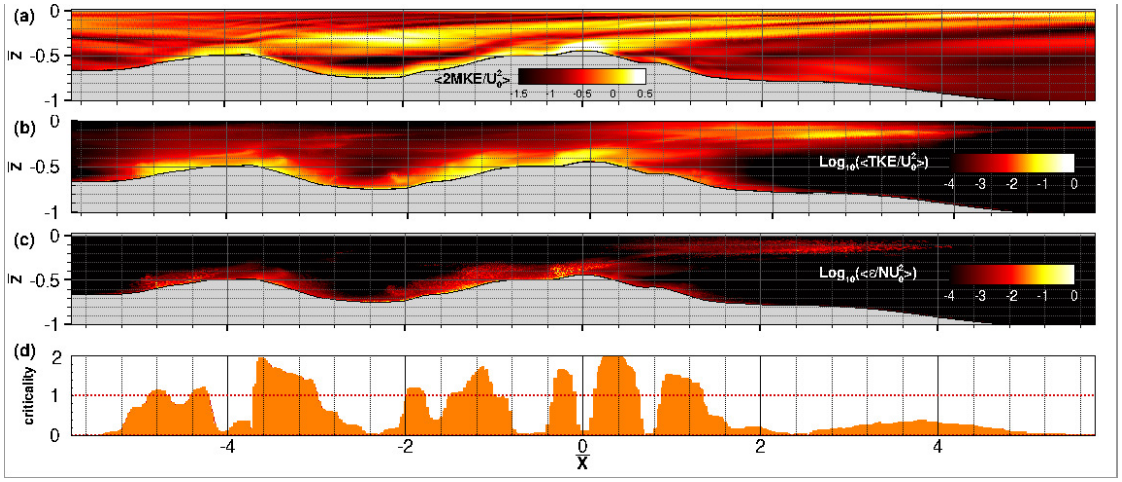

Figure 5.5: Flow and turbulence at a transect of the Luzon west ridge as the spatial distribution of time-averaged (a) mean kinetic energy, (b)turbulent kinetic energy, TKE and (c) turbulent dissipation, ε_t. All normalized and (b) and (c) are in logarithmic scale. Panel (d) shows the criticality to emphasize the enhanced turbulence near the top of the (super-)critical slopes.

5.3 Energetics of baroclinic response

The baroclinic energy (BC) equation (Equation (2.25) is used to quantify wave energetics as

$$C_l + C_{nl} = \frac{\partial}{\partial t}(E_p + E_k) + M + M_{adv} + \varepsilon_{bc} + P\,. \tag{5.1}$$

The net energy conversion ($C_l + C_{nl}$) has the following possible pathways: (a) Leave the generation site as an internal wave flux (M) plus an advective flux (M_{adv}) , (b) Dissipate locally by viscosity acting on gradients in the wave field (ε_{bc}) or by conversion to turbulence (P), and (c) Tendency or unsteadiness, $\frac{\partial}{\partial t}(E_p + E_k)$. Each term of Equation (5.1) is integrated over the computational domain excluding the sponge and averaged over two semidiurnal periods. The baroclinic response is not in steady state during the observational period and, therefore, $\partial E/\partial t$ is nonzero. The terms, normalized by the factor $(\pi/4)\rho_0 U_0^2 h^2 \sqrt{N_\infty^2 - \Omega^2}$ used in linear theory, are

$$C_l = 0.807, C_{nl} = 0.010, M = 0.550, M_{adv} = -0.028, P = 0.159, \varepsilon_{bc} = 0.031, \frac{\partial E}{\partial t} = 0.111\,.$$

The numerical model exhibits excellent energy balance with the residual (LHS - RHS) of Equation (5.1) being less than 1% of conversion. The conversion of $C_l = 0.807$ is consistent with previous values for supercritical obstacles, e.g. Pétrélis et al. (2006); Jalali et al. (2016) .

The local energy loss is of great interest. Buijsman et al. (2014) report 3D simulations that include a configuration with only the west ridge (column WR in their Table 2) which shows diagnosed dissipation ($C_l - M$) that translates to an energy loss of $q = 1 - M/C_l = 21.3\%$. The reported (resolved) dissipation is only about 3.8% ofC_l implying that most of their model dissipation is due to unresolved processes. Here, in contrast, the BC energy budget has negligible residual. The production term, P, is 19.7 % and baroclinic dissipation, ε_{bc}, is 3.8 % of C_l which makes the local energy loss, $q = (P + \varepsilon_{bc})/C_l = 23.5\%$. Thus, the local energy loss is mostly attributed to turbulence via resolved processes described in Section 5.3.

5.4 Conclusions

Three dimensional, high-resolution LES is performed for tidal flow over multi-scale steep topography patterned after a portion of Luzon strait, a wave generation site studied in IWISE. A 40 km transect with ocean depth between 1594 m and 3694 m is considered and the simulation is designed to match key nondimensional parameters, namely, the slope criticality, excursion number, Froude number, and aspect ratio. The simulated velocity with a strong baroclinic response and turbulent dissipation are demonstrated to

exhibit reasonable agreement with the corresponding observations at mooring N2. For example, internal wave beams lead to intensified velocity (features A1-A2 and B1-B2 in figure 5.2) that occur with similar magnitude and tidal phase as in the observations. An exception is a short duration of the tidal cycle during which resonant interaction with the waves from the east ridge (not included in the present model) is important for the baroclinic response at N2 as found by (Buijsman et al., 2012, 2014).

Previous work on near-topography tidally-driven turbulence has focused on individual mechanisms in isolation, e.g. wave breaking at the ridge top (Klymak et al., 2008; Legg and Klymak, 2008) and turbulence at near-critical ridge flanks (Gayen and Sarkar, 2011b). The present LES of a more complex topography shows turbulence from a variety of mechanisms such as downslope jets (contributing to 11% of TKE), high-mode internal wave beams (20% of TKE), off-slope breaking waves in regions considerably above the ridge top (6% of TKE) and over steep valley walls (16.5% of TKE). Uplsope bores following flow reversal and intensified boundary velocity at steep (critical and supercritical slopes) contribute about 22% and 13% of TKE, respectively. There is also 3.5% of TKE in weakly-stratified near-wall boundary layers and about 8% not attributed directly to any of these specific mechanisms. Note that the overlap of mechanisms leads to some variability in the numerical values given above. Furthermore, although both subridges of the west ridge have similar local steepness (local slope criticality between 1 and 2), the crossing of beams from opposite slopes, the presence of a valley between the subridges, as well as the sloshing asymmetric forcing leads to strong asymmetry in the ε pattern. Not only local generation of turbulence (by shear instability when locally $0 < Ri_g < 0.25$ and convective instability when locally $N^2 < 0$) but also advection and transport play a role in establishing the spatial pattern of TKE. The implication is that steep-bathymetry deep regions such as Luzon strait have 100-400 m tall turbulent

overturns.

Linear theory, e.g Pétrélis et al. (2006), shows that conversion to internal tides is enhanced at steep, supercritical obstacles. The present LES show that the local turbulence loss is also enhanced and, particularly so, in the present case where there are two nearby steep subridges and a steep-walled valley between them. The baroclinic energy budget is closed with negligible residual and the local loss is found to be $q = 23.5\%$ of conversion. Climate models need to parameterize turbulence and mixing driven by internal waves. The present LES shows that the bathymetry has an envelope of turbulence (thickness about $5U_0/N$ and $\varepsilon = 10^{-2} - 10^{0} \times U_0^2 N$) around supercritical and near-critical regions and also patches of turbulence further away in the upper ocean that are associated with instability of high-mode internal wave beams. At the simulated Luzon transect, the implication is a 600 m vertical envelope of tidal-averaged ε of $O(10^{-7} - 10^{-5})$ $\mathrm{m}^2/\mathrm{s}^3$. Nested models, e.g. Santilli and Scotti. (2015), and embedded LES can capture turbulent hot spots as they occur and can thus lead to further improvement in the understanding and numerical modeling of internal wave driven turbulence in the ocean.

Acknowledgements

This chapter, in full, has been submitted to the Journal of *Geophys. Res. Lett.*. The dissertation author is the primary investigator and author of this paper. I am grateful gratefully acknowledge the support of ONR grant N00014-09-1-0287 and NSF grant OCE-1459774.

Chapter 6

The accuracy of overturn-based estimates of turbulent dissipation

The complexity and cost of direct microstructure measurements of turbulent dissipation restricts such measurements to limited areas and for a limited period of time. In order to address the need for a broader spatial and temporal coverage of turbulent dissipation and mixing, easily available CTD data have been processed to infer dissipation from density profiles in several locations including hotspots of internal tide generation such as the Hawaiian ridge and the double-ridged system at Luzon Strait.

A simple objective method to infer dissipation rate is based on the vertical overturning length scale computed from measured density profiles. Thorpe (1977) originally proposed a density sorting method to estimate the vertical length scale of density overturns in a stably stratified fluid. This scale has since been called the Thorpe scale L_T. It is theorized that there is a linear relationship (at least statistically) between L_T and the Ozmidov length scale $L_O = \sqrt{\varepsilon/N^3}$. Knowledge of ε through L_O then leads to the eddy diffusivity through $K_\rho = \Gamma\varepsilon/N^2$ where Γ is the mixing efficiency. The Thorpe

scale, L_T, is a kinematic measure of the length scale of an overturn that is computed as the root-mean-square (rms) of parcel displacements that would be required to achieve a statically stable density profile in that overturn. The Ozmidov scale, L_O, is the size of the largest eddy unaffected by buoyancy in stratified turbulence, a length scale that can be constructed from ε and N by $L_O = \sqrt{\varepsilon/N^3}$ where ε is the rate of dissipation of turbulent kinetic energy and N is the buoyancy frequency (Ozmidov, 1965; Dougherty, 1961). L_O is determined by dynamics, i.e., it is the length scale of turbulent motion at which there is a balance between buoyancy force and inertial force.

There are observational studies (Ferron et al., 1998; Wesson and Gregg, 1994; Moum, 1996) suggesting that statistical measures of L_T and L_O are linearly related and in some cases may even be approximately equal, $L_T \approx L_O$ (Peters et al., 1988; Dillon, 1982). There are several studies concerning the relationship between L_T and L_O, for example, Dillon (1982) found that $L_O = (0.8 \pm 0.4)L_T$, Crawford (1986) found $L_O = (0.66 \pm 0.27)L_T$ and Ferron et al. (1998) proposed $L_O = (0.95 \pm 0.6)L_T$. Based on these results, the dissipation rate has been inferred from density measurements in areas where direct measurement with microstructure profiles is not possible. However, it is worth noting that the aforementioned observational studies pertain to shear-driven turbulence in the stratified upper ocean with relatively small $O(1-5)$ m overturns while topographic hot spots in regions like Luzon Strait often have $O(10-100)$ m overturns with the largest turbulent features resulting from convective instability, not shear instability.

The basis for a linear relationship between L_T, a kinematic measure of an overturn length scale based on sorting a density profile, and L_O, defined through a dynamic measure is not clear *a priori*, motivating investigations into when and why does the linear

relationship hold. Smyth et al. (2001) considered the nonlinear evolution of a KH billow in a stratified layer which is an example of turbulence that is primarily driven by *shear instability* and, using DNS, found that L_O/L_T in this problem continuously increased from a small value to an $O(1)$ value. Thus, the Thorpe estimate of dissipation with an $O(1)$ proportionality between L_T and L_O was inferred to be more applicable to "old" turbulence. Mater et al. (2013) analyzed DNS simulations of decaying homogeneous turbulence, finding agreement between L_T and L_O only for the special case when the buoyancy and turbulence time scales are equal. It was also found that L_T correlated well with length scales based on turbulent kinetic energy (K): the large-eddy length scale, $K^{3/2}/\varepsilon$, when buoyancy was weak and the buoyancy length scale, $K^{1/2}/N$, when buoyancy was strong.

Chalamalla and Sarkar (2015) considered turbulence driven primarily by *convective instability* of overturns in a stratified, oscillating, boundary flow, an idealization of near-bottom flow driven by a topography-affected internal wave. A smaller-scale problem (L_T as large as 2 m) was examined using DNS and a larger-scale problem (L_T as large as 20 m) was examined using high-resolution LES. The Ozmidov length scale and Thorpe length scale were found to behave differently during a tidal cycle: L_T decreased as the large convective overturn event (LCOE) evolved in time, while L_O increased; there was a significant phase lag between the maxima of L_T and L_O; and, finally, L_T was not linearly related to L_O. The ratio, L_T/L_O, could be larger or smaller by one-two orders of magnitude. Interestingly, the *cycle-averaged* values of L_T and L_O were found to have an $O(1)$ ratio in both DNS and LES, a result that was explained by the available potential energy in the LCOE being the predominant driver of turbulence in that flow. It is worth noting that Chalamalla and Sarkar (2015) employed a inversion based method to calculate L_T (section 6.1.2) and not the conventional Thorpe sorting method (section

6.1.1). Mater et al. (2015) compared L_T and L_O using data from three observational campaigns: Internal Waves In Straits Experiment (IWISE) conducted in Luzon strait where there are $O(100)$ m overturns associated with steep, supercritical topography, Brazil Basin Tracer Release Experiment (BBTRE) with $O(3)$ m overturns in a site with bottom-enhanced turbulence and the North Atlantic Tracer Release (NATRE) where turbulence is representative of less energetic, interior ocean turbulence. Instantaneous profiles of L_T were found to have bias with respect to those of L_O; the resultant bias in turbulent dissipation was mitigated by ensemble averaging but not by either depth- or time-integration. The bias was especially large and positive for a series of profiles taken at Luzon strait (large overturns with turbulence primarily driven by convective instability) resulting in an $O(10)$ over-estimate in the depth- and time-integrated dissipation. Scotti (2015) used DNS to evaluate the accuracy of overturn-based turbulent dissipation during the nonlinear evolution of a initially unstable patch in an otherwise stably stratified fluid as an idealized example of convectively-driven mixing and found that L_T is much larger than L_O. On the other hand, L_T was able to diagnose turbulent dissipation in stratified Couette flow between two walls in relative motion, an example of shear-driven turbulence.

Bias in overturn estimates of turbulent dissipation at rough topography has been investigated using observational data by Mater et al. (2015) but the simulation-based investigations have so far been restricted to canonical flows as described above that do not have topographically generated internal waves or rough boundaries. This motivates the present study of a northern section of the western ridge of Luzon strait with multiscale topography. Focusing on the western ridge allows high resolution of turbulent features but has the disadvantage of excluding the physical effect of wave resonance between the two ridges (Alford et al., 2011; Buijsman et al., 2012) at Luzon Strait.

Evidence in support of overturn-based methods, often used to infer turbulent dis-

sipation rate from density profiles, is typically taken from regions with weaker turbulence than that at rough-topography hotspots. The present work uses DNS of an idealized sloping topography problem (Chalamalla and Sarkar, 2015) as well as high-resolution large eddy simulation (LES) of turbulent flow at more realistic topography, a model discussed in Chapter 5, in order to investigate the accuracy of overturn-based methods in sites with internal wave breaking. Two methods are assessed: Thorpe sorting where the overturn length L_T is based on local distortion of measured density from the background, and the new proposal of inversion sorting where L_I measures the statically-unstable local region. The overturn boundaries are different between the two methods.

6.1 The computation of turbulent dissipation rate

The turbulent dissipation rate, ε, can be inferred from the overturn thickness and buoyancy frequency, N, by assuming that an overturn length scale defined by the Thorpe scale, L_T, is proportional to the Ozmidov length scale (Ozmidov, 1965). The procedure for calculating L_T involves resorting the instantaneous potential density profile at a particular observational station and time into a stable monotonic profile as well as identifying overturns. We continue below with a description of the conventional *Thorpe sorting* method and the proposed *inversion sorting* method.

6.1.1 Thorpe sorting method

The Thorpe sorting method appears in several previous studies, e.g. Galbraith and Kelly (1995); Klymak et al. (2008); Gargett and Garner (2008). The following procedure is based on the discussion in Klymak et al. (2008) and the associated algorithm is given in the Appendix, Algorithm 1. The density profile containing inversions is resorted into a stable monotonic density profile. Note that if the vertical grid is not constantly spaced,

an interpolation of the density profile to an evenly spaced grid is performed to conserve the average density of the profile in the resorting process. The Thorpe scale displacement is given by the difference in depth of each fluid parcel between the unsorted and sorted profiles,

$$d_\rho = Z(\rho) - Z(\rho_s)\,. \tag{6.1}$$

An auxiliary variable, S_ρ, is introduced. At each vertical point, S_ρ is the depth-sum of individual Thorpe displacements d_ρ from the upper bound of the density profile up to that point. The bounds of an overturn are determined by the locations where S_ρ drops back to zero (in practice, a threshold close to zero is adopted). The Thorpe length scale, L_T, associated with each so-identified overturn is calculated as the root-mean-square of displacements for the points within that overturn:

$$L_T = \sqrt{< d_\rho^2 >}\,. \tag{6.2}$$

Here, $< >$ stands for averaging over grid points inside the overturn. The dissipation rate, estimated from each individual overturn, is expressed in terms of the buoyancy frequency of the sorted density profile, N_{ov} and the Thorpe length scale, L_T. Note that N_{ov}^2 is computed using the density gradient averaged over the points in the overturn. Assuming the commonly used relation between Ozmidov and Thorpe scales, $L_O = 0.8 L_T$, the dissipation rate is given by:

$$\varepsilon_T = 0.64 L_T^2 N_{ov}^3\,. \tag{6.3}$$

6.1.2 Inversion sorting method

The inversion based method, proposed by us, takes the edges of each observed density inversion (or temperature inversion) as boundaries of an overturn and, by so doing,

implicitly assumes that it is the potential energy of each inversion that is instantaneously available for turbulent dissipation because the profile is statically unstable. The algorithm to estimate dissipation by this method is shown in the Appendix, Algorithm 2. Because of the difference in marking overturn boundaries, this inversion-based method leads to smaller overturns relative to the original Thorpe method as will be shown later. Another difference is that the computation of the particle displacement required to attain a stable profile is based on the reordering of the density profile within the inversion rather than reordering the "complete" density profile that is done in the Thorpe sorting method. The *inversion length scale*, L_I, is then computed using $L_I = \sqrt{< d_\rho^2 >}$ where the average for root-mean square displacements is over the identified inversion. The factor 0.64 in Eq. (6.3) is based on calibration of the Thorpe sorting method against observational data sets. Without any justification for using that factor in the inversion sorting method, we elect to use unity as the coefficient, i.e., the turbulent dissipation rate associated with a so-identified overturn is

$$\varepsilon_I = L_I^2 {N_{ov}}^3 , \tag{6.4}$$

where N_{ov}^2 is computed as the averaged density gradient within the overturn, exactly as in the original Thorpe method. We filter out small overturns from inversions that span less than or equal to three grid points since they are marginally resolved. In application of this method to an oceanic dataset, a similar thresholding based on noise in the data will need to be adopted.

6.1.3 An example computation of the Thorpe scale

Figure 6.1 shows the overturn bounds which were employed for the dissipation calculation at a particular time $t = 239.93$ [year-day] at N2 station using measure-

ments (Alford et al., 2011) at Luzon strait which were kindly shared by the authors. Panel (a) shows the unsorted and sorted profiles in the Thorpe sorting method, panel (b) shows the Thorpe displacement and the summation of displacements, S_ρ. The region between successive zero values of S_ρ is identified as the vertical extent of an overturn (as indicated by double arrow line for each overturn) in the Thorpe sorting method. Panels (c) and (d) of figure 6.1 show overturn bounds using the inversion and Thorpe sorting approaches, respectively, in a 250 m vertical section. The Thorpe sorting approach in panel (d) detects a big overturn between depths of approximately 1500 and 1740 m (in agreement with Alford et al. (2011)) while the inversion sorting approach in panel (c) detects multiple smaller overturns within the same region.

6.1.4 Model dissipation from LES

The dynamic Smagorinsky model, used in this simulation, is a well established subgrid model for LES which has been applied successfully in several previous studies, for example, in a rotating channel flow (Piomelli, 1995), mixing layers (Vreman et al., 1997a), scalar mixing in axisymmetric jets (Akselvoll and Moin, 1996), turbulent boundary layer over a bump (Wu and Squires, 1998) and flow over bluff bodies (Rodi et al., 1997). The accuracy of turbulent dissipation rate obtained from the subgrid model has been validated in several studies, for example, by Martin et al. (2000) who found close agreement between the dynamic Smagorinsky model and DNS in the case of isotropic turbulence, and by Foysi and Sarkar (2010) in a compressible mixing layer. Recently, Pham and Sarkar (2014) compared DNS and LES results in a stratified shear layer and found good agreement between them with regards to the buoyancy-induced reduction in shear layer growth rate and the TKE balance. The LES modeling of flow near complex geometry such as the Luzon Strait is a first attempt to study mixing and dissipation mechanisms at relatively high Reynolds number. Therefore, particular attention is paid to ensure

adequate numerical accuracy in the calculation of the model turbulent dissipation.

Resolved dissipation is defined as,

$$\varepsilon_{resolved} \equiv \nu \left\langle \frac{\partial u_i'}{\partial x_j} \frac{\partial u_i'}{\partial x_j} \right\rangle_y , \tag{6.5}$$

where u_i' stands for velocity fluctuations with respect to the spanwise averaged mean velocity and the subgrid scale dissipation, ε_{sgs}, is given as

$$\varepsilon_{sgs} = -\left\langle \tau_{ij} S_{ij} \right\rangle_y , \tag{6.6}$$

where τ_{ij} is the subgrid scale stress tensor and S_{ij} is the strain rate of the LES field.

The setup has a stretched grid in the vertical direction in addition to conforming with the bottom boundary. This allows enhanced resolution of the boundary layer and processes near the ridge top. In the vicinity of the ridge top, the grid spacing is $\Delta x = 0.089$ m and $\Delta z = 0.0475$ m. The spanwise direction has a uniform grid size of $\Delta y = 0.375$ m and spanwise derivatives are computed using a spectral method. The resolution in the boundary layer is adequate, e.g., at the no-slip boundary, case B has $\Delta x^+ = 3.83$, $\Delta y^+ = 15.97$ and $\Delta z^+ = 2.02$ in units of the viscous scale, ν/u_*, with u_* denoting the average friction velocity calculated using simulation results. Figure 6.2 (a)-(b) shows the spanwise spectra of the TKE at two locations S2 and S3. The spectra are calculated at the phase of flow reversal from down to upslope, where the turbulence due to wave breaking is at its peak. The three orders of magnitude drop in the wave number spectra shows that the model is able to capture almost all the turbulent kinetic energy which is indicative of LES with sufficient resolution(Pope, 2011). However, to make sure the stretched grid does not lead to an underestimation of turbulent dissipation we have added a positive

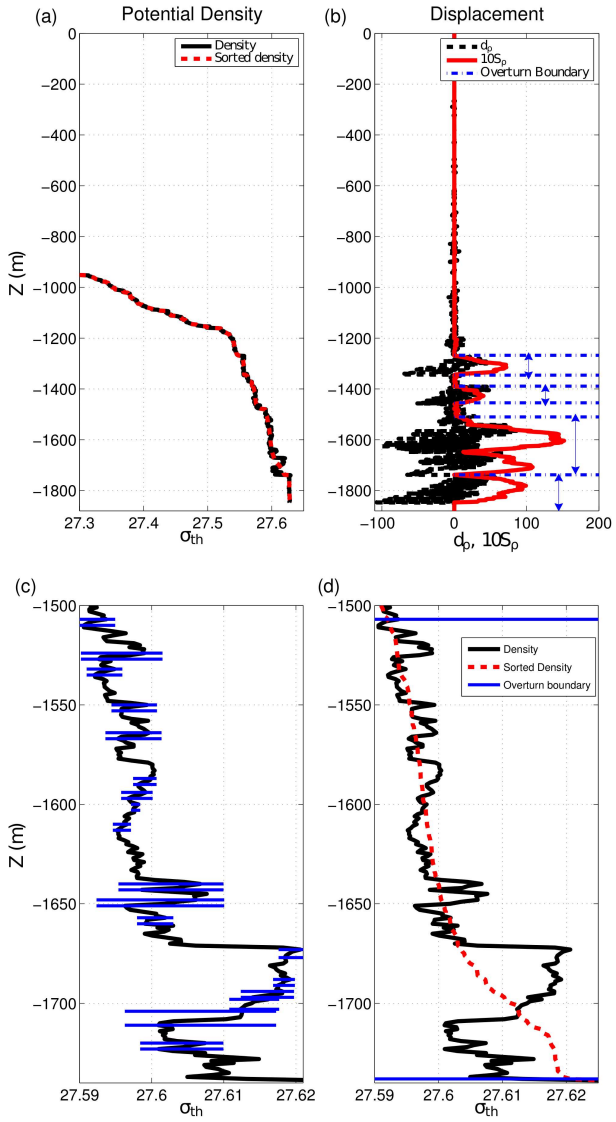

Figure 6.1: Example of Thorpe scale calculation by the different overturn sorting methods using the potential density profile measured at the N2 station of the IWISE experiment (Alford et al., 2011) at $t = 239.93[year - day]$. (a) Unsorted (black solid) and sorted (red dashed) potential density profile used by the Thorpe sorting method. (b) Local vertical displacement, d_ρ, in dashed black and summation of displacements, S_ρ, in red. Overturn boundaries identified by the Thorpe sorting method are shown with blue dash-dot lines and the vertical extent of each identified overturn is indicated by a blue double-arrowed line. (c) Zoom of unsorted density profile (black) showing overturn boundaries identified by the new *inversion sorting* method that is based on local density inversions. Several overturns are identified. d) Same zoom of unsorted density (black) as in part (c). The red dashed line is a zoom of the sorted density profile that was shown in part (a). The Thorpe sorting method identifies a large 250 m "overturn" instead of the smaller overturns identified by the inversion sorting method.

residual component when computing the model dissipation:

$$\varepsilon = \varepsilon_{resolved} + \varepsilon_{sgs} + \varepsilon_{residual} \tag{6.7}$$

The residual term is based on the numerical balance of the TKE equation,

$$\frac{\partial K}{\partial t} = P - \varepsilon_t + B - \nabla \cdot T\,. \tag{6.8}$$

Here K is TKE defined by $\frac{1}{2}\langle u_i' u_i' \rangle$. P is the production term defined as

$$P \equiv -\langle u_i' u_j' \rangle \left\langle S_{ij} \right\rangle - \langle \tau_{ij} \rangle \langle \overline{S}_{ij} \rangle,$$

where the last term is the SGS production. The turbulent dissipation rate, ε_t, is defined as the sum of the resolved and SGS components and B is the buoyancy flux defined as

$$B \equiv -\frac{g}{\rho_0} \langle \rho' w' \rangle.$$

The term $\nabla \cdot T$ denotes the transport of the turbulent kinetic energy, and contains pressure transport, turbulent transport, viscous transport, and subgrid scale (SGS) transport.

The Ozmidov length scale at the same locations and phase described above are also shown in figure 6.2 (c)-(d). At location S2 shown in panel (c), the average of L_O spanning between the bottom surface and $z = -16m$ is about $0.326m$ which is equivalent to approximately $8\Delta z$, suggesting that the Ozmidov scale is well resolved. Panel (c) also has a sub panel zoomed in near an energetic turbulence patch at $z = -17m$. The boundaries of the patch are marked by dashed lines, and the patch has a vertical extent equivalent to 13 grid points. At location S3 shown in panel (d), the average L_O spanning the region between the bottom boundary and $z = -15m$ is $0.286m$, which is approxi-

mately $8\Delta z$ based on the grid spacing in the local region. The good resolution of the Ozmidov scale by the grid is another indicator of adequate LES resolution. The CFL number of 0.57 constrains the time step Δt to a small value of approximately 0.04 s, resulting in approximately 11,000 time steps in a wave period. The model LES dissipation rate is compared with the overturn based dissipation rates at the modeled Luzon Strait.

6.2 Idealized simulation of internal tide breaking

In this section, results from a previous numerical study by Chalamalla and Sarkar (2015) will be revisited to compare dissipation rates inferred from overturn-based methods against the dissipation rates calculated from the simulation data. They performed DNS of an oscillatory bottom layer on a slope underneath an internal tide to quantify turbulence and mixing brought about by density overturns during the flow reversal from down to upslope. Convective instability is found to be the primary mechanism of transition to turbulence, where the large density overturn formed during the transition from down to upslope flow breaks down into small scale turbulence at a later time. The dominant fraction of the turbulent dissipation in this flow is associated with convectively-driven turbulence ensuing from the large convective overturning event (LCOE) and a smaller fraction is due to boundary layer dissipation during upslope flow. Thus, it is an idealized scenario to study the accuracy of various overturn-based dissipation rates during turbulence driven by wave breaking and density overturns. They, *without explicitly stating it*, adopted the inversion sorting method instead of the conventional Thorpe sorting method in their "Thorpe scale" analysis (more details about this study can be found in Chalamalla and Sarkar (2015)).

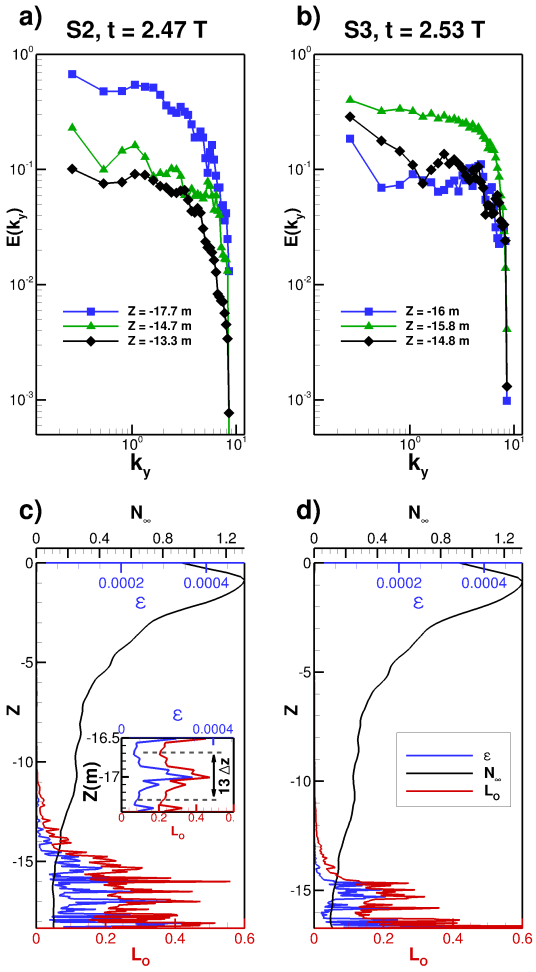

Figure 6.2: *Top row:* Two examples of spanwise wave-number (k_y) spectra of the turbulent kinetic energy. Spectra at 3 different heights are shown for each example. *Bottom row:* Turbulent dissipation rate, background buoyancy frequency, and Ozmidov length scale plotted in SI units. Parts (a) and (c) correspond to S2 location at $t = 2.47T$; parts (b) and (d) correspond to S3 location at $t = 2.53T$. The location of stations S2 and S3 on the ridge are shown in figure 6.4 (h)

Figure 6.3 (a) shows the the temporal evolution of Richardson Number profiles at the mid-slope of the DNS simulation for one cycle. Richardson Number, $Ri_g = N^2/S^2$, can be used as an indicator of possible instability. Here, S is the mean (span-averaged) shear and N is the mean (span-averaged) buoyancy frequency. We plot values of negative Ri_g that correspond to statically unstable regions. In figure 6.3 (a), the interval between $\phi = -0.3\pi$ and $\phi = 0.2\pi$, which has spatially coherent and highly negative Ri_g, corresponds to a LCOE.

Figure 6.3(b) shows the time evolution of spatially averaged dissipation calculated from both Thorpe scale and inversion based methods. The spatial average at any given time is computed by averaging the results of overturn-based analysis at that time, conducted for all vertical lines in the computational domain. We focus on the LCOE. Initially, when the overturn is still young and growing, both Thorpe scale dissipation, ε_T, and inversion scale dissipation, ε_I, increase. The turbulent dissipation, ε, from the simulation also exhibits an increase that commences at a phase of -0.1π and it peaks at the phase of 0.15π during the LCOE. However, the increase of ε_T is excessive during the overturn growth. The dissipation rate estimated from the Thorpe scale becomes higher by *between one and two orders of magnitude* when compared to either the model dissipation rate calculated from the simulation data or that obtained using the inversion method. Although there is a clear phase lag of the dissipation calculated from the simulation data with respect to the dissipation based on the inversion scale, the peak value of these dissipation rates are in good agreement.

The time-averaged dissipation rate over different periods of the cycle is of equal interest. During the life-cycle of the LCOE, the dissipation rate from the Thorpe sorting method leads to a substantial overprediction, $\Sigma\varepsilon_T/\Sigma\varepsilon = 14.6$, while the time-averaged dis-

sipation based on the inversion sorting method leads to a better estimate of $\Sigma\varepsilon_I/\Sigma\varepsilon = 0.6$. On the other hand, outside of the LCOE, the Thorpe sorting method is substantially more accurate. The time average over the non-LCOE part of the cycle is $\Sigma\varepsilon_T/\Sigma\varepsilon = 0.42$, while in the same period $\Sigma\varepsilon_I/\Sigma\varepsilon = 0.014$. It highlights the fact that Inversion sorting method underestimates the dissipation when the source of turbulence is not convective instability. Looking at the time-averaged dissipation rate during the entire cycle, the ratios of $\Sigma\varepsilon_T/\Sigma\varepsilon = 5.39$ for Thorpe sorting method and $\Sigma\varepsilon_I/\Sigma\varepsilon = 0.21$ for Inversion sorting indicate deficiencies of each method within and outside of LCOE, respectively. Ideally, Inversion sorting should be used for LCOE and, otherwise, Thorpe sorting.

Sensitivity of the two methods to the resolution of the grid which samples the density is also investigated using the DNS data. Four different sampling grids are used to calculate overturn-based estimation from the single dataset coming from the DNS of Chalamalla and Sarkar (2015). The same algorithm and threshold are used for all the sampling grids. The vertical grid resolution of the sampling grids is 1.5, 2, 2.5 and 4 time larger than that of the original DNS grid. The results which are presented in Table 6.1 show that the Thorpe sorting method is less sensitive to the size of the sampling grid, both inside and outside of the LCOE. The variation of the Thorpe sorting method as a function of sampling grid resolution is found to between 10%-20%. Meanwhile, the Inversion sorting estimate is more influenced by the resolution of the sampling grid. The dissipation tends to increase with the grid spacing in the Inversion method because the overturn size increases. Inversion sorting method is more dependent on the local behavior of the density while the Thorpe sorting method is dependent on the entire density profile since overturn boundaries are marked using the summation of displacement for the entire column.

Table 6.1: Sensitivity of overturn estimates of turbulent dissipation to the resolution at which the density profile is sampled. Ratio of time-averaged values of Thorpe-estimated dissipation and the turbulent dissipation ($\Sigma\varepsilon_T/\Sigma\varepsilon$), and a similar ratio for the Inversion-estimated dissipation ($\Sigma\varepsilon_I/\Sigma\varepsilon$). Time averages are computed during LCOE, outside LCOE and over the span of the entire cycle.

Size of	$\Sigma\varepsilon_T/\Sigma\varepsilon$			$\Sigma\varepsilon_I/\Sigma\varepsilon$		
Sampling Grid	Cycle	LCOE	Non-LCOE	Cycle	LCOE	Non-LCOE
dz_0 (DNS Grid)	5.39	14.6	0.42	0.21	0.6	0.014
$dz_1 = 1.5\,dz_0$	4.38	11.89	0.33	0.26	0.73	0.014
$dz_2 = 2.0\,dz_0$	5.10	13.84	0.40	0.36	1.03	0.020
$dz_3 = 2.5\,dz_0$	5.03	13.71	0.39	0.41	1.18	0.022
$dz_4 = 4.0\,dz_0$	4.96	13.40	0.40	0.57	1.66	0.031

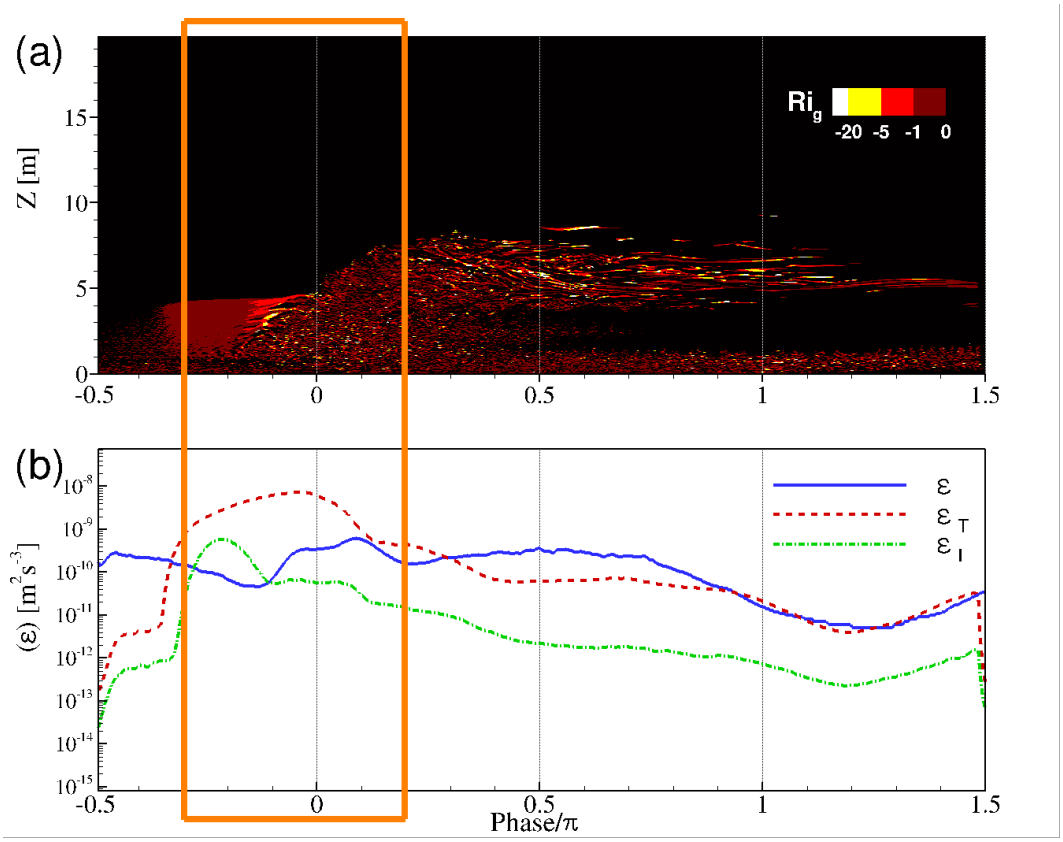

Figure 6.3: (a) Temporal evolution of the vertical profile of Ri_g. Negative values are shown to highlight statically unstable regions. (b) Spatially averaged dissipation during a tidal cycle in the DNS of Chalamalla and Sarkar (2015).The orange box marks a LCOE between $\phi = -0.3\pi$ and $\phi = 0.2\pi$, when convective instability outweighs other sources of turbulence.

6.3 A broader assessment of turbulent dissipation rate

In the present section, we broaden the scope of our assessment of overturn-based estimates of turbulent dissipation rate to investigate regions with dominant convective instabilities in a more realistic setup. Both Thorpe sorting as well as inversion sorting estimates are compared with the model dissipation rate obtained from simulation results. The comparison is performed at several locations in the vicinity of the ridge top for cases A and B. The time evolution of the vertically-integrated values of turbulent dissipation is compared between the two overturn-based methods and the LES model. Four different spatial locations with large wave-breaking features are chosen for the comparison in this case study as shown in Figure 6.4 (h): S1 is at the right flank approximately corresponding to measurement station of N2, S3 is at the top of the ridge, S2 is midway between S1 and top of the ridge, S4 is on the left flank.

The time evolution of depth-integrated dissipation is presented in figure 6.4. Model dissipation (ε) is compared with both the Thorpe sorting method (ε_T) applied to the simulation results, and inversion sorting method (ε_I) also applied to the simulation results. The evolution of turbulent dissipation is shown over three tidal cycles with the first tidal cycle corresponding to a ramp-up from the state of no turbulence. As elaborated below, at these four locations, the original Thorpe method significantly overestimates the turbulent dissipation in terms of magnitude and temporal duration. The *inversion sorting* method shows *better* agreement with the turbulent dissipation rate directly computed from the simulation. For example, the inversion sorting method (blue curve in figure 6.4(a)) quantitatively matches the turbulent dissipation rate computed from the model (black curve) at location S2 while the Thorpe sorting method (red curve) generally overestimates it, often by an order of magnitude.

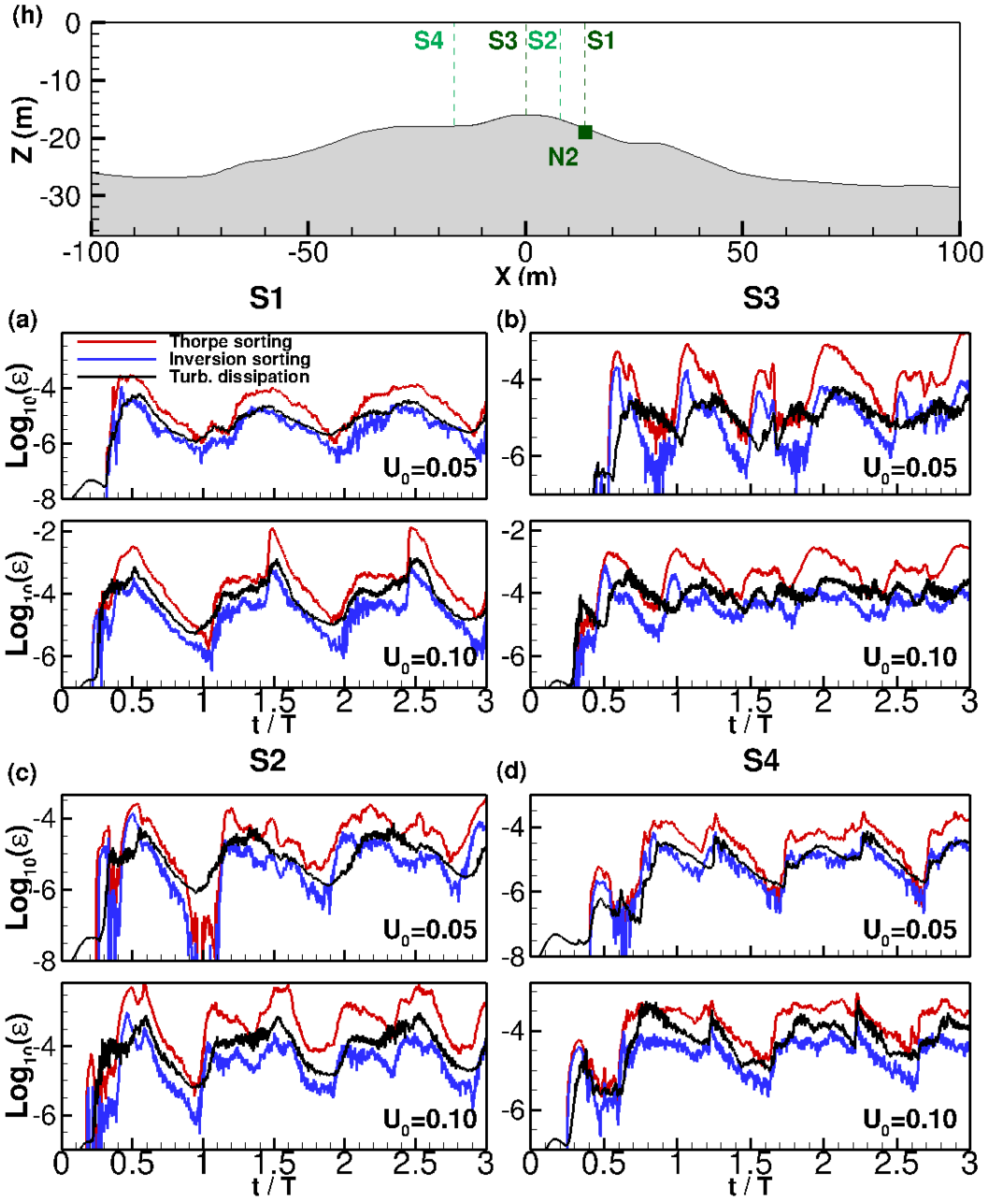

Figure 6.4: Temporal evolution of depth-integrated turbulent dissipation (black) compared with both the Thorpe sorting estimate (red) and the inversion sorting estimate (blue) for case A with a forcing of $U_0 = 0.05$ m/s (top subpanels) and case B with a forcing of $U_0 = 0.1$ m/s (bottom subpanels) at the following four locations: (a) S1, (b) S3, (c) S2 and (d) S4. The header, (h), shows the different locations of the virtual moorings.

The depth-integrated turbulent dissipation near the summit (station S3) is shown in figure 6.4(b). It is noteworthy that, similar to DNS results of Jalali et al. (2014), there are two dissipation maxima per cycle corresponding to the passage of turbulence from each of the two internal wave beams generated at the ridge flanks, while there is only one maximum at the left or right midslope locations. Similar to the situation at the S1 virtual mooring, the conventional Thorpe sorting method overestimates the dissipation at S2, S3 and S4.

Thus, our results show that Thorpe sorting estimate of dissipation at S1-S4, which are locations with breaking internal waves, lead to significantly larger turbulent dissipation rate relative to the value in the simulation. Comparison between overturn-based estimates and direct measurements of dissipation at sites with direct wave breaking are scant. However, Nash and Moum (2013) present a comparison of dissipation rate from microstructure measurement using Chipods with the Thorpe sorting estimate at the N2 mooring in the IWISE-2011 experiment. Their results suggest that the Thorpe sorting estimate is an overprediction relative to the direct measurement, consistent with the finding in our simulations.

An overall view of the accuracy of Thorpe sorting estimates in locations with large convective overturns is provided by comparing their cycle average with the cycle-averaged dissipation, $\Sigma\varepsilon$, in the model. Table 6.2 shows that the Thorpe sorting method leads to a substantial overestimate at those locations. The over-estimate can be by as much as a factor of 10. This shows that the inversion sorting method is a better predictor near the ridge top, where internal wave breaking leads to turbulence, albeit with occasional underestimation during some portions of the tidal cycle.

Table 6.2: Ratio of cycle-averaged Thorpe estimate to cycle-averaged turbulent dissipation ($\Sigma\varepsilon_T/\Sigma\varepsilon$) and a similar ratio of cycle-averaged values for the inversion sorting method ($\Sigma\varepsilon_I/\Sigma\varepsilon$). The cycle average is computed over the span of the second and third cycles.

Location	(Thorpe) (Thorpe)	Case B (Thorpe) (Thorpe)	Case A (Inversion) (Inversion)	Case B (Inversion) (Inversion)
S2	8.76	15.28	0.85	0.63
S3	11.14	12.38	1.55	0.66
S4	16.69	16.64	1.76	0.89
S5	8.45	6.16	1.05	0.57

6.4 Discussion

Based on the results discussed in the previous sections, it can be inferred that the inversion sorting method estimates the dissipation rate more accurately at locations where direct wave breaking is a major contributor to turbulence. In the present section, we seek a more complete understanding of the inversion sorting method and the flow conditions under which it is more accurate compared to the Thorpe sorting approach.

The fundamental difference between shear driven turbulence and convective driven turbulence is that, in shear driven turbulence there is a direct transfer from mean kinetic energy to turbulent kinetic energy through shear production. However, in convectively driven turbulence (wave breaking event in this study), mean kinetic energy drives the flow to a statically unstable density configuration, leading to an increase in the available potential energy, which is subsequently released to turbulence when the density overturn breaks down into small scale turbulence. The conventional Thorpe scale method estimates the total available potential energy in a density profile. However, the

recent study by Scotti (2015) argues that only a fraction of the total APE is available for turbulent dissipation during convective driven mixing.

Thus, a more accurate method of estimating turbulent dissipation rate during convective driven turbulence is necessary. The fundamental criterion on which the inversion sorting method has been developed is that, it is only the available potential energy within a density inversion that can be immediately released to cascade down to turbulence. The density inversion is the region where the density is *statically unstable* i.e $d\rho/dz > 0$ or $N^2 < 0$ and, therefore, the APE of that overturn is instantaneously available to energize turbulence through flow instabilities. In the inversion method, the density profile is sorted only within an inversion and the inversion length scale L_I is defined as the r.m.s of displacements of all fluid parcels within the inversion. ${L_I}^2 N^2$ is thus a measure of the *instantaneously available potential energy* (IAPE) associated with the inversion. Assuming that a substantial fraction of this energy goes into turbulent dissipation over a time scale of the order $1/N$, the turbulent dissipation rate can be estimated as $\varepsilon_I \propto {L_I}^2 N^3$, which is expected to be more accurate in situations where density inversion is a dominant source of turbulence. This is consistent with the results discussed in the previous section, where the inversion sorting method is able to better estimate the dissipation rate of turbulence that originates from density inversions. On the other hand, the conventional Thorpe sorting approach considers zero sum of Thorpe displacement as the bounds of an overturn and then computes the Thorpe length scale (by r.m.s of the previously calculated Thorpe displacements). N^2 is not less than zero throughout the overturn identified by the Thorpe sorting method and, therefore, the APE of the entire Thorpe overturn is not instantaneously available for breakdown to turbulence through instability. The Thorpe length scale is found to be almost 3-8 times larger compared to the inversion length scale at locations of large density inversions, and thus the dissipation rate from the Thorpe sorting method which is proportional to the square of the length scale ($\varepsilon_T \propto {L_T}^2 N^3$) is

expected to be an order of magnitude larger when compared to ε_I.

To better explain the differences between the two overturn-based estimates, Figure 6.5 contrasts convectively driven turbulence with shear driven turbulence. Panel (a) shows the density profile that is typically found during turbulence driven by convective overturns, taken from the idealized problem examined by Chalamalla and Sarkar (2015). The black line shows the unsorted density profile, while the red dashed line shows the sorted density profile obtained using the Thorpe sorting method. The overturn boundaries from the Thorpe sorting method are represented by red dash-dotted lines, whereas blue dash-dotted lines represent overturn boundaries using the inversion sorting method. It is evident that the overestimation of dissipation using the Thorpe sorting method is due to the larger overturn height, which results in large Thorpe scale. Panel (b) of this figure will be discussed shortly.

There is an important *caveat* to the inversion sorting estimate. Since this method measures APE within regions where the density profile is actually unstable, it may not be accurate when turbulence is due to shear that has sufficiently small gradient Richardson number for instability or due to advection/transport from elsewhere. In other words there may be turbulence in locations where the density profile does not necessarily contain an overturned region that spans the entire patch of turbulence.

Returning to the schematic contrasting convective and shear-driven turbulence, Figure 6.5(b) shows density profile from a simulation, which has similar parameters to Armenio and Sarkar (2002), where stratified channel flow was studied. In that case, turbulence was mainly driven by shear production near the wall that was then distributed across the channel by turbulent transport. The region with density inversion can be seen

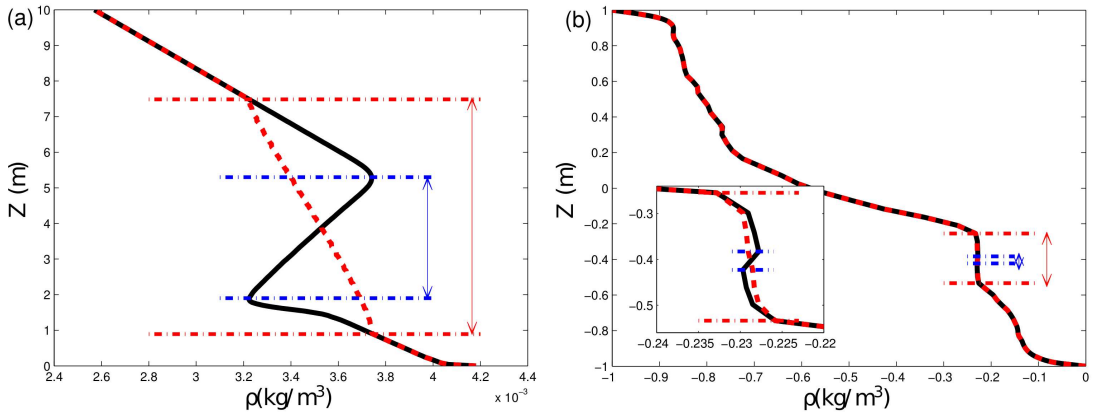

Figure 6.5: Schematic of overturn-based estimation for two different scenarios of turbulence generation: (a) Convective instability drives turbulence. From results of the LES case of Chalamalla and Sarkar (2015), and (b) Shear drives turbulence. From a repeated simulation of stratified channel flow considered by Armenio and Sarkar (2002). In each part of the figure, the instantaneous density profile (solid black) is shown with the overturn boundaries (blue dash-dot horizontal line) identified by the inversion-based method. The Thorpe-sorted (dashed red) profile employed in the conventional method and the corresponding overturn boundaries (red dash-dot horizontal line) are also shown.

to be much smaller than the region with mean shear and turbulence. Therefore, the inversion sorting method, which measures the available potential energy owing to the small inversion (between blue dashed lines) is unable to estimate turbulent dissipation correctly. The two scenarios that we have described here are idealized limits of realistic ocean mixing since ocean turbulence in general involves both shear and convectively driven instabilities. Nevertheless, the idealized scenarios in figure 6.5 allows us to understand the limitations of the alternative overturn-based methods.

Meanwhile, the Thorpe sorting method has better agreement in situations where shear instability is responsible for turbulence (Dillon, 1982; Crawford, 1986; Ferron et al., 1998). In such cases, the dissipation scales as $u^3/L \propto (SL)^3/L = S^3L^2$ where S is the mean velocity shear of the overturn. Furthermore, since the Thorpe sorting overturn measured from the density profile is essentially caused by shear, L can be taken to be proportional to L_T. Meanwhile, S is proportional to N in the overturn since the Richard-

son number, N^2/S^2, required to get shear instability is $O(1)$. Therefore, it is reasonable to assume $\varepsilon \propto L_T^2 N^3$ for shear driven turbulence. The coefficient has been calibrated in various studies (Dillon, 1982; Crawford, 1986; Ferron et al., 1998). Shear-driven turbulence does not necessarily need to have a large inversion region for large TKE (an extreme example is shear driven turbulence in a non-stratified system).

To quantify the relative behavior of Thorpe length scale and Ozmidov length scale in regions with large internal wave breaking, the time evolution of average Thorpe scale and Ozmidov scale are shown in the Figure 6.6 for case B at S1. Panel (a) depicts that at phases with large overturns (for example $t/T = 1.5$ for S1), L_T is significantly larger than L_O. Panel (b), displaying the ratio of L_T/L_O, shows that the widely used assumption of $L_T/L_O = 1/0.8 = 1.25$ is incorrect. L_T/L_O has a large variation, from 1 to a peak of 8 during the cycle.

6.5 Conclusions

Three-dimensional, high-resolution large eddy simulations are performed for tidal flow over a multi-scale topography patterned after a cross-section of Luzon Strait, a double-ridge generation site which was the subject of the recent IWISE experiment. A 1:100 scaling of topography was employed and environmental parameters were chosen to match field values of important nondimensional parameters: the slope criticality, excursion number and Froude number. Using the observational data for the local barotropic velocity at station N2 for model forcing in case M, the simulated velocity (dominated by the baroclinic response) and turbulent dissipation are demonstrated to exhibit good agreement with the corresponding field observations. An exception is a short duration of

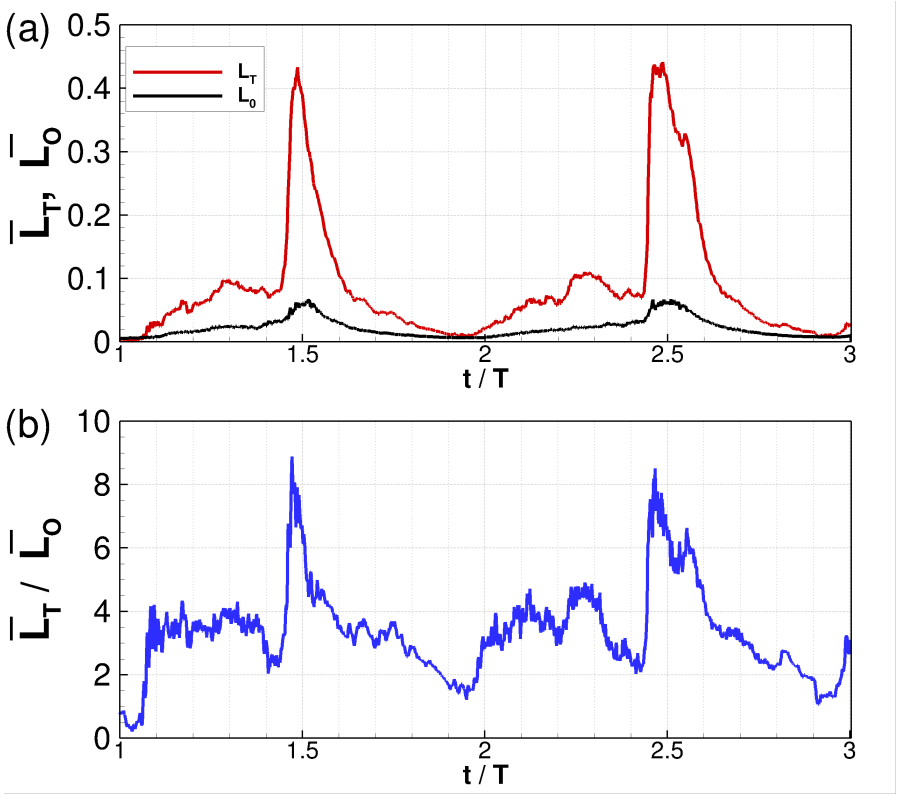

Figure 6.6: (a) Temporal evolution of averaged Thorpe scale, $\bar{L}_T$, (in red) and Ozmidov scale, $\bar{L}_O$, (in black) for Case B at Location S1 during second and third cycles. (b) The corresponding ratio of $\bar{L}_T/\bar{L}_O$.

the tidal cycle when the resonant interaction with the east ridge (a topographic feature that is not included in the present computational model so as to optimally resolve turbulence at N2 with available computational resources) is important for the baroclinic response at N2.

The focus of the paper is an assessment of overturn-based estimates of turbulent dissipation at rough topography that generates internal gravity waves. The conventionally used Thorpe sorting estimate leads to over prediction of turbulent dissipation relative to the model value at station N2. To broaden the assessment, two different cases A and B with low and moderate tidal velocities, respectively, are simulated and several locations on the model ridge transect are considered. A new inversion sorting method is proposed and its performance is compared with the widely used Thorpe sorting method. The Thorpe sorting method can qualitatively estimate dissipation in terms of spatial distribution and phasing but is found to be quantitatively inaccurate. In particular, the Thorpe sorting method overestimates dissipation by more than an order of magnitude at locations with large density inversions where turbulence primarily originates from the convective instability of these large overturns. However, the same method performs better in the case of turbulence driven by strong shear. The overprediction of the Thorpe sorting method in the case of convectively-driven turbulent patches in a stratified background is consistent with prior numerical studies of idealized problems, e.g. DNS by Scotti (2015), DNS and LES by Chalamalla and Sarkar (2015). The overprediction is also consistent with the observational study by Mater et al. (2015) that reports a positive bias in overturn-based estimate of dissipation for large overturns in a strongly stratified background.

In the inversion sorting method, the overturn boundaries are determined based on local inversions in the measured density profile rather than by the sum of Thorpe-

scale displacements. This inversion sorting method is found to estimate dissipation rate more accurately at locations on the model topography that have large overturns associated with internal waves. The reason is that an inversion that has already formed is statically unstable and the potential energy inside the inversion is instantaneously available for turbulent mixing after its collapse. The Thorpe sorting method, on the other hand, computes the Thorpe scale and, thus, the APE in a "overturn" (defined as a flow induced distortion of the density from its background profile) which *may or may not* break down into turbulence. Release of the APE into turbulence depends on the details of the flow, e.g. whether the mean state at later times is stable. The inversion sorting method has a disadvantage too. It underestimates turbulent dissipation when the the source of turbulence is the kinetic energy present in the local (unstable because S^2 is much larger than N^2) sheared velocity profile. Under such flow conditions, the patch of turbulence is larger than what is suggested by the inversion scale in the measured profile since instantaneously available potential energy (IAPE) of the inversion is not the primary driver of turbulence. On the other hand, the standard Thorpe method works well in these shear-unstable situations with $Ri_g = O(1)$ since $L_T^2 N^3$ becomes proportional to $L^2 S^3$ which is the inertial estimate (u^3/L with the turbulent velocity u taken as SL) of turbulent dissipation. Neither overturn-based method is accurate when the turbulence is locally due to advection or turbulent transport from elsewhere.

To conclude, both overturn-based methods give overall qualitative trends regarding the turbulent dissipation in the case of internal waves at rough topography. However, quantitative accuracy is highly dependent on the details of the flow. The inversion sorting method is better at estimating turbulent dissipation when the turbulence results directly from available potential energy (breaking internal waves in the present flow) while the widely-used Thorpe sorting method is better when the pathway to turbulence is directly

from kinetic energy (near-bottom unstable regions of stratified shear). At hotspots of turbulence such as steep, rough topography similar to the flow simulated here, the dominant contributor to turbulence in the near field is likely to be breaking internal waves and, if so, the inversion sorting method, after calibration for the proportionality coefficient, could provide a more accurate estimate of cycle-averaged turbulent dissipation than the Thorpe sorting method.

Acknowledgements

This chapter, in full, is a reprint of the material as it appears in "On the accuracy of overturn-based estimates of turbulent dissipation at rough topography", M. Jalali, V.K. Chalamalla, S. Sarkar, *J. Phys. Oceanogr*, 47.3 (2017): 513-532. The dissertation author is the primary investigator and author of this paper. I am gratefully acknowledge the support of ONR Grant N00014-09-1-0287.

Chapter 7

Multiscale modeling of internal waves and turbulence with SOMAR-LES

In this section, we present the SOMAR-LES framework. We start with a general introduction to SOMAR, followed by a brief discussion of the equations that are solved and the SubGrid Stress (SGS) model that is employed. SOMAR is developed by Edward Santilli and Alberto Scotti at the university of North Carolina.(Santilli and Scotti., 2015). SOMAR-LES is the result of the collaboration between SOMAR team from University of North Carolina and CFD lab in University of California, San Diego led by Vamsi Chalamalla under supervision of Sutanu Sarkar and Alberto Scotti. (Chalamalla et al., 2017)

7.1 The SOMAR framework

SOMAR solves a set of conservation equations for momentum and buoyancy on a composite grid consisting of several levels, each at different resolution. The coarse level (base) grid spans the entire problem's domain with the fine level grids nested within

the base grid in small patches. The fine level grid changes in time to follow features that need high resolution (e.g., turbulent patches). At periodic intervals, cells on the coarse grid are flagged for refinement if specific criteria, which are left to the user to define, are met (see Santilli and Scotti., 2015, for details). This increases efficiency and allows the resolution of a wide range of scales with a reduced computational cost when compared to a traditional single-level solver. On each level, time marching is performed independently. Information from the coarse level is propagated upwards to the fine level via Dirichlet boundary conditions at the coarse-fine interface and through interpolation from the coarse level at the time of fine level grid creation. Information from the fine level, which serves as a correction to the coarse level data, is propagated downwards at *synchronization points*.

Synchronization operations are performed when two or more levels reach the same time. At these points, the fine level velocity and buoyancy fields are averaged down to correct the coarse level data. Since the fluxes into the coarse cells adjacent to the coarse-fine interface need not be identical among the various levels, conservation of total momentum and mass are violated upon averaging. SOMAR restores global conservation by considering this flux difference among the levels and adding or subtracting momentum and mass from the interface-adjacent cells. This process is called *refluxing*. The resulting composite velocity field is then projected to be divergence-free. These synchronization operations are carried out at times illustrated in figure 7.1 and the reader is encouraged to refer to Santilli and Scotti. (2015) for more details.

SOMAR uses second-order, central finite differences for the spatial discretization of viscous terms, computed explicitly for time advancement. Advection terms are computed using the Piecewise-Parabolic Method (PPM) of Colella and Woodward (1984), a

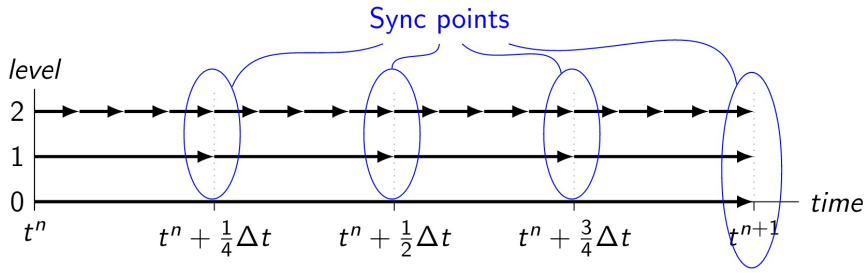

Figure 7.1: A single composite time step with synchronization points identified.

finite volume method.

Both physical and coarse-fine interfacial boundary conditions are satisfied via ghost extrapolation. At the coarse-fine interface, data on both and coarse and fine levels are used to interpolate Dirichlet conditions and extrapolate fine level ghosts. The coarse level data needed at an intermediate time step of the subcycling process is generated using conservative linear interpolation in time. The order of the interpolation is linear in the hyperbolic solver and quadratic in the parabolic and elliptic solvers. The stencils for both the linear and quadratic interpolators are well described in Adams et al. (2011) and their use in SOMAR is fully detailed in Santilli and Scotti. (2015).

7.1.1 Governing equations

In what follows, the subscripts C and F represent quantities on the coarse and fine grids, respectively. x represents the stream-wise direction, y is the span-wise direction, and z represents the vertical (opposing gravity) direction. The variable, $\overline{\phi}$, denotes the filtered value of the variable, ϕ.

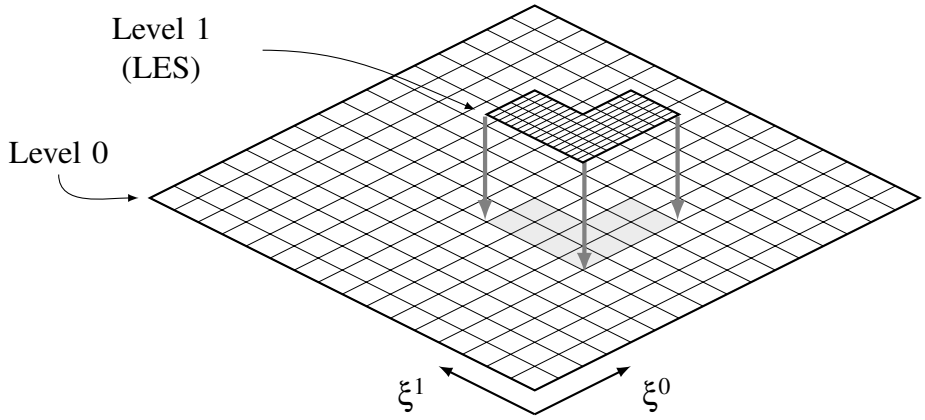

Figure 7.2: Two-dimensional visualization of two-level grid hierarchy is shown in SOMAR. Level 1 grids, on which LES is performed, exists only in the localized regions of interest. In this study, the tagging criteria has been chosen such that the level 1 grid occupies only a small percentage of the total domain, however the exact percentage of the fine level grid varies among cases.

7.1.1.1 Fine grid equations

The filtered Navier-Stokes equations solved on fine level grid are given by

$$\nabla \cdot \overline{\mathbf{u}}_F = 0, \tag{7.1a}$$

$$\frac{D\overline{\mathbf{u}}_F}{Dt} = -\nabla p_F^* - \overline{b}_F^* \hat{\mathbf{k}} + \nu \nabla^2 \overline{\mathbf{u}}_F - \nabla \cdot \boldsymbol{\tau}, \tag{7.1b}$$

$$\frac{D\overline{b}_F^*}{Dt} = \kappa \nabla^2 \overline{b}_F^* + \overline{w}_F N^2 - \nabla \cdot \boldsymbol{\lambda}. \tag{7.1c}$$

Here, $\overline{u}_F, \overline{v}_F, \overline{w}_F$ represent filtered velocities in the streamwise, spanwise, and vertical directions, respectively, p_F^* denotes the deviation from the background hydrostatic pressure, and $\overline{b}_F^*$ denotes the deviation from the background buoyancy stratification. The sub-grid scale stress tensor, $\boldsymbol{\tau}$, and the density flux vector, $\boldsymbol{\lambda}$, are given by

$$\tau_{ij} = -2\nu_{sgs}\overline{S_{ij}} \tag{7.2}$$

and

$$\lambda_j = -\kappa_{sgs}\frac{\partial \overline{b}^*}{\partial x_j}. \tag{7.3}$$

Two different LES models have been considered in this study. For the first set of test cases, the standard Smagorinsky model (Smagorinsky, 1963) is considered, whose subgrid scale viscosity is given by

$$\nu_{sgs}(\mathbf{x},t) = (C_S\Delta)^2|\overline{S}|. \tag{7.4}$$

The Smagorinsky coefficient, C_s, is analytically found to be 0.17 in isotropic turbulence. Several studies have shown that $C_s = 0.17$ leads to excessive dissipation in shear flows and smaller values of the Smagorinsky coefficient between 0.08 and 0.1 have been used in LES of shear flows, e.g. channel flow (Deardorff, 1970; Piomelli et al., 1988) and pipe flow (Brandt, 2005). The value of C_s is found to increase from a small value at early time to $C_s \approx 0.13$ at late time in LES of a temporally evolving shear layer (Vreman et al., 1997b), and from 0.04 near the inflow to 0.13 in the region of fully-developed turbulence in a spatially evolving jet (Ribault et al., 1999). LES of a stratified shear layer by Pham and Sarkar (2014) shows that C_s in the turbulent stage varies from 0.13 in the central core of the shear layer to about 0.08 at the flanks where the turbulence is intermittent. For simplicity, we choose the standard Smagorinsky model rather than the dynamic Smagorinsky model and, furthermore, choose a low value of $C_s = 0.085$ so as to allow instabilities and transition to turbulence, an important feature in the problem of turbulence driven by internal tides (Sarkar and Scotti, 2017). A turbulent Prandtl number of 1 is used to calculate the sub-grid scale diffusivity κ_{sgs}.

The LES model for the Gaussian ring test case (discussed in section 5) is based on the second order filtered structure function (FSF) discussed in Ducros et al. (1996). In this approach, a high pass Laplacian filter (denoted by $\sim$) iterated three times is applied to the velocity field before calculating the structure function. A six-neighbor formulation is used to calculate the filter velocity as shown below (see Ducros et al. (1996) for details)

$$\begin{aligned}\tilde{\tilde{u}}(i,j,k) = \overline{u}(i+1,j,k) - 2\overline{u}(i,j,k) + \overline{u}(i-1,j,k) \\ + \overline{u}(i,j+1,k) - 2\overline{u}(i,j,k) + \overline{u}(i,j-1,k) \\ + \overline{u}(i,j,k+1) - 2\overline{u}(i,j,k) + \overline{u}(i,j,k-1).\end{aligned}$$

The sub-grid scale viscosity, ν_{sgs}, is given by

$$\nu_{sgs}(\mathbf{x},t) = 0.0014 C_K^{-3/2} \overline{\Delta} \left(\overline{F_2}(\mathbf{x},\Delta,t)\right)^{1/2} \tag{7.5}$$

where Δ is the filter width based on the grid size in all directions $(\Delta x \Delta y \Delta z)^{1/3}$, C_K is the Kolmogorov constant, and $\overline{F_2}$ is the filtered structure function given by

$$\begin{aligned}\overline{F_2}(\mathbf{x},t) = \quad 1/6 \Big(& ||\tilde{\tilde{u}}_{i+1,j,k} - \tilde{\tilde{u}}_{i,j,k}||^2 + ||\tilde{\tilde{u}}_{i-1,j,k} - \tilde{\tilde{u}}_{i,j,k}||^2 \\ & + ||\tilde{\tilde{u}}_{i,j+1,k} - \tilde{\tilde{u}}_{i,j,k}||^2 + ||\tilde{\tilde{u}}_{i,j-1,k} - \tilde{\tilde{u}}_{i,j,k}||^2 \\ & + ||\tilde{\tilde{u}}_{i,j,k+1} - \tilde{\tilde{u}}_{i,j,k}||^2 + ||\tilde{\tilde{u}}_{i,j,k-1} - \tilde{\tilde{u}}_{i,j,k}||^2 \Big).\end{aligned}$$

This model is applied to the test case where the flow is not fully turbulent and highly intermittent in both space and time. This model was found to be less dissipative when compared to the classical Smagorinsky model in some flow scenarios.

7.1.1.2 Coarse grid equations

The Navier-Stokes equations solved on coarse level grids are given by

$$\nabla \cdot \mathbf{u}_C = 0, \tag{7.6a}$$

$$\frac{D\mathbf{u}_C}{Dt} = -\nabla p_C^* - b_C^* \hat{\mathbf{k}} + \nu \nabla^2 \mathbf{u}_C - \nabla \cdot (\boldsymbol{\tau})_{F \to C}, \tag{7.6b}$$

$$\frac{Db_C^*}{Dt} = \kappa \nabla^2 b_C^* + w_C N^2 - \nabla \cdot (\boldsymbol{\lambda})_{F \to C}. \tag{7.6c}$$

Here, $\boldsymbol{\tau}_{F \to C}$ and $\boldsymbol{\lambda}_{F \to C}$ account for the turbulent effects solved at the fine level. They are obtained by averaging $\boldsymbol{\tau}$ and $\boldsymbol{\lambda}$ from fine grid on to the coarse grid. Of course, they are different from zero only in regions overlapping a fine grid.

7.1.2 Turbulent diagnostics

The instantaneous velocity field can be decomposed into mean and fluctuating components, $u = \langle u \rangle + u'$. The calculation of the mean component $\langle u \rangle$ varies according to the flow type. If there is a periodic direction, the mean component is calculated by performing a spatial average in the periodic direction on all grid levels. Then, derived quantities such as turbulent kinetic energy and turbulent production are first calculated on all levels, with the more accurate fine level values averaged down to the coarse grid. If a periodic direction doesn't exist, we average the fine-level solution down to the coarsest grid, then perform a conservative linear interpolation back up to the fine grid. This essentially filters out any velocity component that can only be harbored on the refined grids. The interpolated velocity is assumed to be the ensemble average on fine level. In the case where there is no periodic direction, the derived quantities such as TKE and turbulent production are computed only on the fine level grid and averaged down to the

coarse grid.

7.1.3 Flow Analysis on data spread over nested grids

Special care must be taken when post-processing data which belongs to grids with different resolution. Failure to properly incorporate the coarse and fine data into post-processing efforts can lead to filtering of high wavenumber modes. In this section, we will consider how the energy budget calculation is performed on our adaptive mesh and provide justification for our algorithmic decisions. SOMAR-LES is typically setup to produce two levels of data. The coarse level, which extends over the entire problem's domain, contains data produced by the large-scale solver. The fine level, which only exists in small, sparse regions of the domain, contains data that is more accurate for two major reasons. First, the time-stepper experiences significantly less truncation error. For example, with a refinement ratio of 4, the fine level achieves at least 16 times less numerical diffusion than the coarse level. Second, since the grid is more refined, it can harbor modes that are sub-grid to the coarse level. This is important for the LES since it needs to filter-out, dealias, and model all of the high-wavenumber modes that the grid cannot support. Since SOMAR-LES uses block-structured adaptive mesh refinement, there is, in a sense, some data duplication. The data that lives on the fine level overshadows less resolved data on the coarse level. This less-resolved data is often called *invalid data* since it is not as accurate as its fine-level version, but this invalid data still serves a significant purpose. Each invalid cell contains the average of all of the fine-level cells above it. This makes line and volume integration significantly simpler – whatever needs to be integrated can be averaged down to the coarse level, where we can sum over any sub-domain with impunity. Since the coarse level extends over the entire domain, we will not run into missing regions of data as we would on the fine level. Integrals carried out in this way

are guaranteed to be as accurate as possible since they effectively use the most accurate data available.

This "average then sum" method does not work for derived quantities such as the energy. To correctly compute the integral of the energy or any other derived quantity, we must first compute the derived quantity on all levels, then average down and integrate.

7.2 Modeling Luzon strait with SOMAR-LES

To illustrate the capabilities of SOMAR-LES, the Luzon Strait problem discussed in Chapter 5 is selected. The problem is characterized by non-trivial topography and turbulent regions which are not stationary. This case is performed with a two-level grid with a refinement ratio of 4:1 in all directions, using the gradient Richardson number, Ri_g, as the criterion to tag the coarse level cells for refinement. Regridding is performed every 4 coarse time steps. If the regridding interval is too small, computational overhead increases, but if too large, the nonlinear features may move off of the fine grid. The regridding interval has been chosen to balance between these effects. The model uses curvilinear grid coordinates over a digital elevation map (DEM) which is obtained from discrete points of the realistic two-dimensional bathymetry used in Chapter 5 and with no variation in the third (spanwise) direction. Earth's rotation is ignored in this study for simplicity. The barotropic tidal forcing is imposed by adding the following pressure gradient term to right hand side of the x-momentum equation (i.e., eq. 7.6 b),

$$F_0(t) = U_0 \Omega \cos(\Omega t). \tag{7.7}$$

Here, U_0 is the barotropic velocity amplitude, Ω is the forcing frequency, and t

represents dimensional time.

Table 7.1: Simulation parameters for different cases of tidal flow simulation at an smoothed west ridge of Luzon strait. Barotropic forcing frequency Ω corresponds to the semi diurnal internal tide. The units for grid parameters are in meters. The coarse grid is uniform and has $1024 \times 32 \times 256$ grid points in the x, y and z directions, respectively.

$U_0(m/s)$	$h(km)$	$\nu(kg/sm)$	$\Omega(1/s)$	Re_s	ε_{max}
0.1	2.1	10^{-6}	0.0001407	11922	2.13
$L_x(km)$	L_y	L_z	$dx_C\,[dx_F]$	$dy_C\,[dy_F]$	$dz_C\,[dz_F]$
58.4	1.2	3.694	57.0 [14.25]	37.5 [9.37]	14.4 [3.60]

Simulation parameters are shown in Table 7.1 as is the grid resolution for all levels. Parameters dx_C, dy_C, and dz_C represent grid spacing on the coarse level grid in the streamwise (x), spanwise (y), and vertical (z) directions, respectively. Fine grid spacing, dx_F, dy_F and dz_F, are shown in squared brackets in table 7.1. Both horizontal and vertical directions have molecular viscosity of $1 \times 10^{-6} m^2/s$ and the ratio of molecular viscosity to diffusivity is $Pr = 1$. Periodic boundary conditions are used in the spanwise (y) direction. The background stratification is based upon a realistic density background in the region as described in chapter 5. Sponge forcing is applied at the left (x_{min}) and right (x_{max}) boundaries to absorb the internal wave energy radiated outside the domain of interest.

The results agree well qualitatively with the previous study in chapter 5 depicting internal wave and turbulence characteristics previously observed in the region. Figure 7.3 shows snapshots of the x-direction velocity at four time instances for phases between $\Theta = \Omega t = 5/4\pi$ and $\Theta = 2\pi$. The velocity is shown in three mutually-orthogonal cutting planes. The velocity is intensified over the steep region and the top of the two sub-ridges. The computational mesh on the fine level is also shown, represented by the black shaded

region. The fine level grid adapts in time based on the gradient Richardson number criteria ($Ri_g < 0.25$). The vertical-spanwise plane at x = 25km shows that the vertical extent of the fine grid varies with time. In Figure 7.3 (a)-(c), the fine grid occupies a region of 500 m directly over the slope. This region shrinks to a vertical height of 250 m in Figure 7. 3 (d). The streamwise-vertical plane also shows that refinement of the grid changes with time and occurs mainly at the steep-slope region of the ridge and at the vertically thin (high-mode) wave features emanating from the ridge.

The fine level has very limited extent in the streamwise (x) and vertical (z) directions. Since the turbulence in this case exists mainly close to the bathymetry, the fine level grid is confined close to the crest in the streamwise direction, with width of about $0.1H$ in the vertical direction. However, in the spanwise direction, the fine level grid extends along the whole domain from y_{min} to y_{max}. The fine grid is used at the internal wave beams and jets with high shear and in a convectively unstable region close to the topography. As these regions change in time, the refined region changes accordingly.

Figure 7.4 shows magnified snapshots of the xz-plane Ri_g field at two different time instances. The coarse level grid spans the entire domain, whereas the fine level grid is adaptively created in localized regions where the gradient Richardson number drops below 0.25 to follow the turbulent patch as it sloshes back and forth over the ridge. In the bottom panel, snapshots of turbulent kinetic energy ($Log_{10}[TKE]$) are shown. Turbulence intensity is significant during flow reversal as seen in the bottom panels where the density overturn breaks down creating a tall turbulent patch. On average for this case, the fine level occupies less than 5% of the domain to resolve the nonlinear features, thus saving significant computational cost.

It is found that, without resolving the internal waves as they propagate, wave

beam intensification will be compromised, leading to reduction or elimination of turbulence in those regions. Results would also lack important small-scale features in the turbulent regions. To illustrate this, figure 7.5 compares the streamwise velocity field in fine and coarse level grids to highlight the small-scale features that the second level and subgrid-scale can add to the simulated response.

Acknowledgements

This chapter, in parts, in parts, a reprint of material published in following journal: V.K. Chalamalla, E. Santilli, A. Scotti, M. Jalali, S. Sarkar, "SOMAR-LES: A framework for multi-scale modeling of turbulent stratified oceanic flows" under review for publication in *Ocean Model.*. The dissertation author is one of the investigators and co-authors of this paper. I am grateful gratefully acknowledge the support of NSF grants OCE-1459774 and OCE-1459506.

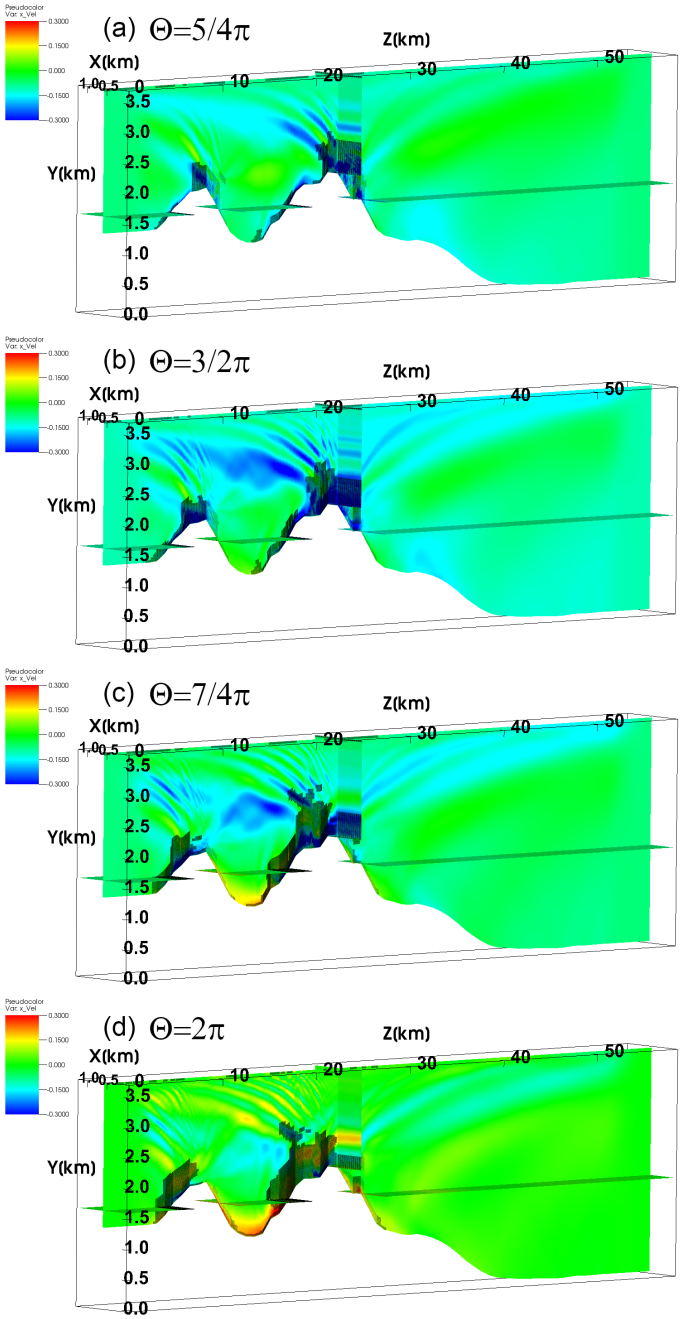

Figure 7.3: Snapshots of the x-direction velocity contours in three planes at various time instances for phases (a) $\Theta = 5/4\pi$, (b) $\Theta = 3/2\pi$, (c) $\Theta = 7/4\pi$, and (d) $\Theta = 2\pi$. Each Subplot has three orthogonal cutting planes. Fine level computational grids cells are shown by the black shaded region in each cutting plane.

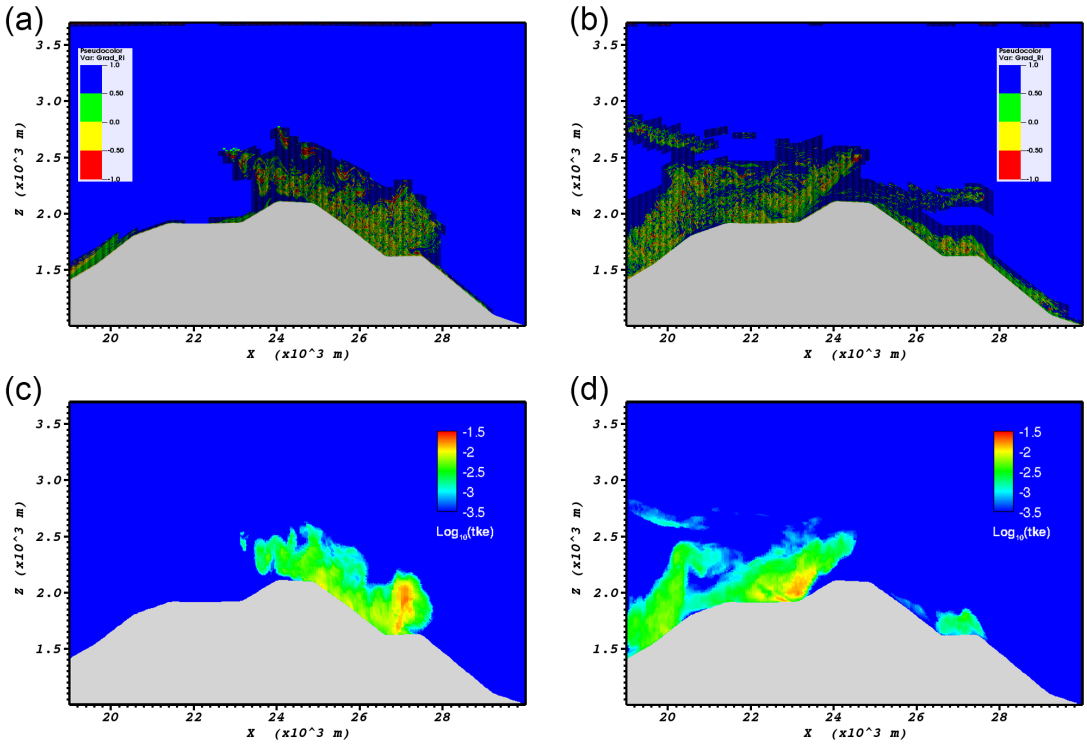

Figure 7.4: Top: Snapshots of the gradient Richardson number contours in a magnified region of xz-plane showing the fine level mesh in shades at (a) $\Theta = 5/4\pi$ and, (b) $\Theta = 2\pi$. Bottom: Snapshots of the turbulent kinetic energy contours in logarithmic scale for the same location and phase of the corresponding panels in the top row as (c) $\Theta = 5/4\pi$ and, (d) $\Theta = 2\pi$.

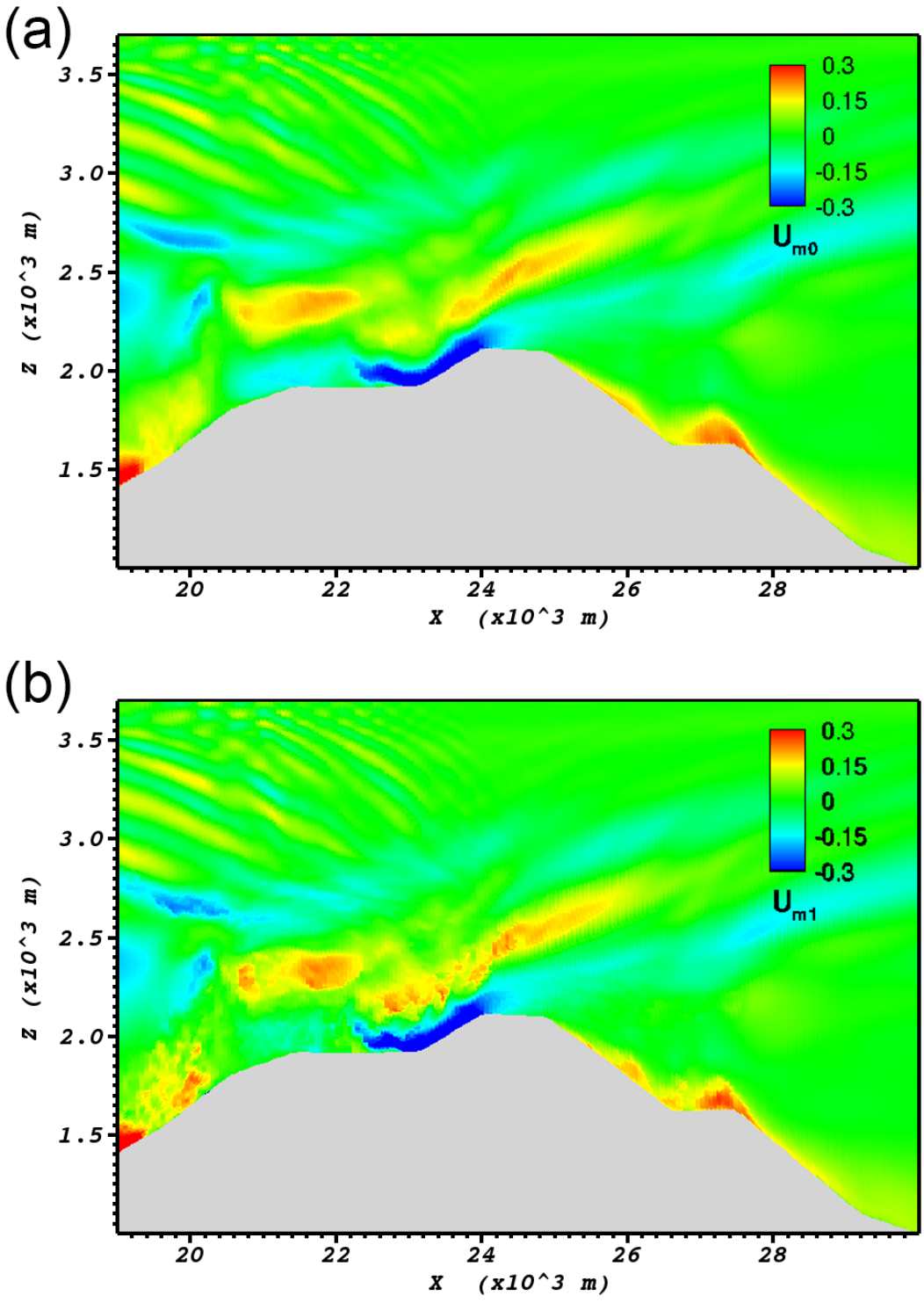

Figure 7.5: Snapshots of the x-direction velocity contours in a magnified region of xz-plane calculated at $\Theta = 5/4\pi$, in the (a)the coarse level and (b) the fine level.

Chapter 8

Summary and future directions

Topographic features with steep, supercritical slope on the ocean bottom are sites of large energy conversion from the oscillating tide to internal waves according to linear theory. At the same time, they are also sites with potentially large local energy loss as is suggested by nonlinear waves and overturns found in field observations and two-dimensional simulations. In chapter 3, direct numerical simulations (DNS) are performed to study how internal gravity waves and turbulence change when Ex is varied from a low value (typical of a large ridge in the deep ocean) to a value of unity (corresponding to energetic tides over a small topographic feature). An isolated obstacle having a smoothed triangular shape, overall steepness parameter of $\gamma = (h/l)/\tan(\alpha) = 0.64$, and 20% of the streamwise length at critical slope is considered. With increasing values of Ex, the near-field of the internal waves looses its beam like character, the wave response becomes asymmetric with respect to the ridge center, and transient lee waves form. Analysis of the baroclinic energy balance shows significant reduction in the radiated wave flux in the cases with higher Ex owing to a substantial rise in the advective flux and baroclinic dissipation as well as a decrease in conversion. Turbulence changes qualitatively with increasing Ex. In the situation with $Ex \sim 0.1$, turbulence is intensified at the near-critical

regions of the slope, and is also significant in the internal wave beams above the ridge where there is intensified shear. At $Ex = O(1)$, the transient lee waves overturn adjacent to the ridge flanks and, owing to convective instability, buoyancy acts as a source for turbulent kinetic energy. The size of the turbulent overturns has a non-monotone dependence on excursion number: the largest overturns, as tall as twice the obstacle height, occur in the $Ex = 0.4$ case, but there is a substantial decrease of overturn size with further increase of Ex.

In chapter 4, we turned to topography that is steeper than that considered in chapter 3. An obstacle with a smoothed triangular shape having supercritical slope (gamma = 1.73 and a 77.5 % linear slope with criticality $\varepsilon = 2$) is considered as a laboratory-scale model for a two-dimensional ocean ridge. Three simulations are performed with constant Reynolds number and an excursion number (Ex) that varies from 0.066 to unity, corresponding to a large obstacle and a small obstacle, respectively. The dominant nonlinear flow feature is a downslope jet on the leeward, upper slope the obstacle with intensified velocity whose length and thickness increase with increasing Ex. During the flow reversal phase, the jet continues to initially flow downward but encounters upward flow from below and the interaction creates a rebounding jet which distorts the density resulting in convective instability. Turbulence is generated predominantly by shear in the jet, convective instabilities from the rebounding jet, and breaking of transient lee waves. The active region of turbulence grows as Ex increases although the local normalized turbulent kinetic energy becomes smaller. Analysis of the baroclinic energy budget shows that, with increasing Ex, there is a substantial decrease of energy conversion (C) to the wave field as well as a substantial increase in local energy loss (q). Primary mechanisms responsible for turbulence at supercritical obstacles are shear in the jet and convective instabilities arising from steepened isopycnals followed by wave breaking. Shallow

obstacles have noticeably less turbulence if the bathymetry has entirely subcritical slope. On the other hand, shallow obstacles with subcritical aspect ratio exhibit turbulence at deep flanks if the local slope is near critical and Ex is low.

Chapter 5 presents high-resolution, turbulence-resolving Large Eddy Simulation (LES) for flow over multiscale, steep bathymetry patterned after a portion of the west ridge of Luzon Strait at 20.6° N. Oceanic values of the slope criticality, Froude number, Excursion number, and aspect ratio are matched. The amplitude and phasing of velocity, overturns, and dissipation are similar to observations that were made at a deep mooring during IWISE. However, a tidal phase is noted in which intensification from the resonant interaction with waves generated at the east ridge is important in the observations and is lacking in the simulations since the model does not include the east ridge. Turbulent dissipation originates from several mechanisms including breaking lee waves during flow reversal, downslope jets, critical-slope boundary layer, high-mode internal wave beams, off-slope lee wave breaking and flow patterns in the valley. The model baroclinic energy budget is closed with negligible residual and the local turbulence loss of 23.5% is large.

The present results shows that the deep, underwater bathymetry has an envelope of turbulence with thickness of about $3-5\times U_0/N$ close to the topography and in the vicinity of internal wave generation sites. The turbulence results in column-integrated dissipation of $\varepsilon = 10^{-3} - 10^{-1} \times U_0^2 N$ over supercritical and near-critical regions. The results of this study are also used to extract the dependence of the local loss (cycle-averaged q) of internal wave energy on the governing non-dimensional parameters as a step towards parameterization of internal tides in ocean models. The spatial distribution of cycle-averaged q changes qualitatively among cases. The changes in q are linked to changes in the features responsible for turbulence. Local loss increases with an increase

of Ex as shown in Figure 8.1. For the flows in the $Ex \sim O(1)$ regime, the magnitude of q is significantly larger for supercritical ridges relative to subcritical ridges with 20% critical slope angle. Interaction of different mechanisms in a multiscale realistic topography like Luzon Strait leads to amplified local loss of the energy compared to the energy dissipation at an idealized triangular obstacle.

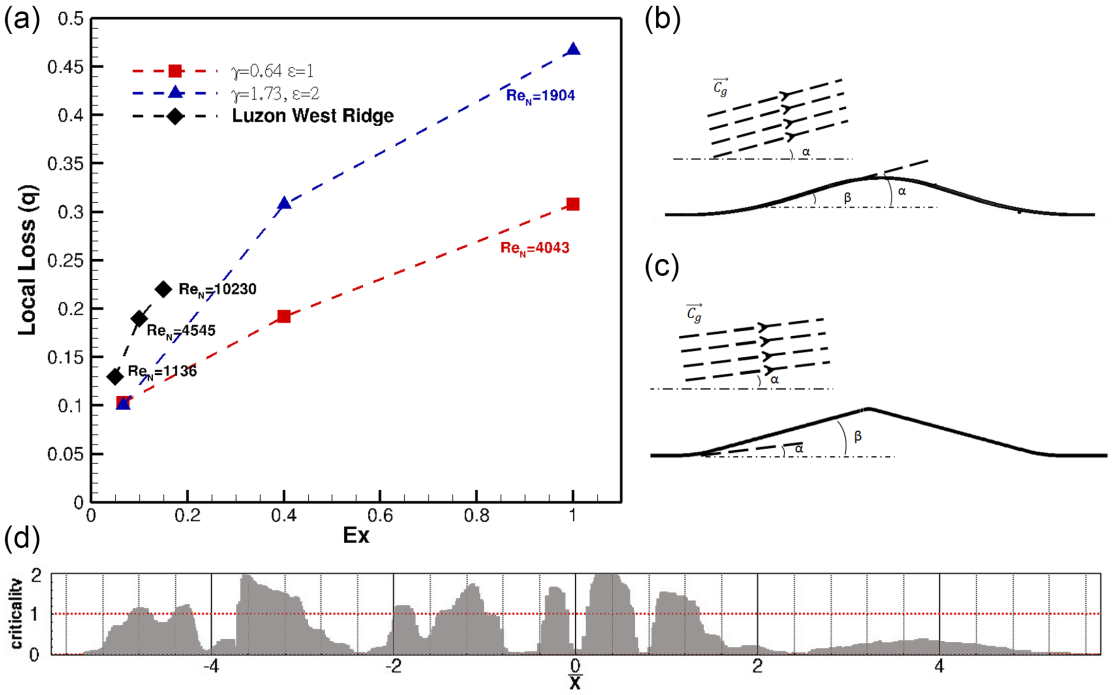

Figure 8.1: The dependence of local loss of energy, q, converted from the barotropic tide to the baroclinic field, for three different set ups: supercritical model ridge, subcritical ridge with critical slope, and multiscale topography of the Luzon Strait. Schematic of wave generation showing the wave propagation angle (α) topographic slope angle (β) for (b) critical model ridge and (c) supercritical model ridge. Panel (d) shows slope criticality in the Luzon Strait simulation.

Evidence in support of overturn-based methods, often used to infer turbulent dissipation rate from density profiles, is typically from regions with weaker turbulence than that at rough-topography hotspots. Chapter 6 uses DNS of an idealized problem of sloping topography as well as high-resolution large eddy simulation (LES) of turbulent flow

at more realistic topography, a model patterned after a cross-section (latitude 20.6° N) of the western ridge of Luzon Strait, in order to investigate the accuracy of overturn-based methods in sites with internal wave breaking. Two methods are assessed: Thorpe sorting where the overturn length L_T is based on local distortion of measured density from the background, and inversion sorting where L_I measures the statically-unstable local region. The overturn boundaries are different between the two methods. Thorpe sorting leads to an order-of-magnitude overestimate of the turbulent dissipation in the DNS during large convective overturn events when inversion sorting is more accurate. The LES of steep, realistic topography leads to a similar conclusion of a substantial overestimate of dissipation by Thorpe sorting. Energy arguments explain the better performance of inversion sorting in convectively-driven turbulence and the better performance of Thorpe sorting in shear-driven turbulence.

A new multi-scale modeling technique, SOMAR-LES (Chalamalla et al., 2017), is presented in the Chapter 7. Localized grid refinement gives SOMAR (Stratified Ocean Model with Adaptive Resolution) (Santilli and Scotti., 2015) access to smaller scales of the flow which are normally inaccessible to general circulation models (GCMs). SOMAR-LES employs the information in these smaller scales to perform a LES on SOMAR's finest grids, which in turn receives realistic, large scale forcing from the coarser grids. Three-dimensional simulations of internal tide generation at the west ridge of the Luzon Strait are performed to demonstrate this multi-scale modeling technique. SOMAR-LES is most effective in reducing the computational cost in flow situations where the location of turbulence is intermittent in space and time. With the help of adaptive refinement features and an LES model, nonlinear features can be tracked and turbulence can be modeled as the flow evolves in both space and time. Thus, SOMAR-LES can be used to tackle problems that so far have been computationally prohibitive. Coupling SOMAR-LES with

global ocean models like HYCOM can be a proper next step in utilizing this numerical model.

The present work aims at gaining a better understanding of the turbulent processes during the generation of internal waves. It is widely recognized that this process is a key ingredient in maintaining and regulating the strength of the Meridional Overturning Circulation. The latter is a crucial component of the climate system, because it affects simultaneously the uptake of CO_2 into the ocean and the meridional transport of heat. Thus, any progress that ultimately leads to better parametrizations of mixing processes for large scale climate models has a significant impact outside the ocean mixing community.

An essential follow up in the exploration of turbulence at deep topography is the study of a flow consisting of a current and a tidal oscillation that encounters a three-dimensional, conical obstacle in a stratified fluid. The study of topographic internal waves and topographic wakes/vortices have, for the most part, been conducted as a separate lines of research. However, both internal waves and wakes occur in conjunction for three-dimensional topography. The impact of the topographic and environmental parameters on wave/vortex dynamics and therefore on local turbulent dissipation and internal wave generation in such a setting is of great interest.

Appendix A

Overturn-based estimation algorithms

Algorithms 1 and 2 describe the Thorpe and Inversion sorting method, respectively.

Input : Potential Density(Temperature)

Output : Dissipation

① Find boundaries of input potential density data for a particular vertical profile ;

② Interpolate data to a equispaced grid and store as σ_{th} ;

③ Sort density profile of the entire column into a stable monotonic profile, σ_{ths} ;

④ Find vertical displacement for each point between sorted and unsorted profile, d_σ;

⑤ Calculate sum of displacements from surface, s_σ;

⑥ Set *threshold*. Mark the boundaries of overturn when $s_\sigma < threshold$;

for *Each Marked Overturn* **do**

⑦ Calculate Thorpe scale, $L_T = \sqrt{mean(d_\sigma^2)}$;

⑧ Calculate overturn N using difference of max and min of density within the unsorted data, $N_{ov} = \sqrt{-\frac{g}{\sigma_{mean}} \frac{Max(\sigma_{th}) - Min(\sigma_{th})}{h}}$ when σ_{mean} is average of σ_{th} within the overturn. ;

⑨ Calculate the dissipation of the overturn as $\varepsilon = 0.64 L_T^2 N_{ov}^3$;

end

⑩ Repeat the steps 1-9 for potential temperature if available and take the minimum of both calculated dissipations as the final estimate.;

⑪ Make plots and report profile of dissipations.

Algorithm 1: Dissipation estimation using the Thorpe Sorting Method with potential density(temperature) profile. Following the algorithm used in Alford et al. (2011).

Input : Potential Density

Output : Dissipation

① Find boundaries of input potential density data for a particular vertical profile ;

② Interpolate data to a equispaced grid and store as σ_{th};

③ Set *threshold*. Mark the boundaries of overturn wherever there is an inversion in the profile and the length of inversion, H_I is bigger than pre-set threshold, $H_I < threshold$;

for *Each Marked Overturn* **do**

④ Sort the portion of potential density Profile within the overturn into a stable monotonic profile, σ_{ths}. ;

⑤ Find vertical displacement for each point between sorted and unsorted profile within the overturn, d_σ;

⑥ Calculate Inversion Scale, $L_I = \sqrt{mean(d_\sigma^2)}$;

⑦ Calculate overturn N using difference of max and min of density within the unsorted data, $N_{ov} = \sqrt{-\frac{g}{\sigma_0}\frac{Max(\sigma_{th}) - Min(\sigma_{th})}{h}}$.;

⑧ Calculate the dissipation of the overturn as $\varepsilon = L_I^2 N_{ov}^3$;

end

⑨ Make plots and report profile of dissipations.

Algorithm 2: Dissipation estimation using the Inversion Sorting Method with potential density profile.

Bibliography

Adams, J. C. (1989). Mudpack: multigrid portable fortran software for the efficient solution of linear elliptic partial differential equations. *Appl. Math. Comput.*, 34(2):113–146.

Adams, M., Colella, P., Graves, D. T., Johnson, J., Keen, N., Ligocki, T. J., Martin, D. F., McCorquodale, P., Modiano, D., Schwartz, P., Sternberg, T., and Straalen, B. V. (2011). Chombo software package for AMR applications - Design document. *Lawrence Berkeley National Laboratory Technical Report LBNL-6616E*.

Afanasyev, Y. D. and Peltier, W. R. (1998). The three-dimensionalisation of stratified flow over two-dimensional topography. *J. Atmos. Sci.*, 55:19–39.

Akselvoll, K. and Moin, P. (1996). Large-eddy simulation of turbulent confined coannular jets. *J. Fluid Mech.*, 315:387–411.

Alford, M. H., Klymak, J. M., and Carter, G. S. (2014). Breaking internal lee waves at Kaena Ridge, Hawaii. *Geophys. Res. Lett.*, 41:906–912.

Alford, M. H., MacKinnon, J., Nash, J., Simmons, H., Pickering, A., Klymak, J., Pinkel, R., Sun, O., Rainville, L., Musgrave, R., Beitzel, T., Fu, K., and Lu, C. (2011). Energy flux and dissipation in Luzon Strait: two tales of two ridges. *J. Phys. Oceanogr.*, 41:2211–2222.

Alford, M. H., Peacock, T., MacKinnon, J. A., Nash, J. D., Buijsman, M. C., Centuroni, L. R., Chao, S., Chang, M., Farmer, D. M., Fringer, O. B., Fu, K., Gallacher, P. C., Graber, H. C., Helfrich, K. R., Jachec, S. M., Jackson, C. R., Klymak, J. M., Ko, D. S., Jan, S., Johnston, T. M. S., Legg, S., Lee, I., Lien, R., Mercier, M. J., Moum, J. N., Musgrave, R., Park, J., Pickering, A. I., Pinkel, R., Rainville, L., Ramp, S. R., Rudnick, D. L., Sarkar, S., Scotti, A., Simmons, H. L., Laurent, L. C. S., Venayagamoorthy, S. K., Wang, Y., Wang, J., Yang, Y. J., Paluszkiewicz, T., and Tang, T. (2015). The formation and fate of internal waves in the South China Sea. *Nature*, 521:0028–0836.

Armenio, V. and Sarkar, S. (2002). An investigation of stably stratified turbulent channel flow using large-eddy simulation. *J. Fluid Mech.*, 459:1–42.

Aucan, J., Merrifield, M. A., Luther, D. S., and Flament, P. (2006). Tidal mixing events

on the deep flanks of Kaena Ridge, Hawaii . *J. Phys. Oceanogr.*, 36:1202–1219.

Baines, P. G. (1995). *Topographic Effects in stratified flows.* Cambridge University Press.

Bewley, T. R. (2007). *Numerical Renaissance: simulation, optimization, and control*. Renaissance Press.

Bluteau, C. E., Jones, N. L., and Ivey, G. N. (2011). Dynamics of a tidally forced stratified shear flow on the continental slope. *J. Geophys. Res.*, 116:C11017.

Brandt, T. (2005). A posteriori study on modeling and numerical error in LES applying the Smagorinsky model. *Lect. Notes Comput. Sci. Eng.*, 56:173–189.

Buijsman, M., Klymak, J. M., Legg, S., Alford, M., Farmer, D., Mackinnon, J. A., Nash, J. D., Park, J., Pickering, A., and Simmons, H. (2014). Three-Dimensional Double-Ridge Internal Tide Resonance in Luzon Strait. *J. Phys. Oceanogr.*, 44:850–869.

Buijsman, M., Legg, S., and Klymak, J. M. (2012). Double-Ridge Internal Tide Interference and Its Effect on Dissipation in Luzon Strait. *J. Phys. Oceanogr.*, 42:1337–1356.

Cacchione, D., Pratson, L. F., and Ogston, A. (2002). The shaping of continental slopes by internal tides. *Science*, 296(5568):724–727.

Carter, G. S., Merrifield, M. A., Becker, J. M., Katsumata, K., Gregg, M. C., Luther, D. S., Levine, M. D., Boyd, T. J., and Firing, Y. L. (2008). Energetics of M2 Barotropic-to-Baroclinic Tidal Conversion at the Hawaiian Islands. *J. Phys. Oceanogr.*, 38:2205–2223.

Chalamalla, V. K., Santilli, E., Scotti, A., Jalali, M., and Sarkar, S. (2017). SOMAR-LES: A framework for multi-scale modeling of turbulent stratified oceanic flows. *Ocean Modell.*, under review.

Chalamalla, V. K. and Sarkar, S. (2015). Mixing, dissipation rate, and their overturn-based estimates in a near-bottom turbulent flow driven by internal tides. *J. Phys. Oceanogr.*, 54:1969–1987.

Colella, P. and Woodward, P. R. (1984). The Piecewise Parabolic Method (PPM) for Gas-Dynamical Simulations. *J. Comp. Phys.*, 54:174–201.

Crawford, W. (1986). A comparison of length scales and decay times of turbulence in stably stratified flows. *J. Phys. Oceanogr.*, 16:1847–1854.

Deardorff, J. W. (1970). A numerical study of three-dimensional turbulent channel flow at large Reynolds numbers. *J. Fluid Mech.*, 41:453–480.

Dillon, T. M. (1982). Vertical Overturns: A Comparison of Thorpe and Ozmidov Length Scales. *J. Geophys. Res.*, 87:9601–9613.

Dougherty, J. P. (1961). The anisotropy of turbulence at the meteror level. *J. Atmos. Terr. Phys.*, 21:210–213.

Ducros, F., Comte, P., and Lesieur, M. (1996). Large-eddy simulation of transition to turbulence in a boundary layer developing spatially over a flat plate. *J. Fluid Mech.*, 326:1–36.

Echeverri, P. and Peacock, T. (2010). Internal tide generation by arbitrary two-dimensional topography. *J. Fluid Mech.*, 659:247–266.

Farmer, D. M., Alford, M. H., Lien, R.-C., Yang, Y. J., Chang, M.-H., and Li, Q. (2011). From Luzon Straight to Dongsha Plateau: Stages in the Life of an Internal Wave. *Oceanography*, 24(4):64–77.

Ferron, B., Mercier, H., Speer, K., Gargett, A., and Polzin, K. (1998). Mixing in the Romanche Fracture Zone. *J. Phys. Oceanogr.*, 28:19291945.

Fletcher, C. A. J. (1991). *Computational Techniques for Fluid Dynamics*. Springer, second edition.

Foysi, H. and Sarkar, S. (2010). The compressible mixing layer: an LES study. *Theoret. Comput. Fluid Dynamics*, 24:565–588.

Galbraith, P. S. and Kelly, D. E. (1995). Identifying overturns in CTD profiles. *J. Atom. and Ocea. Tech.*, 13.

Gargett, A. and Garner, T. (2008). Determining Thorpe Scales from Ship-Lowered CTD Density Profiles. *J. Atmos. Oceanic Technology*, 25:1657–1670.

Garrett, C. and Kunze, E. (2007). Internal Tide Generation in the Deep Ocean. *Ann. Rev. Fluid Mech.*, 39:57–87.

Gayen, B. and Sarkar, S. (2010). Turbulence During the Generation of Internal Tide on a Critical Slope. *Phys. Rev. Lett.*, 104:218502.

Gayen, B. and Sarkar, S. (2011a). Boundary mixing by density overturns in an internal tidal beam. *Geophys. Res. Lett.*, 38:L14608.

Gayen, B. and Sarkar, S. (2011b). Direct and large eddy simulations of internal tide generation at a near critical slope. *J. Fluid Mech.*, 681:48–79.

Gayen, B. and Sarkar, S. (2014). PSI to turbulence during internal wave beam refraction through the upper ocean pycnocline. *Geophys. Res. Lett.*, 41:8953–8960.

Germano, M., Piomelli, U., Moin, P., and Cabot, W. H. (1991). A dynamic subgrid-scale eddy viscosity model. *Phys. Fluids*, 3(7):1760–1765.

Gostiaux, L. and Dauxois, T. (2007). Laboratory experiments on the generation of internal tidal beams over steep slopes. *Phys. Fluids*, 19:028102.

Haren, H., Cimatoribus, A., and Gostiaux, L. (2015). Where large deep-ocean waves break. *Geophysical Research Letters*, 42(7):2351–2357.

Jalali, M., Chalamalla, V. K., and Sarkar., S. (2017). On the accuracy of overturn-based estimates of turbulent dissipation at rough topography. *J. Phys. Oceanogr.*, 47:513–532.

Jalali, M., Rapaka, N., and Sarkar, S. (2014). Tidal flow over topography: effect of excursion number on wave energetics and turbulence. *J. Fluid Mech.*, 750:259 – 283.

Jalali, M. and Sarkar., S. (2017). Large eddy simulation of flow and turbulence at the steep topography of Luzon Strait. *Geophys. Res. Lett.*

Jalali, M., VanDine, A., Chalamalla, V. K., and Sarkar, S. (2016). Oscillatory stratified flow over supercritical topography: wave energetics and turbulence. *Computers & Fluids*.

Kang, D. and Fringer, O. (2011). Energetics of Barotropic and Baroclinic Tides in the Monterey Bay Area. *J. Phys. Oceanogr.*, 42:272–290.

Klymak, J. M., Moum, J. N., Nash, J. D., Kunze, E., Girton, J. B., Carter, G. S., Lee, C. M., Sanford, T. B., and Gregg, M. C. (2006). An Estimate of Tidal Energy Lost to Turbulence at the Hawaiian Ridge . *J. Phys. Oceanogr.*, 36:1148–1164.

Klymak, J. M., Pinkel, R., and Rainville, L. (2008). Direct breaking of the internal tide near topography: Kaena Ridge, Hawaii . *J. Phys. Oceanogr.*, 38:380–399.

Legg, S. and Klymak, J. (2008). Internal hydraulic jumps and overturning generated by tidal flows over a tall steep ridge . *J. Phys. Oceanogr.*, 38:1949–1964.

Leichter, J. J., Stewart, H. L., and Miller, S. L. (2003). Episodic nutrient transport to florida coral reefs. *Limnology and Oceanography*, 48(4):1394–1407.

Levine, M. D. and Boyd, T. J. (2006). Tidally forced internal waves and overturns observed on a slope: Results from HOME. *J. Phys. Oceanogr.*, 36:1184–1201.

Lim, K., Ivey, G. N., and Jones, N. L. (2010). Experiments on the generation of internal waves over continental shelf topography. *J. Fluid Mech.*, 663:385–400.

Lund, T. S. (1997). On the use of discrete filters for large eddy simulation. *Annual Research Briefs*, pages 83–95.

Martin, M., Piomelli, U., and Candler, G. (2000). Subgrid-Scale Models for Compressible Large-Eddy Simulations. *Theoret. Comput. Fluid Dynamics*, 13:361376.

Mater, B. D., Schaad, S. M., and Venayagamoorthy, S. K. (2013). Relevance of the Thorpe length scale in stably stratified turbulence. *Phys. Fluids*, 25:076604.

Mater, B. D., Venayagamoorthy, S. K., Laurent, L. S., and Moum, J. N. (2015). Biases in Thorpe scale estimates of turbulence dissipation Part I: Assessments from large-scale overturns in oceanographic data. *J. Phys. Oceanogr.*, 45:2497–2521.

Moum, J. N. (1996). Energy-Containing scales of turbulence in the ocean thermocline. *J. Geophys. Res.*, 101:14095–14109.

Nash, J. D. and Moum, J. N. (2013). Shipboard LADCP/χpod Profiling of Internal Wave Structure and Dissipation in the Luzon Strait. *ONR report, N00014-09-1-0281*.

Ozmidov, R. V. (1965). On the Turbulent Exchange in a Stably Stratified Ocean. *Izv. Atmos. Oceanic Phys*, 8:853–860.

Peters, H., Gregg, M. C., and Toole, J. M. (1988). On the parameterization of equatorial turbulence. *J. Geophys. Res.*, 93:1199–1218.

Pétrélis, F., Llewellyn Smith, S. G., and Young, W. R. (2006). Tidal conversion at submarine ridge. *J. Phys. Oceanogr.*, 36:1053–1071.

Pham, H. T. and Sarkar, S. (2014). Large Eddy Simulations of a Stratified Shear Layer. *J. Fluids Engineering*, 136:060913.

Piomelli, U. (1995). Large eddy simulation of rotating channel flows using a localized dynamic model. *Phys. of Fluids*, 7:839–848.

Piomelli, U., Moin, P., and Ferziger, J. H. (1988). Model consistency in large eddy simulation of turbulent channel flows. *Phys. Fluids*, 31:1884–1891.

Pope, S. B. (2011). *Turbulent Flows*. Cambridge University Press.

Rapaka, N. R., Gayen, B., and Sarkar, S. (2013). Tidal Conversion and Turbulence at a Model Ridge: Direct and Large Eddy Simulations. *J. Fluid Mech.*, 715:181–209.

Rapaka, N. R. and Sarkar, S. (2016). An immersed boundary method for direct and large eddy simulation of stratified flows in complex geometry. *J. Comput. Phys.*, 322:511–534.

Ribault, C. L., Sarkar, S., and Stanley, S. (1999). Large eddy simulation of a plane jet. *Phys. Fluids*, 11:3069–3083.

Rodi, W., Ferziger, J., Breuer, M., and Pourquie, M. (1997). Status of large eddy simulation: results of a workshop. *J. Fluids Eng.-T ASME*, 119:248–262.

Rudnick, D. L., Boyd, T. J., Brainard, R. E., Carter, G. S., Egbert, G. D., Gregg, M. C.,

Holloway, P. E., Klymak, J. M., Kunze, E., Lee, C. M., Levine, M. D., Luther, D. S., Martin, J. P., Merrifield, M. A., Moum, J. N., Nash, J. D., , Pinkel, R., Rainville, L., and Sanford, T. B. (2003). From tides to mixing along the Hawaiian Ridge. *Science.*, 301:355–357.

Santilli, E. and Scotti., A. (2011). An efficient method for solving elliptic equations on highly anisotropicgrids. *J. Comp. Phys.*, 230:8342–8359.

Santilli, E. and Scotti., A. (2015). An AMR based baroclinic ocean model. *J. Comp. Phys.*, 291:60–91.

Sarkar, S. and Scotti, A. (2017). From topographic internal gravity waves to turbulence. *Ann. Rev. Fluid Mech.*, 49:195–220.

Scotti, A. (2015). Biases in Thorpe scale estimates of turbulence dissipation Part II: Energetics arguments and turbulence simulations. *J. Phys. Oceanogr.*, 45(10):2522–2543.

Smagorinsky, J. (1963). General circulation experiments with the primitive equations. Part I: The basic experiment. *Monthly Weather Review*, 91:99–164.

Smyth, W. D., Moum, J. N., and Caldwell, D. R. (2001). The Efficiency of Mixing in Turbulent Patches: Inferences from Direct Simulations and Microstructure Observations . *J. Phys. Oceanogr.*, 31:19691992.

Taylor, J. R. and Sarkar, S. (2008). Stratification effects in a bottom Ekman layer. *J. Phys. Oceanogr.*, 38(11):2535–2555.

Thorpe, S. A. (1977). Turbulence and mixing in a Scottish Loch. *Philos. Trans. R. Soc. London Ser. A*, 286:125–181.

van Haren, H. (2006). Nonlinear motions at the internal tide source. *Geophys. Res. Lett.*, 33:L11605.

Vreman, B., Geurts, B., and Kuerten, H. (1997a). Large eddy simulation of the turbulent mixing layer. *J. Fluid Mech.*, 339:357–390.

Vreman, B., Geurts, B., and Kuerten, H. (1997b). Large-eddy simulation of the turbulent mixing layer. *J. Fluid Mech.*, 339:357–390.

Wesson, J. C. and Gregg, M. C. (1994). Mixing at Camarial Sill in the Strait of Gibraltar. *J. Geophys. Res.*, 99:9847–9878.

Winters, K. B. (2015). Tidally driven mixing and dissipation in the stratified boundary layer above steep submarine topography. *Geophys. Res. Lett.*, 42:7123–7130.

Winters, K. B. and Armi, L. (2013). The response of a continuously stratified fluid to an

oscillating flow past an obstacle. *J. Fluid Mech.*, 727:83–118.

Wong, S. H., Santoro, A. E., Nidzieko, N. J., Hench, J. L., and Boehm, A. B. (2012). Coupled physical, chemical, and microbiological measurements suggest a connection between internal waves and surf zone water quality in the southern california bight. *Continental Shelf Research*, 34:64–78.

Wu, X. and Squires, K. (1998). Numerical investigation of the turbulent boundary layer over a bump. . *J. Fluid Mech.*, 362:229–271.

Wunsch, C. and Ferrari, R. (2004). Vertical mixing, energy, and the general circulation of the oceans. *Annu. Rev. Fluid Mech.*, 36:281–314.

Yakovenko, S. N., Thomas, T. G., and Castro, I. P. (2011). A turbulent patch arising from a breaking internal wave. *J. Fluid Mech.*, 677:103–133.

Zang, Y., Street, R. L., and Koseff, J. R. (1993). A dynamic mixed subgrid-scale model and its application to turbulent recirculating flows . *Phys. Fluids A*, 5(12):3186–3196.

Zhang, H. P., King, B., and Swinney, H. L. (2008). Resonant Generation of Internal Waves on a Model Continental Slope. *Phys. Rev. Lett.*, 100:244504.